Title
Cerebrovascular response to focal brain irradiation

Permalink
https://escholarship.org/uc/item/7r7008bp

Author
Gobbel, Glenn T.

Publication Date
1991

Peer reviewed|Thesis/dissertation

Cerebrovascular Response to Focal Brain Irradiation:
Modification by alpha-Difluoromethylornithine
by

Glenn T. Gobbel

DISSERTATION

Submitted in partial satisfaction of the requirements for the degree of

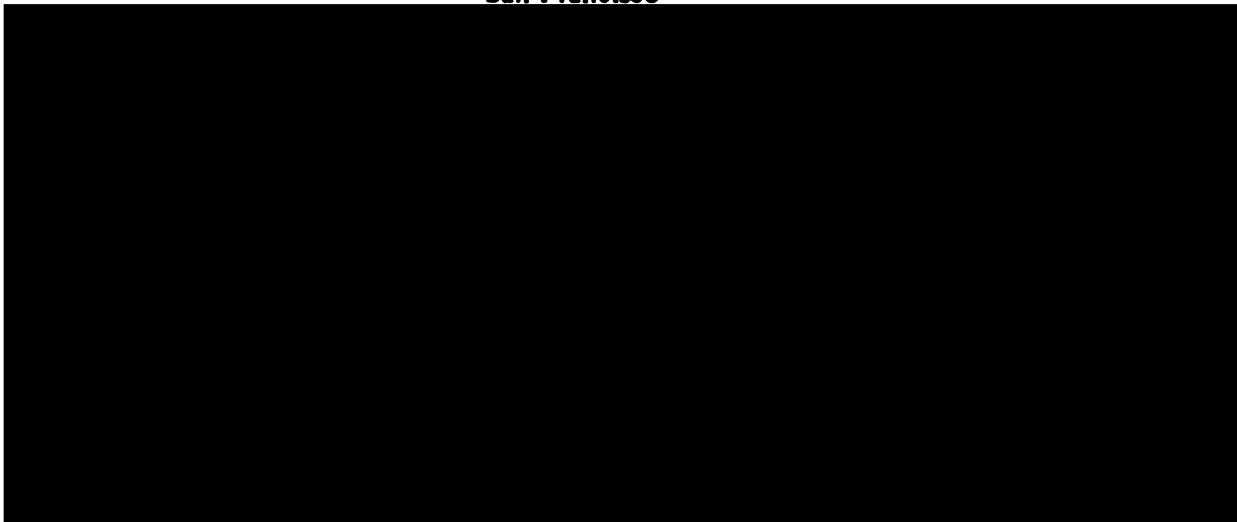DOCTOR OF PHILOSOPHY

in

Biophysics

in the

GRADUATE DIVISION

of the

UNIVERSITY OF CALIFORNIA

San Francisco

· ·
Date   · University Librarian

Degree Conferred: . . . . 6/16/91 . . . .

This work is dedicated:

To my mother, whose encouragement has made me feel that dedication conquers all.

To my father, who helped me to recognize my own interests.

PREFACE

This work would never have been possible without the support, guidance, and assistance of numerous people. First, I wish to thank my wife, Penny, whose patience and understanding have allowed me to fulfill my ambitions. My graduate advisor, John Fike, provided me with the opportunity to pursue my interests and served as both a mentor and a friend throughout. Without his guidance, none of this work could have ever been accomplished. Theresa Seilhan provided expert technical assistance in every aspect of this work. Her inimitable care and attention to detail played a most important part in the success of this work. I will be eternally grateful to the numerous teachers whose instruction provided me with the mathematical and analytical tools to complete this and future endeavors, in particular Hugo Martinez, Ken Dill, Vojtech Licko, and Svein Oie. The members of my qualifying examination committee, Dennis Deen, who served as the chairman, Chris Cann, Pak Chan, Kathleen Giacomini, and William Dewey, greatly assisted in the formulation and solidification of many of the ideas herein. Kathleen Lamborn aided in the statistical analyses. Carolyn Scott provided excellent assistance in both the histopathologic studies and the studies validating computed tomography based volumetric methods. Liv Cann, Susan Schoen, Audrey Lee-Rivera, and Debbie Badsky provided expert technical assistance with the computed tomography scans. Warren Lubich assisted in the measurement of tissue and cerebrospinal fluid polyamine levels. Antonio Brito assisted in the measurement of blood iodine levels. Keith Weaver calibrated and supplied ^{125}I seeds for the experiments. Each of the above people were fundamental to the completion of this dissertation, and I doubt if I could ever fully express my gratitude. Nevertheless, I thank all of them for their help, patience, and understanding.
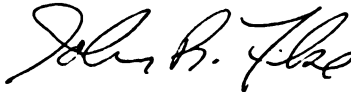
CEREBROVASCULAR RESPONSE TO FOCAL BRAIN IRRADIATION: MODIFICATION BY ALPHA-DIFLUOROMETHYLORNITHINE

by

Glenn T. Gobbel

The cerebral vasculature is thought to play a significant role in the development of radiation-induced brain injury, but few investigations have actually demonstrated an association between alterations in cerebrovascular physiology and radiation-induced damage. This may be due to the extended evolution of such damage (weeks to months) and the lack of non-invasive techniques to sequentially monitor cerebrovascular physiology. For the present study, non-invasive computed tomography-based methods of measuring edema, blood-brain barrier (BBB) breakdown, regional cerebral blood flow, blood mean transit time, and vascular volume were developed and combined with established methods of measuring volumes of tissue necrosis and contrast enhancement. Cerebrovascular physiology was monitored weekly for up to 6 weeks after the implantation of an ^{125}I source into the brain of beagle dogs. Dose was 20 Gy at a point 0.75 cm from the source. Approximately half of the dogs received α-difluoromethylornithine (DFMO), a polyamine inhibitor and potential modifier of blood-brain barrier breakdown, for 2 days prior and 14 days after ^{125}I implantation. The remaining dogs were treated with physiologic saline. Within the saline treated group, tissue necrosis was maximal 3-4 weeks after irradiation, after which the necrotic region became filled in with fibrous tissue and new vessels. Cerebral edema also peaked 3-4 weeks after irradiation, while blood-to-brain transfer of iodinated contrast material increased throughout the 6 week period. Blood flow and vascular volume were reduced for up to 4 weeks after irradiation in the tissue surrounding the region of

necrosis, and there was a significant relationship between increased edema and decreased blood flow. Treatment with DFMO produced an alteration in blood-to-brain transfer, as expected, but also reduced the amount of cerebral edema and altered radiation-induced changes in vascular volume, necrosis volume, and volume of contrast enhancement. There was a significant relationship between alterations in blood-to-brain transfer and cerebral edema, suggesting that DFMO-induced modifications of edema were mediated by its effects on BBB breakdown. The alteration of blood-to-brain transfer, cerebral edema, and necrosis volume by DFMO suggests that cerebrovascular permeability plays a significant role in the development of radiation-induced brain injury.

John R. Fike, Ph.D.

Chairman, Dissertation Committee
Associate Professor in Residence
Department of Neurosurgery

TABLE OF CONTENTS

LIST OF TABLES

LIST OF FIGURES

LIST OF ABBREVIATIONS

AIB	Alpha-amino-isobutyric acid
ANOVA	Analysis of variance
AUC_{PA}, AUC_{ROI}	Area under the time-concentration curve for a peripheral artery or ROI
A', B', α, and β	Parameters describing the bi-exponential fall off in the concentration of iodinated contrast within the blood according to $A'e^{-\alpha t}+B'e^{-\beta t}$ where t is time after bolus administration
A,B,C	Gamma-variate curve fit parameters
BBB	Blood-brain barrier
c	Proportionality constant relating $\Delta CT_{ART}(T)/(1-Hct)$ to $C_P(T)$
c'	Proportionality constant relating $\Delta CT_{ROI}(T)$ to $C_{ROI}(T)$
$C_a(t)$, $C_{aP}(t)$	Concentration within arterial blood and plasma, respectively, at time t
$C_B(t)$, $C_P(t)$	Concentration within brain and plasma, respectively, at time t
C_i	CT number at time i computed from a gamma-variate fit of the measured CT numbers
$C_{In}(t)$	Time-concentration curve describing input of contrast into a ROI
CNS	Central nervous system
$Counts_{Ref}$, $Counts_{ROI}$	Radioactivity of a reference arterial blood sample or a ROI, respectively

$C_{ROI}(t)$, $C_{ROI_i}(t)$	Time-concentration curve within a ROI resulting from any bolus of contrast and from an instantaneous bolus, respectively
CSF	Cerebrospinal fluid
CT	Computed tomography
$\Delta CT_{ART}(t)$, $\Delta CT_{ROI}(t)$	Change in CT number from baseline at time t for a given artery or ROI, respectively
DFMO	α-Difluoromethylornithine
D_T, D_{Ri}, D_R	Total dose of radiation, initial dose rate, and dose rate at some arbitrary time, respectively
ε	Dose rate constant
f_i	Fraction of a region comprised of material i
$f_i(t)$	Function representing the change in CT number within a region due to the movement of the ith contrast molecule through the region
F, F_P	Blood and plasma flow, respectively, through a region in $cm^3 \cdot g^{-1} \cdot s^{-1}$ (or equivalently $ml \cdot g^{-1} \cdot s^{-1}$)
Hct, Hct_C, Hct_{PA}	Peripheral, cerebral tissue, and peripheral arterial hematocrit, respectively
HU	Hounsfield Units
j	Proportionality constant relating peripheral to tissue hematocrit
κ	Decay rate constant for ^{125}I
k	Proportionality constant relating standard deviation of transit times to the mean transit time
K_b	Brain-to-blood transfer or backflux constant
K_i	Blood-to-brain transfer or influx constant

kV_P	Killivolts Peak
μ	Attenuation coefficient
m	Fraction of $<t_{ROI}>-<t_{PA}>$ that is due to the difference between the time the bolus arrives at the region of interest and the time it arrives at the peripheral artery used for determining $<t_{PA}>$
mAs	Milliamp-seconds
M_i	Measured CT number at time i
MRI	Magnetic resonance imaging
n	Lumped factor representing the term $[(1-HCT_{PA})\cdot(1+k^2)]/[2\cdot(1-j\cdot HCT_{PA})\cdot(1-m)]$
n'	Number of data points included in a gamma-variate fit of time-concentration data
P	Permeability in $cm\cdot s^{-1}$
p_aCO_2	Arterial carbon dioxide tension
PET	Positron emission tomography
q	Amount of Contrast
Q_{REF}, Q_{ROI}	Blood flow in $ml\cdot min^{-1}$ into the reference arterial blood sample and ROI, respectively
r	Hypothetical number of contrast molecules within a contrast bolus
rCBF	Regional cerebral blood flow
RE	Ring of Contrast Enhancement
ROI	Region of interest
S	Surface area in $cm^2\cdot g^{-1}$
σ, σ_M	Standard deviation and standard deviation of the mean, respectively

$\sigma_{Ve}^2, \sigma_{PA}^2$	Variance of time-concentration curves for a peripheral artery or vein, respectively
SD	Standard deviation
SD_f	SD of transit times
SE	Standard error of the mean
SPECT	Single photon emission computed tomography
t_o	Time of arrival of a contrast bolus at a ROI
t_r	Transit time of the rth molecule of contrast
V_B, V_{Bl}, V_P	Fraction of a region comprised of brain parenchyma, flowing blood, and plasma, respectively
V_{ED}, V_{IH}	Volume of edema and the hemisphere containing the radioactive source, respectively
Y	Activity of a radioactive source in mCi
∂	Change in CT number within a region due to a single molecule of contrast within the region
$\langle t_f \rangle, \langle t_f^2 \rangle$	Center of gravity of curve describing distribution of transit times, which is equivalent to the mean transit time, and second moment of this same curve, respectively
$\langle t_{PA} \rangle, \langle t_{Ve} \rangle$	Center of gravity of the time-concentration curve of a peripheral artery and vein, respectively
$\langle t_{In} \rangle, \langle t_{ROI} \rangle, \langle t_{ROI_i} \rangle$	Center of gravity of $C_{In}(t)$, $C_{ROI}(t)$, and $C_{ROI_i}(t)$, respectively

INTRODUCTION

RATIONALE

The prognosis for patients with malignant brain tumors is grave; the tumor recurs within two years following therapy in most cases.[1] Post-surgical radiation therapy is the most effective treatment for such tumors,[2] and normal tissue injury is the major limitation to such treatment.[1] Increased radiation dose is associated with an increase in survival of patients with malignant brain tumors,[3, 4] but it is also associated with an increased incidence of complications.[5]

Brachytherapy, in which radioactive sources are implanted directly into a tumor, has been employed to deliver relatively high radiation doses to the tumor while limiting the dose to the surrounding normal brain.[2] Although the results of brachytherapy trials appear promising in terms of patient survival,[1] approximately half of all patients so treated require chronic corticosteroid administration and/or additional surgery to manage the cerebral edema and radiation necrosis which occurs following therapy.[2, 6] Furthermore, long term corticosteroid administration can result in a number of deleterious side-effects including gastrointestinal ulceration and bleeding, loss of muscle mass, and osteoporosis.[7, 8] If the complications associated with brachytherapy could be reduced, larger radiation doses might be used, and the success of this treatment modality thereby increased. In order to develop methods of treating or reducing the complications, the cellular and physiologic factors which are responsible for the development of radiation-induced brain injury must be understood.

The present work focuses on the alterations in cerebrovascular physiology which accompany radiation-induced brain injury and attempts to

determine whether those alterations are responsible for the development of the injury.

HISTORICAL BACKGROUND

Previous Studies of Radiation-induced Brain Injury

The first studies of radiation-induced brain injury, done in the early 1900's, attempted to simply determine how much radiation the normal brain could withstand.[9-11] Radium sources were placed either interstitially or on the brain surface of experimental animals. Dosimetry was crude, and doses were reported as milligram-hours of filtered or unfiltered radium.[9-11] Treatment follow-up focused primarily on clinical symptoms and the histopathologic alterations present at euthanasia, which was generally 1-2 months following irradiation. In general, the findings of these studies were similar: 1) the tissue immediately surrounding the radium suffered severe degeneration; and 2) beyond this was a region in which the neurons and glial cells were spared while the vasculature was severely damaged.[9-11] The vascular damage was manifest as blood vessel congestion, vessel wall thickening, and hemorrhage. Based on these findings, two general conclusions were drawn: 1) below a certain threshold dose, the neurons and glial cells of the central nervous system (CNS) appeared to be resistant to radiation, and 2) changes in CNS tissue that occur in response to doses below the threshold were probably secondary to alterations in the blood vessels.

The importance of the cerebrovasculature was recognized early in the study of brain radiation injury, but the conclusions of these early studies have since been questioned. In the 1930's it was shown that in some instances brain injury became evident only months or years following irradiation[12-15]. Davidoff

et al[13] recognized that this latent period between irradiation and evidence of histopathologic injury was dose dependent. The dose dependency of the latency might explain why the early studies, which used high activity radium sources, failed to observe the latent period and instead observed primarily an acute type of injury. Although some investigators in the 1930's were still attributing radiation-induced brain injury to blood vessel changes, such as Scholz and Hsü[15] who described fibrotic alterations resulting in "blood stream functional disturbances which cause . . . necroses", Ross [16] as well as Davidoff et al [13] were describing histopathologic changes associated with only minimal changes in blood vessels. In those studies, the damage was confined primarily to the neurons and glial cells, and demyelinization was noted in regions dissociated from blood vessel changes. These studies raised two fundamental issues which have been the driving force behind many of the subsequent studies of radiation brain injury. The first issue involves why there is a dose-dependent latent period between irradiation and the expression of radiation injury, and the second involves whether radiation-induced brain injury is due to glial or cerebrovascular alterations.

Regarding the first issue, both neuroglial and vascular endothelial cells have long potential doubling times, which probably results in the extended latent period.[17, 18] Endothelial cells of the adult mouse brain have a growth fraction of 0.3% and cell cycle time of 20 hrs,[19, 20] which would correspond to a potential doubling time of 6-7 months.* Others have estimated the potential doubling times of brain endothelial cells to be greater than a year.[21]

---

* The growth rate constant would be 0.003/20 hrs or 0.00015 hr^{-1}; if there was no cell loss, the number of cells, N, at time t would be $N=N_0e^{(0.00015 \text{ hr}^{-1} * t)}$, where N_0 is the starting number of cells. The potential doubling time is the time at which N would equal $2N_0$ assuming no cell loss, so that $2N_0=N_0e^{(0.00015 \text{ hr}^{-1} * t)}$ and, solving for t, $t=\ln 2/0.00015 \text{ hr}^{-1}$.

Neuroglial cells (considering astrocytes, oligodendrocytes, and microglial cells as a single group) of the adult mouse brain have a growth fraction of 0.4% and cell cycle time of 20 hrs,[19, 20] which would correspond to a potential doubling time of approximately 5 months.[19, 20] Thus, at radiation doses below those causing acute cell death, the expression of damage could be delayed until mitosis and the subsequent mitotic-linked death of either endothelial or glial cells. In addition, there could be a delay because a certain number of cell deaths might be required to produce histopathologic evidence of tissue injury.

The primary target cell of radiation, i.e. the second issue raised above, is uncertain at the present time. If the degeneration of a single cell type could be identified as the primary cause of radiation brain injury, it might be possible to shift the study of radiation brain injury from whole brain to single cell studies and thus better focus the study of radiation injury. This is a strong motivation for trying to identify a primary target cell. The reason that the primary target cell has not been identified appears to be related to the reliance of prior studies on histopathologic results and the failure of these studies to consider the interdependence of cell populations comprising the CNS.

Histopathologic evidence appears to support both of the two hypothesized primary cellular targets of brain irradiation, the glial (primarily oligodendroglial) and the endothelial cell. Before the work of Ross,[16] virtually all the studies suggested that the the vascular system was responsible for injury,[9-11, 20] implying that the endothelial cell was a more likely target than the glial cell. Although a number of the early studies concentrated on acute alterations in the cerebrovasculature following apparently high doses of radiation,[9-11] later studies described such changes at more prolonged times following irradiation.[14, 15] Lyman et al[14] described "severe hyaline degeneration and obliterating sclerosis of arterioles" 5 months after a "dose" of

18 human erythema skin doses directed at the occipital lobe[*]. The studies of Scholz and Hsü[15] described primarily vascular alterations in human patients one and a half years following total brain "doses" of 4 times the erythema skin dose. On the other hand, following the initial evidence suggesting that the glial cell might be the primary target,[16] a number of other studies also demonstrated either demyelination and white matter injury[13, 22-25] or radiation injury unaccompanied by significant vascular changes.[26] These later studies involved both human brain tumor patients[25, 26] and investigations of non-human primate brain.[13, 22, 23, 25] A number of different doses and methods of administration were employed,[13, 22, 23, 25] and demyelination was a consistent finding. In some cases, the demyelination appeared to progress to necrosis of myelin, axons, and/or glial cells.[13, 22, 23, 25] Although alterations in blood vessels were sometimes described,[13] more often only demyelination was seen.[13, 22-24]

The experimental findings demonstrating primarily demyelination and/or white matter necrosis provide strong evidence for the oligodendroglial cell target hypothesis.[13, 22-24] In addition, Zeman and Samorajski[27] have pointed out that if the endothelial cell was the primary target, the gray matter, which has approximately twice the number of capillaries as white matter,[28] would be expected to be more sensitive to radiation, which is exactly the opposite of what experimental results have indicated.[23, 29, 30] It has even been suggested that some vascular alterations might be secondary to surrounding parenchymal changes rather than causes of those changes.[29] However, others have argued against the oligodendroglial cell target hypothesis. Histopathologic evidence

---

[*] One human skin erythema dose was equivalent to an exposure of 800 roentgens [Scholz, 1938 #10].

supporting the endothelial cell target has already been mentioned.[9-11, 15] In addition, Myers, Rogers, and Hornsey[31] point out that there is no known pathologic pathway by which damage to oligodendrocytes alone would produce tissue necrosis. There are existing animal models of demyelination in which tissue necrosis is never seen.[32] In some cases, radiation-induced demyelination may be due to Wallerian degeneration, which is the axonal degeneration and demyelination that sometimes occurs distal to the point of nerve damage, so that demyelination might be caused by ischemic alterations occurring in regions unassociated with the histologic tissue section.[31] Further evidence against the oligodendroglial hypothesis comes from a study on the effects of neutron irradiation on primate brain.[24] In this study, demyelination was seen following irradiation despite there being no apparent loss of oligodendrocytes, which suggests that radiation can cause demyelination without producing oligodendrocyte death. If nothing else, the above findings and conclusions demonstrate the difficulty in identifying a single cell type within a tissue as the target of radiation based on histopathologic results.

The disparity in the histopathologic findings may be clarified, in part, by studies demonstrating that not only the length of the latent period but also the type of damage produced is dose-related.[29, 33] For instance, in rat brain, at doses of approximately 20 Gy, primarily vascular-related alterations were seen with a latency of >12 months.[29] At doses of 25 Gy, alterations were confined primarily to the white matter with latencies of <12 months.[29] At even higher doses, the latent period further decreased accompanied by another increase in vascular damage such as hemorrhage.[33] These findings might explain why the early studies[9-11] using radium applied directly to the brain reported primarily vascular-related alterations. An additional factor that may influence the

character of radiation injury is volume, so that when smaller volumes of tissue are irradiated, there is a shift from white matter to vascular damage.[33]

Although the aforementioned findings may help to explain the apparent discrepancy in histopathologic results, they do not explain the mechanism by which an alteration in the dose or volume of irradiation would lead to an alteration in the character of radiation injury, nor do they answer the question of whether there is a single target cell population for radiation brain injury. An apparent weakness of studies relying only upon histopathology is that they demonstrate changes in cell morphology but reveal little if anything about cell functionality. Studies of cell and tissue function following irradiation might provide evidence of alterations which precede histopathologic changes and might better demonstrate the pathogenesis of the development of radiation-induced brain injury. They might also reveal that the term "latent period" is something of a misnomer. In fact, it has already been demonstrated that alterations in cell function can occur in the absence of and prior to demonstrable tissue necrosis.[30, 34] Rose[30] demonstrated increased uptake of the ^{24}Na in the brain of rabbits exposed to as little as 5 Gy, which is well below the dose associated with morphologic alterations. Delattre et al[34] also noted increased blood-to-spinal cord transfer of alpha-amino-isobutyric acid (AIB) in the rat 30 days following 35 Gy delivered to spinal cord segments T2-T9, which preceded findings of tissue necrosis by approximately 4 months. Whether the functional alterations demonstrated by these two studies play a role in the evolution of radiation injury or are merely consequences of such changes is unknown. However, they demonstrate that morphologic studies do not adequately reveal all the sequelae following brain or spinal cord irradiation.

The findings of Rose and Delattre et al also raise the question of whether there might be important radiation effects on the function of critical cell

populations besides the endothelial cells or oligodendrocytes. For instance, Hopewell et al.[17] noted smooth muscle cell atrophy in the choroid plexus of rats following whole brain irradiation. Changes in the function of smooth muscle cells could conceivably lead to alterations in blood flow and, secondarily, gross tissue damage. In addition, Clemente and Holst [35] demonstrated that alterations in the astrocytes might play an important role in the expression of radiation-induced brain injury. Their study examined radiation-induced histopathologic and blood-brain barrier (BBB) alterations in macaque monkeys 6 hours to 6 months after single doses of 15 to 60 Gy delivered to the whole head. Regions of BBB breakdown were detected with intravenously administered trypan-blue dye, which is unable to cross from the cerebrovasculature into the parenchyma in regions where the BBB is intact. BBB breakdown was observed in all of the animals treated with 60 Gy, none of the animals treated with 15 Gy, and 30-40% of those treated with intermediate doses. The authors noted that regions of BBB breakdown were "co-extensive" with regions of astrocytic degeneration, and, of particular interest, regions of BBB breakdown corresponded to the regions of the most intense neuronal damage. The damage to neurons in those cases were attributed to what Clemente and Holst[35] referred to as the "indirect" effects of radiation on tissue, i.e. secondary effects arising due to alterations in supporting cells. It is apparent from their study that tissue integrity in the brain is dependent upon the inter-relationships of the cellular elements comprising that tissue, which could make it difficult to identify a single cell as the primary target of radiation and cause of tissue breakdown. In a study examining correlated alterations in the morphology of endothelial cells and astrocytes following irradiation of the rat brain, Calvo et al[29] considered the radiation damage of these two cell types to be so closely related that they chose to refer to damage to the "glial/vascular

unit." In an analytical review of target cell theories of radiation injury to the CNS, van der Kogel[33] states that "one cannot analyze the role of one target cell without considering the damage induced in another population. The ultimate expression of tissue damage will depend on the interactions between the different tissue components."

The hypothesis that a change in the function of one cell type can lead to secondary alterations in other cell types suggests that there are factors besides cell survival that may affect the expression of radiation injury. Ascher and Anson[36] demonstrated that one such factor is systolic blood pressure. In their study, hypertension was artificially induced in rats by ligating a renal artery. After irradiation of the cervical and thoracic spinal cord with doses of 15 to 30 Gy, all hypertensive animals showed signs of ataxia and/or died during the 9 month follow-up period. In addition, histopathologic examinations demonstrated vascular lesions in the spinal cord of all the hypertensive rats. In marked contrast, none of the control animals showed evidence of any kind of injury following irradiation. Later, studies by Hopewell and Wright[37] demonstrated that hypertension could also alter radiation injury of the brain. That study combined with those of Rose,[30] Dellatre et al.[34] and Clemente and Holst[35] demonstrate that it is important to consider factors other than cell survival to understand the radiation response of a whole tissue or organ such as brain.

Models have been introduced to account for these other factors that may influence the expression of radiation injury in late responding tissues such as brain and spinal cord.[33, 38, 39] Factors included in the models are not only the radiosensitivity of the cells comprising the tissue but also rate of cell loss of the lethally irradiated cells, proliferative capacity and rate of proliferation of the surviving cells, and the ability of the surviving cells to compensate functionally

for the killed cells.[38] The last factor is in turn dependent upon the functional demand placed upon the cells. Consideration of these factors and the idea that cell types are likely to be dependent on one another for survival might explain the earlier question of why the expression of radiation injury is dose and volume dependent as well as being dependent upon blood pressure. For example, it seems likely that glial and endothelial cells would have not only different radiosensitivities but also different abilities to proliferate in response to injury and functional demands; two different radiation doses would then cause tissue necrosis secondary to alterations in glial function at one dose and secondary to alterations in vascular function at the other. The volume dependence could be explained by the smaller demand placed on surviving cells for proliferation and function when smaller volumes of tissue are irradiated.[40] The effect of arterial pressure on the expression of radiation damage could be explained by greater mechanical stress and functional demand placed on surviving cells at high blood pressure. Other explanations of these phenomena probably exist; nevertheless, the importance of understanding how factors such as functional demand may alter the expression of radiation injury was well understood by Michalowski and co-workers[38] when they stated that such an understanding might lead to post-irradiation manipulations that could modulate radiation-induced tissue injury. In late-responding tissues such as the CNS, post-irradiation manipulations are of particular interest because they might be used weeks or months following radiation therapy, at a time unlikely to interfere with the tumor response.

Alterations in functional demand may be due not only to factors extrinsic to the irradiated tissue, such as blood pressure, but also to intrinsic factors. For example, cell death may stimulate a mitotic response of surviving cells and put increased functional demands on the remaining cells.[41, 42] This is supported

by a study of the turnover of neuroglial cells following irradiation of the rat cervical spinal cord.[41] Rats were given intraperitoneal injections of ^{3}H-thymidine to label mitotically active cells at various time points up to 4 months after irradiation. A pronounced increase in the labelling-index was noted at the 4 month time point, which is just before the onset of cervical cord necrosis and accompanying paralysis. In another study of the radiation response of rat cervical spinal cord, Zeman[43] examined changes in the labelling index of neuroglial cells over a period of several days after the initial labelling. Just before the onset of necrosis, the mitotic index fell from 10% at 3 hours after labelling to 3% three days after labelling, which Hubbard and co-workers attributed to mitotic cell death.[42] The inability of surviving cells to keep up with the increased demand can then lead to further cell death and tissue damage, resulting in an "avalanche" effect.[33, 42] While the surviving cells are proliferating to replace dead cells, they must also compensate for the lost functionality of the dead cells. If the compensation is inadequate, tissue damage could again become progressive.[33, 40] It would appear that cell death and the ability of the surviving cells to compensate for cell death are both important determinants of the amount of tissue injury.

The present study concentrates on the alterations in cerebrovascular function that may be responsible for the progression of tissue injury following brain irradiation. The reasons for concentrating on cerebrovascular rather than oligodendroglial cell alterations are due to a number of considerations. Some of these have already been mentioned and will be reiterated here. First, there is no clear path by which oligodendroglial cell death would lead to the progression of tissue necrosis. In contrast, damage to the cerebral vessels could clearly lead to tissue necrosis through the process of ischemic infarction.[31, 44] In addition, alterations in BBB function resulting from vascular

damage might lead to increased levels of edema, increased interstitial pressure within the brain parenchyma, vascular compression, and further ischemic injury.[31] Lastly, it has been suggested that the presence of cerebral edema may cause myelin damage;[34, 45, 46] thus, vascular damage and the associated BBB breakdown might account for the demyelination seen following irradiation. The need to further study the role of the vasculature in radiation injury was pointed out by Hopewell et al.[17] who stated that the consequence of alterations in the vasculature following irradiation "varies from tissue to tissue and depends on complex adaptations and physiologic relationships which are at present little understood ... A fuller understanding of the reasons for these tissue differences may lead to the development of techniques for preventing or modifying late normal tissue damage after irradiation." In the hope of addressing some of these complex physiologic relationships, the primary questions considered in the present work are: 1) what are the cerebrovascular alterations that occur in response to radiation, and 2) do such alterations influence the expression of radiation-induced injury.

Prior Studies of Post-Irradiation Cerebrovascular Function

There have been only a limited number of studies that have quantitatively assessed alterations in cerebrovascular function, such as blood flow and permeability, following brain irradiation.[34, 46-51] In one of the earliest studies, the right occipital cortex and underlying white matter of eight macaque monkeys were irradiated with 35 Gy; treatment follow-up included sequential monitoring of cerebrospinal fluid (CSF) pressure and a terminal measurement of regional cerebral blood flow (rCBF).[50] At CSF pressures that were 2-3 times pre-irradiation values, marked reductions in rCBF were noted in the edematous white matter. In two monkeys with CSF pressures that were greater than 3

times their pre-irradiation values, rCBF was diffusely reduced throughout the brain. In addition, rCBF was elevated in the regions immediately surrounding the radiation lesions, a finding which is typical of ischemic brain injury. These results are consistent with the earlier stated hypothesis that radiation injury to the brain may be secondary to alterations in blood flow due to edema, increased interstitial pressure, and subsequent ischemia.[31]

In an effort to determine the source of radiation-induced edema, Groothuis and colleagues[47] studied changes in BBB transfer of radiolabeled AIB 7-717 days after the permanent interstitial implantation of 5-7 mCi ^{125}I sources in dog brain. They noted that the resultant lesion consisted of a central necrotic zone surrounded by a region of viable brain tissue with an increased blood-to-brain transfer. The increased AIB transfer was relatively constant between days 7-392, and returned to normal by 716 days. Extensive edema was also noted histologically in dogs that survived up to 392 days but not in those surviving 716 days. Although the cerebral edema was attributed to alterations in BBB permeability as also suggested by others,[34, 46, 52] Groothuis et al[47] pointed out that AIB may be a poor marker of processes associated with edema because it is trapped intracellularly and cannot diffuse very far.[53] This is particularly important because radiation-induced edema following interstitial irradiation can be found in regions distant from the area of BBB breakdown, probably due to the diffusion and bulk flow of proteins from the site of BBB breakdown.[47] Groothuis and co-workers conceded that "the physiological mechanisms of ^{125}I-induced hemispheric edema remain to be studied." Because cerebral edema is one of the primary complications of brachytherapy,[54] this comment emphasizes the importance of studies to elucidate the relationship of cerebrovascular permeability to cerebral edema.

There are at least two reasons for the limited number of studies of cerebrovascular function following brain irradiation. The first is related to the fact that most of the studies done within the past 20-30 years, when methods for evaluating cerebrovascular function existed, were done using external beam radiation at doses of 15-30 Gy. There is typically a long latent period preceding brain injury following external beam radiation at those doses.[55] The long latency makes it imperative to do multiple studies over long periods of time in order to detect subtle alterations in blood flow which might precede morphologic injury; in the case of invasive techniques such as the hydrogen clearance and microsphere methods of blood flow measurement,[56] this generally necessitates using multiple animals. If the most significant cerebrovascular alterations are assumed to occur at some critical time just prior to the onset of morphologic injury, it might seem that the difficulties presented by the long latency could be avoided by limiting cerebrovascular studies to that critical time period. However, the latent period can vary by up to 3 months[50, 55] so that multiple time points would still be required. The second reason is that cerebrovascular radiation injury following external beam radiation is multifocal,[29, 57] which could make it difficult to define precisely the cerebrovascular changes that take place following irradiation. To avoid difficulties associated with the extended and varied latent period, the present study has employed high activity ^{125}I sources that are directly implanted in the brain. The delay prior to the maximal expression of injury is generally shorter (3-4 weeks rather than 3-4 months) and less variable than that seen after external beam irradiation.[52, 58] In addition, the resultant lesion is well-defined making it possible to focus the study of cerebrovascular alterations on a small region of the brain.

To overcome the problems associated with invasive techniques of measurement of cerebrovascular function, a non-invasive method of blood flow measurement was developed for the present study,[59, 60] and a non-invasive method of quantitatively assessing BBB breakdown was derived from a positron emission tomography (PET) method.[61] Although non-invasive methods of rCBF measurement such as PET and single photon emission computed tomography (SPECT) have been available for the past 15-25 years,[62, 63] the resolution of these methods has generally restricted their use to regions of interest (ROIs) of at least 1 cm^3.[64, 65] Therefore, such methods might be unable to detect small regional alterations in cerebral blood flow accompanying radiation brain injury.[29, 57, 66, 67] While PET has been used to study alterations in BBB function following irradiation,[49] the expense associated with PET has limited its availability. Magnetic resonance imaging (MRI) methods have much better spatial resolution than either PET or SPECT, but unfortunately no quantitative methods to measure rCBF have been developed, despite efforts in that area.[68-75] MRI has been used for qualitative detection of BBB alterations following radiation,[49, 76, 77] but the complex relationships determining image intensity[78] have probably limited its use for quantitative studies. Computed tomography (CT), like MRI, has good spatial resolution and is widely available. Unlike MRI, the relationships determining image intensity following the administration of contrast media appear to be more straightforward. For example, the change in CT image intensity, measured in Hounsfield Units (HU), following administration of an iodinated contrast agent is directly proportional to the amount of agent within the tissue of interest.[79] For these reasons, CT was chosen over PET, SPECT, and MRI as a method for the measurement of rCBF and BBB breakdown.

CT has already been used for measurement of blood flow in a number of other organs, including liver,[80] kidney,[81] cardiac muscle,[82] and brain.[83] The technique used for brain consists of a series of CT images of a given section of brain obtained during the inhalation of xenon gas, which is radiodense and thus serves as a contrast agent. Regional CBF is then determined from the rate of uptake of the gas into the tissue, which can be determined from changes in image intensity. Unfortunately, spatial resolution of the xenon CT technique is limited to ROIs of greater than 1 cm^3.[83] Axel[84] proposed a dynamic CT method for assessing rCBF, in which a series of CT images is obtained during the passage of a bolus of iodinated contrast agent through the brain. Changes in contrast concentration as a function of time can be determined from the CT images, and rCBF-related information can be derived from these changes based on indicator dilution theory.[84-86] Previous studies attempting to utilize dynamic CT to measure blood flow were limited by scan acquisition times and interscan delay times of 1.5 -2.0 seconds and greater.[85, 86] The development of the ultrafast CT scanner, with acquisition times of 50-100 msec and interscan delay times of 0.6 seconds, has reduced these limitations.[87] However, despite the use of the ultrafast scanner to measure blood flow in a number of organs, the development of an accurate means for estimating blood flow within the brain with such a scanner had not been established prior to the present work.

Determination of the cerebrovascular changes associated with radiation damage is most useful if one can distinguish which of the changes actually mediate the injury. One method of accomplishing this would be to specifically modify one of the cerebrovascular changes and see if the injury is also modified. Such modifications might be induced by the administration of drugs which affect either rCBF or cerebrovascular permeability. Although there are no known examples of studies using agents to modify rCBF following irradiation,

there are examples in which brain irradiation was followed by the administration of agents which modify cerebrovascular permeability.[48, 51] Joó and colleagues[48] studied BBB leakiness after the implantation of [90]yttrium sources and administration of metiamide, a histamine H_2 receptor blocker. BBB damage was quantified at 24 or 72 hours after implantation by the extent of tissue staining by Evan's blue dye, which in a normal brain is confined to the cerebrovasculature. They noted significantly reduced staining in the metiamide-treated animals. In addition, they reported that, unlike saline-treated controls, metiamide-treated animals showed no clinical signs of edema such as somnolence or apathy. Although the amount of edema was not quantified, the apparent association of altered BBB damage with an altered extent of edema strongly suggests that changes in cerebrovascular leakiness are not end results of radiation damage but actually play a role in the evolution of such damage.

Similarly, Warnke and co-workers[51] studied the effects of dexamethasone on radiation injury induced in dog brain by the interstitial implantation of radioactive sources. After 3 days of treatment with dexamethasone, the investigators noted a reduction in the blood-to-brain transfer constant, which was accompanied by an increase in rCBF in the edematous region. One implication of this study is that alterations in BBB function are associated with alterations in rCBF.

Another agent which has been found to modify cerebrovascular permeability is α-difluoromethylornithine (DFMO).[88-92] DFMO is an inhibitor of ornithine decarboxylase, a key enzyme involved in the formation of the polyamines putrescine, spermidine, and spermine from the amino acid ornithine.[93] Following creation of a focal cryogenic lesion in rat brain, it was found that there was a significant increase in polyamine levels within the lesion, whereas there were no or minimal alterations in polyamine levels outside the

lesion. The injury was accompanied by an increase in BBB permeability signified by abnormal leakage of fluoroscein from the cerebrovasculature into surrounding tissue. DFMO administered 10 minutes prior to induction of the cryogenic lesion prevented the subsequent increases in polyamines and cryogenic injury; the administration of putrescine abolished the effects of DFMO. Because DFMO appeared to affect permeability, it was suggested that the compound might also be useful in reducing cold-injury induced edema. Furthermore, in a model of ischemic injury in cat brain, it was found that DFMO pretreatment resulted in a reduction in Evan's blue dye staining of the ischemic region and a "significant return to control values for specific gravity",[94] suggesting that permeability changes were accompanied by alterations in edema.

Based on the above studies, DFMO appears to be a promising agent for the alteration of radiation-induced cerebrovascular permeability and the subsequent edema. DFMO reduces radiation-induced alterations in the permeability of endothelial cell monolayers,[95] but there are no known studies of the effect of DFMO on both radiation-induced permeability and subsequent radiation-induced tissue damage. In the present work, DFMO is used as a cerebrovascular permeability modifying agent in order to determine how such a modification might alter subsequent radiation brain injury.

SUMMARY

There are a number of compelling reasons to examine the role of the cerebrovasculature in radiation brain injury. Despite the importance and relevance of determining the primary target cell responsible for radiation-induced brain injury, efforts toward this end have been unsuccessful to date. Reasons for the lack of success include the lack of emphasis as well as

techniques to study the variety of factors that play a role in the expression of radiation injury within a complex tissue or organ.[38] One important factor is the interdependence of the various cell types within a tissue. Because of this interdependence, a loss or reduction of function of one type can potentially lead to the death of another type. Perhaps the clearest example of this is the role of endothelial cells in maintaining the vasculature and nutrient supply of all other cells within a tissue. Despite the obvious importance of the vasculature to tissue integrity, it has been difficult to determine what role the cerebral vasculature might play in the expression or radiation brain injury based on histopathologic results. Although studies of *in vivo* cerebrovascular function should avoid some of the inherent limitations of histopathologic studies, there have been only a limited number of such studies.

The present study was designed to elucidate the changes in cerebrovascular physiology that mediate cerebral edema and radiation injury. The design of the study was based on the hypothesis that radiation-induced BBB damage leads to cerebral edema, ischemia, and, in turn, tissue necrosis. To sequentially study the changes in cerebrovascular function following irradiation, non-invasive CT methods for the quantitative determination of blood flow, blood-to-brain transfer, and cerebral edema were developed. Following development of these methods, a well-described beagle model of radiation brain injury[52, 58] was used to non-invasively study cerebrovascular parameters and tissue injury following irradiation. In this model, radiation injury is manifest on CT images as a focus of low density surrounded by a ring of tissue that is characterized by profound enhancement by conventional iodinated contrast medium (Figure 1). The enhancement delineates a region of BBB breakdown.

Figure 1   Transverse, contrast-enhanced CT scan of dog brain 2 weeks

post-irradiation   with a single ^{125}I source. Radiographic characteristics of the

focal radiation lesion include an area of necrosis (N), visible as a region of low

density centered around the site of implantation of the radioactive source,

surrounded by a ring of contrast enhancement (RE). Diffuse edema (arrows)

can be visualized on the scan by the low density throughout the hemisphere.
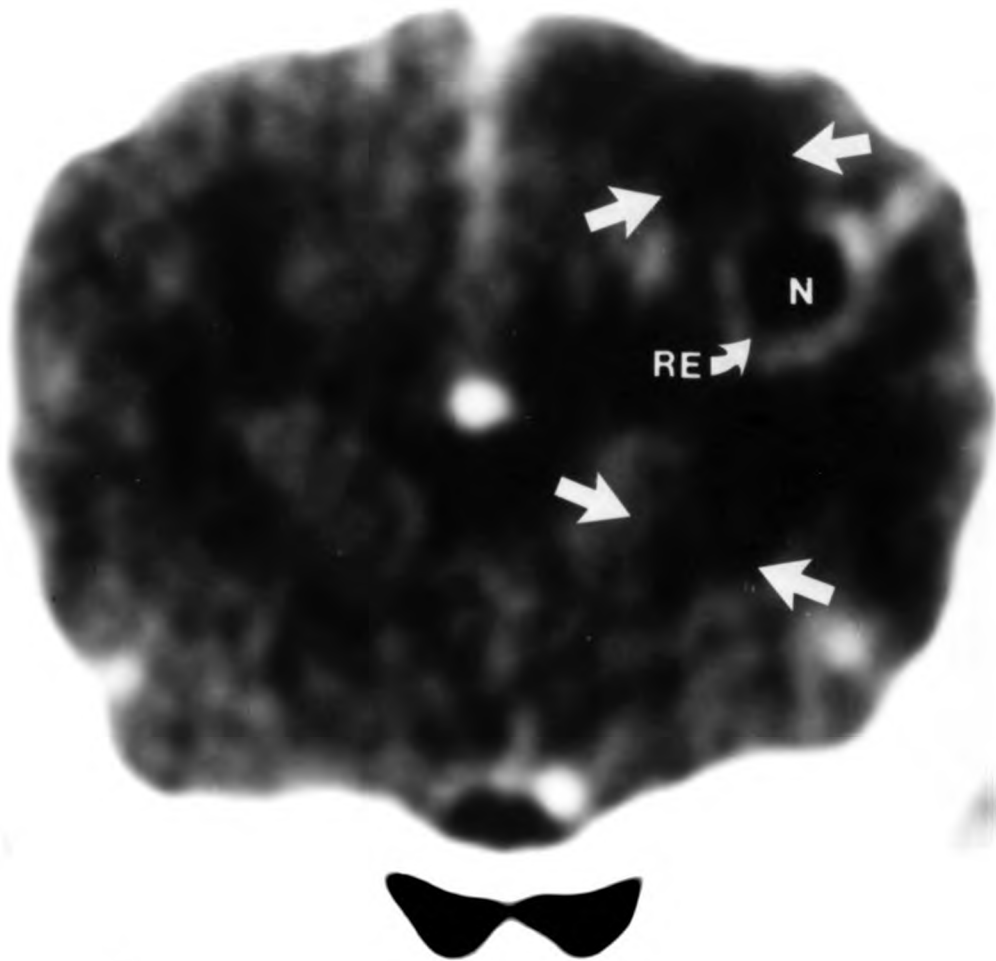
Diffuse low density is also observed within and outside of this region of BBB breakdown. Histologically, the focus of low density corresponds to necrosis, the ring of contrast enhancement (RE) corresponds to the region at the interface of necrosis and surrounding non-necrotic tissue, and the diffuse low density corresponds to vasogenic edema. Following irradiation, changes in rCBF, vascular volume, mean transit time of blood, blood-to-brain and brain-to-blood transfer of iodinated contrast, edema volume, and volumes of necrosis and contrast enhancement were non-invasively quantified weekly with CT for up to 6 weeks following the implantation of ^{125}I sources into the white matter of 9 adult beagle dogs. In addition, tissue and CSF polyamine levels were assessed 2, 4, and 6 weeks after irradiation. To assess the role of cerebrovascular permeability in the subsequent radiation-induced tissue injury, DFMO was administered at a dose of 150 mg/kg for 2 days prior and 14 days post-irradiation in an additional 7 dogs, and the ensuing changes in the aforementioned measures of cerebrovascular function, tissue injury, and polyamine levels were determined.

METHODOLOGY, VALIDATION, AND RESULTS

METHOD OVERVIEW

Animals

All studies involving experimental animals were carried out using male and female purebred adult beagle dogs approximately one year of age. The dogs were purchased from a commercial supplier and housed under standardized conditions. They were given routine veterinary care including the prophylactic administration of anthelmintics for intestinal parasites and vaccinated against distemper, hepatitis, leptospirosis, parainfluenza, and parvo virus. Dogs were anesthetized for all surgical and imaging procedures. Preanesthetics included atropine sulfate (0.05 mg·kg^{-1}) and acepromazine maleate (0.25 mg·kg^{-1}) administered subcutaneously 20-30 minutes before induction. General anesthesia was induced with sodium thiamylal (4% to effect) given through an 18-20 gauge catheter placed in a cephalic vein. After endotracheal intubation, anesthesia was maintained either with supplemental boluses of thiamylal (CT studies of blood flow and blood-to-brain transfer constants) or with a mixture of methoxyflurane gas and oxygen (see Appendix I. General Anesthesia for details).

All irradiated dogs (see below) were given a general physical and neurologic exam one week prior to irradiation and weekly thereafter. The neurologic exam was done to determine the effects of focal radiation injury on sensory and motor function and incorporated subjective assessments of response following naturally occurring or induced stimulation. Included in the neurologic exam were evaluation of proprioceptive and nociceptive reflexes, righting and placing reactions and assessment of cranial nerve function.

CT-Based Measurements

<u>Volumes of Necrosis. Contrast Enhancement. and Edema</u>   Volumes were measured using a GE 9800 CT scanner (General Electric Medical Systems, Milwaukee, Wisconsin). After induction of general anesthesia, the dog was placed in sternal recumbency with head extended onto a plastic head rest within the gantry of the CT scanner (Figure 2). A CT number calibration phantom containing tubes filled with water, saline, 10% serum albumin, and mineral oil was positioned under the head during scanning.[52, 55, 58] A lateral computed radiograph of the skull was obtained in order to select the appropriate levels for scanning.

For the CT studies of edema volume, 20 contiguous 3 mm thick transverse CT scans were obtained in approximately 5 minutes. The head was scanned from the tentorium of the cerebellum to the cribriform plate using contiguous, 3 mm thick sections, technique factors of 140 kV_P, 100 mA, and 4 s exposures. Images were reconstructed on a 320 X 320 matrix with a pixel size of 0.488 mm.

For determination of edema volume, three ROIs were drawn on each of the 20 scans·using a manually-directed, trackball-guided cursor. The first was drawn as a circle approximately 1 cm in diameter around the water within the calibration phantom. The last two ROIs were drawn around the left and right hemisphere. In drawing these ROIs, it was important to exclude the tissues close to the bone-brain and brain-ventricle interface due to the artifacts present adjacent to such interfaces.[96] To accomplish this, contrast within the image was maximized by setting the window of visible CT numbers on the computer console equal to the range of CT numbers within the brain and by setting the level equal to the center of that range. The hemispheric ROIs were then drawn

Figure 2   Photographs demonstrating positioning of dog within the 9800 General Electric CT scanner. Note that the dog is in sternal recumbency and maintained on methoxyflurane/O_2 gas anesthesia during scanning. The head is fixed in place with velcro straps within a plastic holder with a standardized water, mineral oil, albumin, and saline filled calibration phantom (closed arrows) placed beneath the head. A jacket (open arrows) containing an infusion pump for intravenous administration of DFMO or saline is also visible.
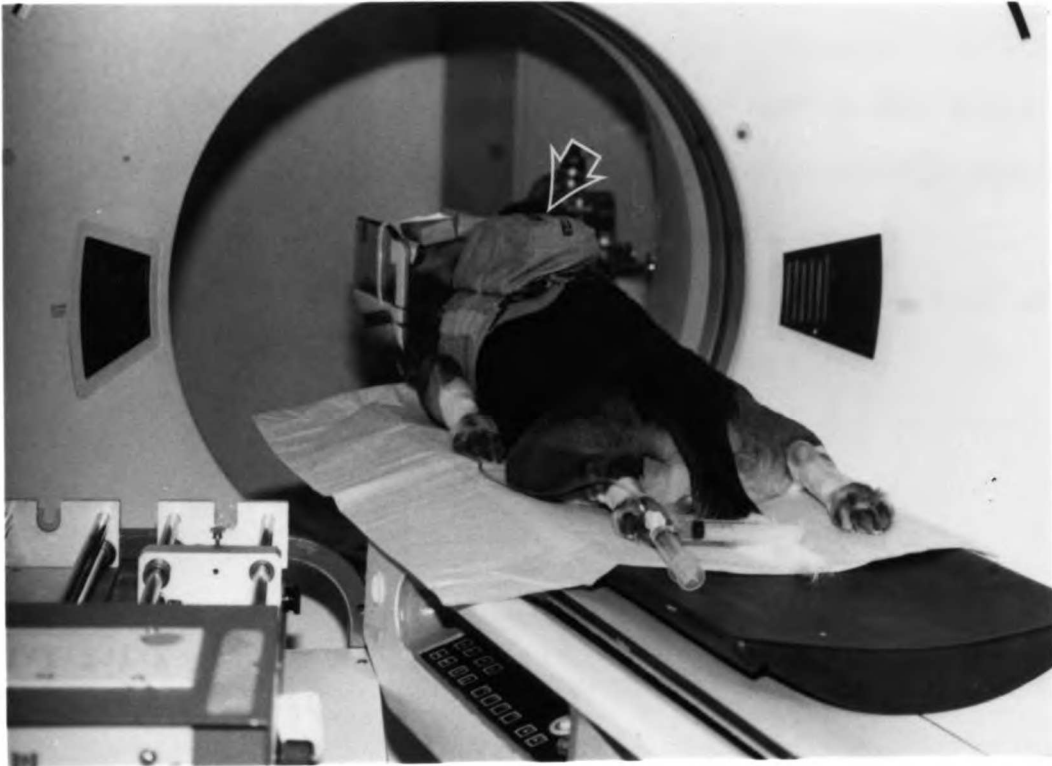
in such a way that the ventricles, the radiation lesion, and a 1.5-2.0 mm margin surrounding the bone-brain, brain-ventricle, and brain-lesion interfaces were excluded. When a radiation lesion was excluded from an ROI drawn around one hemisphere, a comparable region was excluded from the contralateral hemispheric ROI.

The volume (V) of edema (ED) within each tissue section was then calculated according to the equation

$$V_{ED} = V_{IH}(CT_{IH} - CT_{CH})/(CT_{H2O} - CT_{CH})$$ (1)

where CT_{IH} is the CT number of the hemisphere containing the focal radiation lesion (i.e. the irradiated hemisphere-IH), CT_{CH} is the CT number of the contralateral hemisphere, and CT_{H2O} is the average CT number of the water within the phantom (see Appendix II. Measurement of Edema Volume using CT). V_{IH} was determined from the scan thickness and number and size of pixels within the ROI within the irradiated hemisphere.

Immediately after completion of the CT scanning for edema measurement, the dog was scanned for measurement of volumes of necrosis and ring enhancement. Iodinated contrast medium (Na/meglumine-iothalamate, Conray 400® Mallinckrodt, Inc., St. Louis, MO) was infused intravenously using a Harvard infusion pump at 7 ml·min⁻¹ for 3 minutes and then at 2 ml·min⁻¹ for at least 2 minutes and during scanning in order to maintain relatively constant blood iodine levels.[52] Five minutes after the start of infusion, 5 contiguous 3 mm thick transverse CT scans were taken. The five scan levels were based on the pre-contrast images and chosen so as to encompass the focal radiation lesion. Technique factors and image reconstruction were the same as for CT-based edema measurement studies.

The scan levels included the level of the twist drill hole in the skull used for ^{125}I implant and two scans both rostral and caudal to this level. The CT studies of volume of necrosis and contrast enhancement immediately followed the edema volume study.

During image analysis, image contrast was maximized as in the edema volume analysis. The focal lesion was readily visible on the contrast enhanced images in virtually all cases; the lesion appeared as a focally low dense area (referred to as necrosis) surrounded by a ring of contrast enhancement (Figure 1). ROIs were drawn around the regions of necrosis and RE using the manually-directed trackball-guided cursor, and the number of pixels within each ROI noted. Total volume of necrosis and RE were calculated from these values by summing values from one or more CT scans based on the pixel width (0.488 mm) and slice thickness.

Transfer Constants, Blood Flow, Transit Time, and Vascularity Measurements were made using a C-100XL ultrafast CT scanner (Imatron Inc., South San Francisco, California). Dogs were anesthetized and placed within the scanner with the calibration phantom as for the CT-based volumetric measurements. In order to select the appropriate level for scanning, a lateral computed radiograph of the skull and scout transverse images were obtained. The scan level containing the twist drill hole for ^{125}I was chosen.

For the determination of transfer constants, a 20 ml bolus of iodinated contrast agent (Conray 400®) was injected into a cephalic vein at a rate of 7 ml/second using a mechanical injector (Medrad, Mark IV, Pittsburgh, Pennsylvania). A series of 40 CT scans was initiated at the beginning of the injection using interscan delays of 30 seconds for scans 1-2, 15 seconds for scans 3-20, and 60 seconds for scans 21-40. Scan duration was 0.2 seconds. Scan thickness was 6 mm. The scanner was operated at 130 kV$_P$ and 126

Figure 3   CT images of irradiated dog brain illustrating the various regions of interest in which blood flow and blood-to-brain transfer constants were measured. The regions outlined are: A) lesion, B) brain surrounding lesion, C) white matter, and D) gray matter. Region A was also used for determination of transfer constants and V_P.
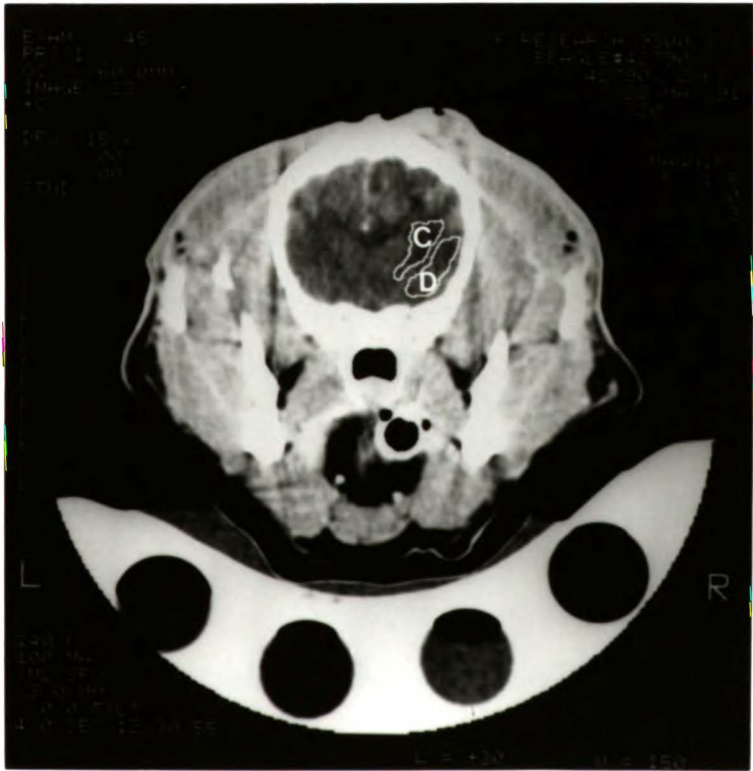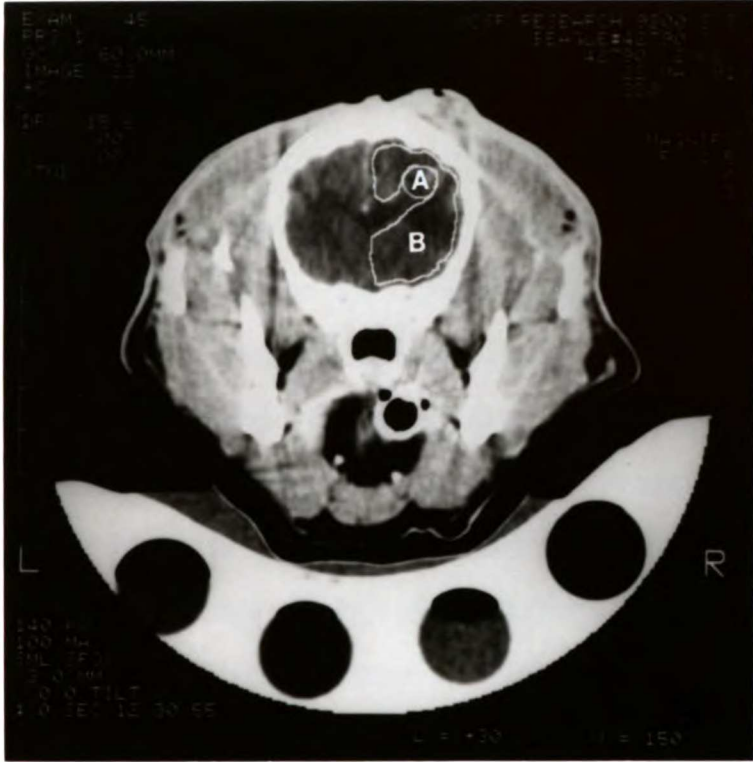
mAs. Images were reconstructed on a 360 X 360 matrix, and pixel size was 0.5 mm. A 1 ml intravenous blood sample was obtained from a saphenous vein at the completion of scanning for determination of peripheral hematocrit (Hct).

For the analysis, a manually directed trackball-guided cursor was used to outline a ROI that encompassed the entire focal lesion (i.e. necrosis and RE) (Figure 3). The size, shape and placement of the ROI for each dog was the same from week to week and was dictated by the lesion characteristics seen during the two week volumetric CT study. The location of the ROI was based on bony and soft tissue landmarks, including location of the twist drill hole used for implantation of the ^{125}I source, the vein of the corpus callosum, and the lateral ventricle. The CT number for the ROI was obtained from each scan, and the change in CT number (ΔCT_{ROI}) for scans 2-40 was calculated relative to scan 1. Two pixels, one in the left and one in the right lingual artery, were used to determine the change in CT number of an artery, ΔCT_{ART}. To minimize any inaccuracy of ΔCT_{ART} values due to volume averaging (inclusion of non-arterial tissues in the arterial ROI), the pixels with the greatest increase in CT number over baseline were chosen.

The value of each of the transfer constants and plasma vascular volume were obtained from the equation

$$\Delta CT_{ROI}(T)(1\text{-Hct})/\Delta CT_{ART}(T)$$
$$= K_i(1\text{-}V_P/(1\text{-}0.5\text{Hct})\ (\ \int_0^T \Delta CT_{ART}(t)e^{K_b(t\text{-}T)}dt/\Delta CT_{ART}(T)) + V_P \qquad (2)$$

where K_i is the blood-to-brain or influx constant, V_P is the volume of the ROI occupied by plasma within the cerebral vasculature, and K_b is the brain-to-blood transfer or backflux constant (see Appendix III.

Theory of Transfer Constant Determination for details). This equation is in the form of the equation for a straight line, y=mx+b, where m represents the slope of the line and corresponds to K_i, and b represents the intercept and corresponds to V_P. K_b was obtained using an iterative method (see Appendix IV. Iterative Algorithm for K_b Determination) to obtain the best linearity of the experimentally determined points, and V_P and K_i were then calculated from the intercept and slope, respectively, of the line obtained using a least-squares fit.[61]

In the initial pilot studies of blood flow parameters within normal dog brain, the level chosen for measurement was the same as that used for ^{125}I implant (see Appendix VIII. [125]I Implant and Removal #7). For dogs with ^{125}I lesions, the blood flow measurement was done 5-10 minutes following the end of the permeability measurement. A 15 ml bolus of iodinated contrast agent (Conray 400®) was injected into a cephalic vein at a rate of 5 ml/second using a mechanical injector (Medrad, Mark IV, Pittsburgh, Pennsylvania). A series of 20 CT scans was initiated at the beginning of the injection using interscan delays of 2.0 seconds for scans 1-3 and 0.8 seconds for scans 4-20. Scan duration was 0.1 seconds. Scan thickness was 6 mm. The scanner was operated at 130 kV_P and 63 mAs. Images were reconstructed on a 360 X 360 matrix, and pixel size was 0.5 mm.

To select the best image for delineating brain morphology, an elliptical ROI encompassing most of the brain was drawn, and the average CT number of the pixels within the outlined regions was determined for each of the 20 scans and plotted *versus* time. Based on this plot, the scan at which the CT number peaked within the brain was determined and used for subsequent ROI analysis. The various regions of the brain appeared to be most easily visualized on this image. The image contrast was maximized as for the edema volume analysis (see above).

A manually directed trackball-guided cursor was used to outline ROIs within the CT images. The regions used in normal dogs included the left and right internal capsule, neocortex, basal ganglia, and hemisphere. These regions were well-defined anatomically on the CT images, thus minimizing operator influence on the choice of the region boundary (Figure 4). In dogs treated with radiation, regions used included the lesion (i.e. the necrosis and region of contrast enhancement as described above), the entire hemisphere excluding the lesion (as described in the measurement of edema), the white matter region of the internal capsule ventral to the region of the lesion, the gray matter region of the neocortex just lateral to the white matter region, and comparable regions within the contralateral hemisphere (Figure 3).

In order that measured rCBF would reflect parenchymal rather than pial blood flow, care was taken to insure that ROIs containing peripheral gray matter, such as the hemisphere and the neocortex, were drawn so that overlying pial vessels were largely excluded. To accomplish this, use was made of the finding that pixels within vessels tended to have a large maximal rise in CT number; pixels that were within 5 mm of the brain surface, ventricles, or mid-sagittal sulcus and had a maximal rise in CT number exceeding the maximal rise in CT number of deeper brain tissue were excluded from ROIs.

To minimize averaging of the arterial volume with the surrounding parenchyma, the single pixel within the left or right lingual artery that showed the greatest rise in CT number was determined from the automatic gamma-variate curve fit routine (see below), and this pixel was used as the arterial ROI. In similar fashion, in an arbitrary group of the normal dogs, a single pixel was selected within the vein of the corpus callosum for determining k in Equations V.13 and V.14. The average CT number of the pixels within the outlined

Figure 4   One of 20 CT images of the dog brain used for comparing ultrafast CT measurements of rCBF to microsphere measurements. Similar ROIs were used in the study comparing ultrafast CT measured rCBF to xenon CT measured rCBF. Outlined are the various regions of interest used including A) basal ganglia, B) internal capsule, C) neocortex, and D) lingual artery.
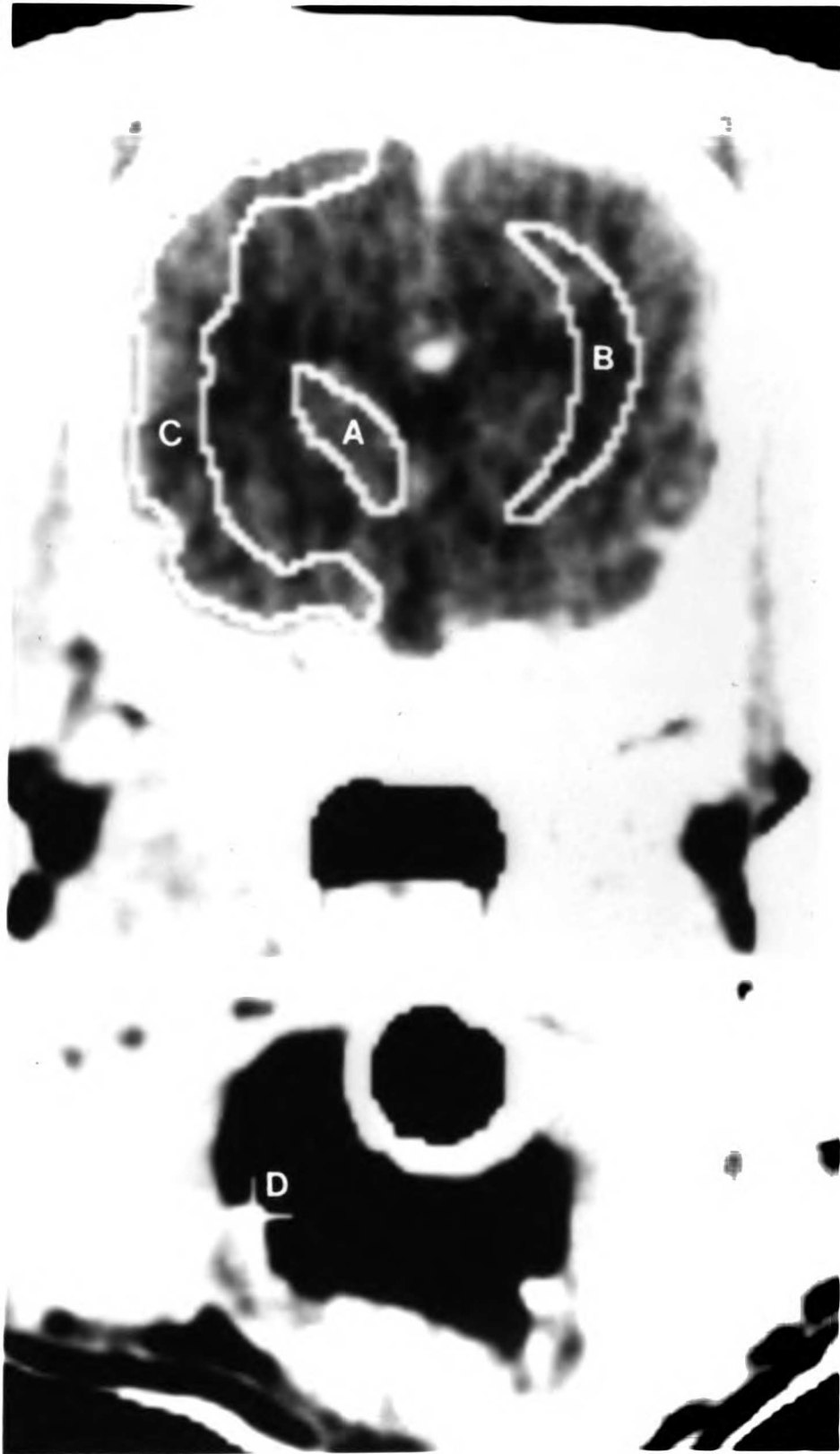
regions was determined for each of the 20 scans and plotted *versus* time (Figure 5).

A gamma-variate curve of the form $\Delta CT(t)=C(t-t_0)^A e^{-(t-t_0)/B}$, where $\Delta CT(t)$ is the change in CT number from baseline at time t and A, B, C, and t_0 are parameters obtained from the curve fit, was then automatically fitted to the data by the scanner software. The curve fit was initiated at the point that the CT number increased to 15% (for neocortex, hemisphere, gray matter, venous, and arterial ROIs) or 30% (for basal ganglia, internal capsule, lesion, and white matter ROIs) of the maximal rise in CT number and was terminated at the point when the CT number fell back to 50% of the maximum. The reason for using different initiation points for the fit was related to the lower maximal rise in CT number and greater noise in the data from smaller ROIs (i.e. the basal ganglia) and ROIs with lower flow (i.e. the lesion and white matter) (see below).

For use in the actual calculation of rCBF, parameters characterizing the fitted curve, A, B, C, and t_0 as well as area under the curve (AUC), center of gravity of the curve <t>, and peak increase in CT number, were automatically displayed adjacent to the CT image. The rCBF, mean transit time, $<t_f>$, and vascularity, V_{BI}, were then calculated according to the formulae (see Appendix V. Theory of Blood Flow Determination)

$$rCBF= V_{BI}/<t_f> \tag{3}$$

$$V_{BI} = [(1-HCT_{PA})/(1-j \cdot HCT_{PA})] \cdot [\ AUC_{ROI}/AUC_{PA}] \tag{4}$$

$$<t_f>=[2 \cdot (1-m)/(1+k^2)] \cdot (<t_{ROI}>-<t_{PA}>) \tag{5}$$

Figure 5   Time-concentration data obtained for the region of the neocortex. Each open box corresponds to the concentration of indicator (i.e. CT number) within the ROI at that particular time after the start of injection. The line passing through the open boxes is the gamma-variate curve fitted using a least-squares approximation. The carat at approximately 10.5 seconds corresponds to the time of maximal concentration of indicator within the ROI and is equal to the time of acquisition of the image used for drawing the neocortical ROI.
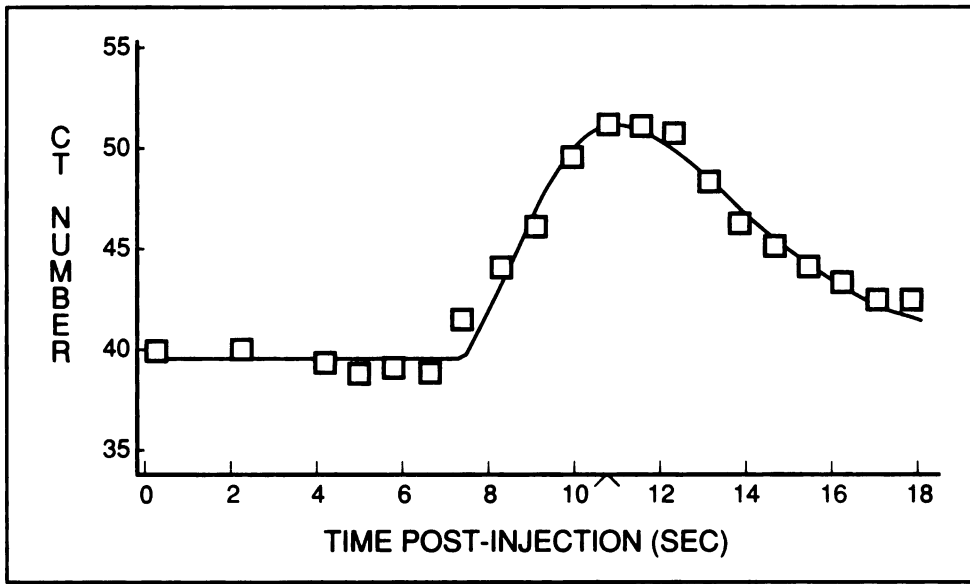
CT-BASED MEASUREMENT DEVELOPMENT AND VALIDATION

CT provides a method to non-invasively measure the x-ray attenuation coefficients of the regions comprising a cross-section of tissue. These x-ray attenuation coefficients can be translated to a corresponding gray scale, and the coefficients of the section viewed as a conventional CT image. Regional variations in the attenuation coefficient are then evident within the image as variations in image brightness, with greater brightness typically corresponding to a higher attenuation coefficient.

The attenuation coefficient of a region is a function of the probability with which a photon passing through the region is either absorbed by the photoelectric process or scattered by the Compton process.[97] This probability is determined by both the photon energy and the atomic composition of the region.[97] The attenuation coefficient is measured by determining the proportion of incident photons that are transmitted through the region.[97] The region's CT number in Hounsfield Units (HU) is then derived from this attenuation coefficient, μ, of the region (T) and that of water according to the formula[97]

$$HU = 1000(\mu_T - \mu_{H2O})/\mu_{H2O} \tag{6}$$

Because regional attenuation number and hence CT numbers are a function of the atoms comprising the tissue, changes in tissue composition can be evaluated by monitoring alterations in CT number. This makes it possible to measure alterations such as changes in brain water content that might accompany cerebral edema. In addition, because contrast agents that enter the region can cause marked alterations in the attenuation characteristics of the tissue, it is also possible to use CT to study the dynamics of accumulation and

washout of such agents. This is the basis of using CT to measure blood flow and blood-to-brain transfer.

It should be noted out that there is some uncertainty in measurements based on changes in CT number. Because any measurement of attenuation must be based on a finite number of photons, there is imprecision or "statistical noise" associated with such a measurement and therefore inaccuracy in the derived CT number. As the number of photons used in the measurement is increased, the precision will increase.[97] However, to use CT numbers effectively, it is important to have some quantitative appreciation of their precision.

One method of determining precision associated with measurements of CT number is to examine the CT numbers of a homogeneous region, such as a water-filled phantom. In theory, CT number of the water should be the same throughout the region, but in practice there will be some fluctuation in the number due to statistical noise. The standard deviation, σ, of the values gives a measure of the spread of values or noise associated with any CT number measurement. The uncertainty in the measured CT number for a ROI is determined by the uncertainty of the mean, σ_M, of CT numbers for the region. If there are N CT numbers corresponding to N pixels within the ROI, this uncertainty can be estimated from the expression[98]

$$\sigma_M \approx \sigma/N^{1/2} \tag{7}$$

Because the variation in CT numbers within an image is not random, this equation actually overestimates the standard deviation of the mean and should be considered as the upper limit of the true value.[97] The equation is accurate for long, narrow, rectangular ROIs in which the area is increased only by

increasing the length of the longer side.[98] However, for circular ROIs of increasing area, σ_M decreases proportional to $1/N^{3/4}$.[98] Therefore, for irregularly shaped ROIs, σ_M would be expected to be proportional to $1/N^x$ where x would be between 1/2 and 3/4.

The theory and/or methodology of the CT-based measurements of volume of necrosis, contrast enhancement, and edema as well as blood-to-brain and brain-to-blood transfer, blood flow, mean blood transit time, and vascularity were developed and/or validated as outlined below.

Region of Interest Volumes

To assess the accuracy of volumetric measurements of small ROIs, such as those used for determining volume of necrosis or contrast enhancement, a CT phantom study was done utilizing a water-filled plastic phantom within which was a second fluid filled compartment roughly the size of the dog brain. Within the smaller compartment there was a series of glycerol filled cylinders whose diameters ranged from 2 to 6 mm based on the diameter of the drill bits used in creating the cylinders; therefore, for a 3 mm thick scan, cylinder volumes were expected to range from 0.0094 - 0.0848 cm^3. The phantom was placed within the CT gantry and scanned using radiologic technic factors comparable to those used for the *in vivo* studies. The differences between the cylinders and surrounding fluid were less than 100 CT numbers, which was comparable to the CT number differences between the regions of necrosis, RE, and surrounding brain. Volume measurements of the glycerol filled cylinders were made using the trackball guided cursor to outline the cylinders. Cylinder volume was calculated based on the number of pixels within the outlined region, pixel size (0.488 mm), and scan thickness. CT measurements were compared to the expected volumes of the cylinders. The accuracy of the CT trackball method for

analysis of small volumes was demonstrated by a highly significant correlation (R=0.99) between CT measured volume and expected volume (Figure 6).

Cerebral Edema

To assess the validity of the CT-based method of volume of edema analysis, the CT results were compared to water volume calculated from the wet and dry weights of tissue. For 14 dogs, 3 cross sectional slices of brain, approximately 3 mm thick and comparable to 3 CT sections taken 6-15 mm caudal to the focal lesion, were divided along the midline into left and right halves. The halves were weighed, dried at 100°C to constant weight, and reweighed. Per cent water in each half was calculated as [100% · (wet weight - dry weight)/wet weight], and volume of excess water determined. For each slice, excess water volume was calculated as $[(\%H_2O_{IH}-\%H_2O_{CH})/100] \cdot V_{IH}$, where $\%H_2O$ is the percent water in the irradiated (IH) or contralateral (CH) hemisphere and V_{IH}, the volume of the irradiated hemisphere, was determined by dividing its wet weight by brain density (1.03 g/ml). For each dog, the total amount of excess water in the three tissue slices was compared to the total amount of excess water calculated from the CT images.

A significant correlation was seen when CT-based determinations of edema volume were compared to wet-dry weight based measurements (R=0.71, Figure 7). However, the slope of the least-squares regression line relating CT-based measures to the wet-dry measures was significantly less than one, indicating that the CT-based volumes were greater than the wet-dry volumes. The reason for this difference is that the CT method depends upon overall changes in x-ray attenuation within the irradiated hemisphere, and such changes may be due to a variety of factors in addition to increased water, such as the leakage of plasma proteins and breakdown of tissue lipids. Therefore,

Figure 6   Comparison of CT derived volumes (mean ± standard deviation) to expected volumes within a standard phantom. The expected volumes were calculated from the known thickness of the CT sections (3 mm) and the size of the bits used to drill the holes in the phantom. There were from 4-6 holes within the phantom at each of the different volumes. There is a strong correlation (R = 0.99) between the two measurements; the line of unity is shown for comparison.
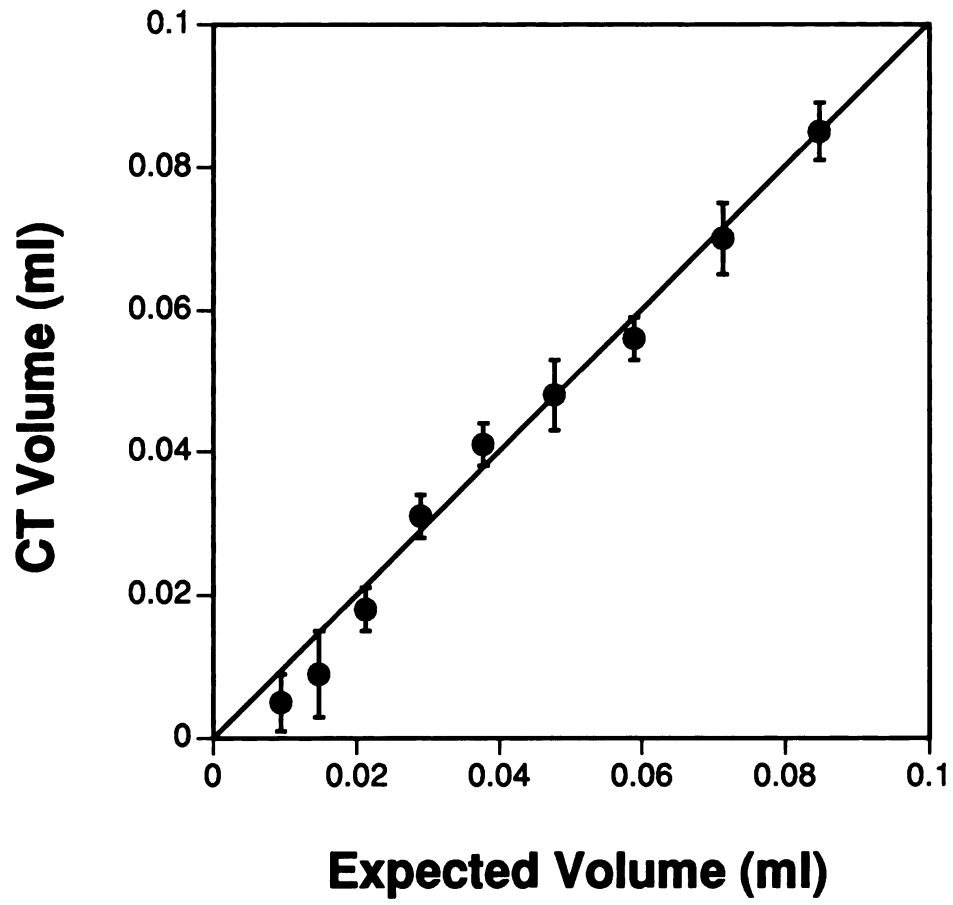
Figure 7   Comparison of CT derived volume of edema and volume of excess hemispheric water based on wet/dry weight determinations. There is a significant correlation between the two methods (R=0.85). The line represents the least-squares line of regression (Wet/Dry Volume = 0.26·CT Volume + 0.05).
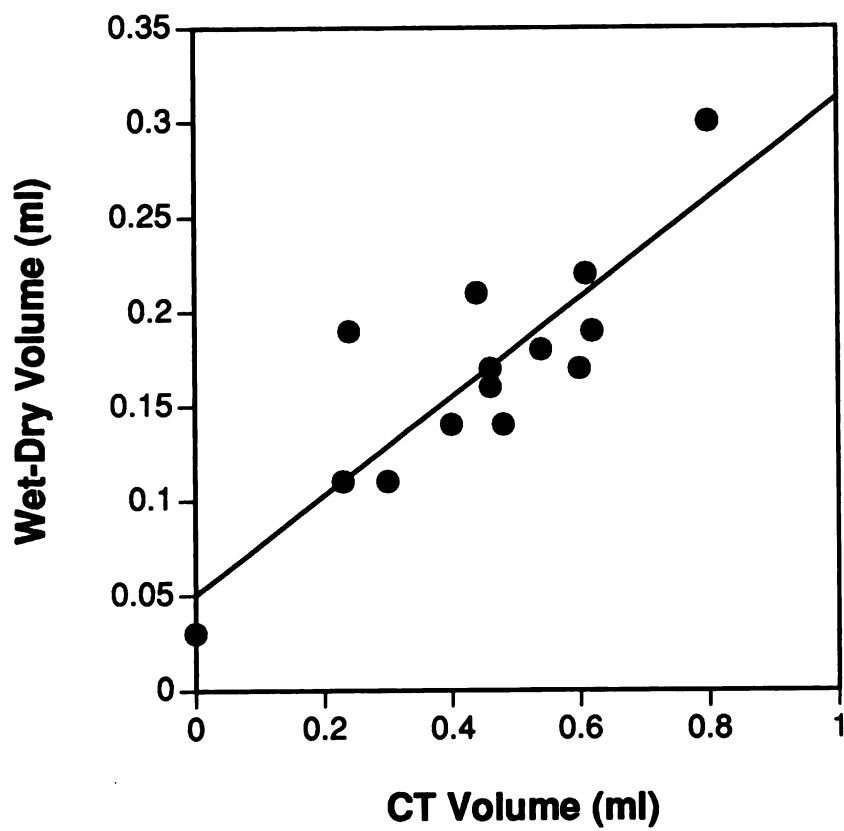
the CT-calculated volumes do not strictly reflect increased water content, as is the case for the wet-dry weight method. Nevertheless, the significant correlation between the CT and wet-dry methods suggests that changes in CT-based volume of edema measured here were largely due to changes in tissue water rather than protein and/or lipid. For this reason, the CT methodology is a valid method of quantifying volume of excess tissue water resulting from focal brain irradiation.

Blood-to-Brain and Brain-to-Blood Transfer Constants

The accuracy of Equation 2 is dependent upon $\Delta CT_{ART}(T)/(1-Hct)$ being directly proportional to $C_P(T)$, the plasma concentration of the contrast agent, and $\Delta CT_{ROI}(T)$ being directly proportional to $C_{ROI}(T)$, the concentration of contrast within the ROI (see Equation III.9). Theoretically, the constant of proportionality, c, should be the same in both cases so that Equation 2 should be valid. However, CT number of small structures, such as arteries, are subject to inaccuracies due to volume averaging,[99] which could alter the proportionality constant relating $\Delta CT_{ART}(T)/(1-Hct)$ to $C_P(T)$. Because of this, the actual proportionality constant was determined in four dogs. Following general anesthesia, an incision was made near the femoral triangle and 10 cm of Tygon tubing, 1 mm diameter, was inserted into the femoral artery and advanced into the aorta. The skin wound was closed and the arterial line flushed with a solution of heparinized (3 U/ml of heparin) normal saline. During the course of a permeability study, ten 5 ml blood samples were collected from the intra-arterial line. Samples were obtained before the administration of any contrast agent, and after every 2-5 CT scans. A 100 µl aliquot was taken from each sample to determine hematocrit, and the remaining blood was allowed to clot, spun at 2000 rpm for 10 minutes, and the serum removed and frozen until

evaluated for total iodine concentration using an x-ray fluorescence technique.[100]

The proportionality constant, c, was approximated by the slope of the least-square regression lines relating $\Delta CT_{ART}/(1-Hct)$ to C_P in each of the four dogs. In all cases, there was a strong and highly significant correlation between $\Delta CT_{ART}/(1-Hct)$ and C_P with correlation coefficients ranging from 0.96 to 0.98. The average value of c for the four dogs was 0.059 ± 0.008 (mean $\pm$ standard error (SE)). Two SEs above and below this mean should contain the range of c for approximately 95% of the dogs, which is the range of 0.043 to 0.075. Letting c' be the proportionality constant relating $\Delta CT_{ROI}(T)$ to $C_{ROI}(T)$ and c be the proportionality constant relating $\Delta CT_{ART}(T)/(1-Hct)$ to $C_P(T)$, then

$$C_{ROI}(T)/C_p(T) = [\ c'\Delta CT_{ROI}(T)]/[c\Delta CT_{ART}(T)/(1-Hct)] \qquad (8)$$

and, if c=c',

$$C_{ROI}(T)/C_p(T) = [\ \Delta CT_{ROI}(T)]/[\Delta CT_{ART}(T)/(1-Hct)] \qquad (9)$$

(see Equation III.9). Because volume averaging is not expected to significantly affect the value of c', it is assumed to be constant, which is consistent with experimental evidence.[79, 101] If the value of c' is assumed to be approximated by the mean value of c, 0.059, whereas c is able to vary by as much as two SEs about the mean or 0.016, then the true value of c'/c could deviate from unity and could range from 0.059/(0.059+0.016) to 0.059/(0.059-0.016) or 0.79 to 1.37. Thus, measurement of K_i based on Equation 2 could potentially be in error by 21-37%. However, this error range could overestimate the actual error if the value of c' also varied and was correlated with the value of c. In fact, at

least some of the variation in c may be due to study-to-study variability in CT number (i.e. the amount of iodine required on a given scan to produce a given change in CT number) as opposed to study-to-study variability in the amount of volume averaging within the arterial ROI. The study-to-study variability in CT number would be expected to have a similar affect on the variability of both c' and c, which would suggest that c' and c are correlated and that the calculated error range should be considered an upper limit.

To determine the accuracy of the numerical method and computational algorithm used in the determination of K_i, K_b, and V_P, a simulation was carried out in which the expected values of $\Delta CT_{ROI}(t)$ and $\Delta CT_{ART}(t)$ were theoretically calculated based on known input values of K_i, K_b, V_P, and Hct (see Appendix VI. Simulated Change in CT Number Due to Blood-Brain Barrier Breakdown). After generating the expected values of $\Delta CT_{ROI}(t)$ and $\Delta CT_{ART}(t)$ based on these input values, the values of K_i, K_b, and V_P were then calculated using the curve-fitting method detailed in Appendix IV, and these calculated values were compared to the input values. In addition, because the values of $\Delta CT_{ROI}(t)$ and $\Delta CT_{ART}(t)$ are always associated with some degree of random error as discussed above, varying amounts of random noise were added onto the generated values of $\Delta CT_{ROI}(t)$ and $\Delta CT_{ART}(t)$ using a computer-based pseudorandom number generator, and the effect of this noise on the accuracy of the determinations of K_i, K_b, and V_P was also assessed.

Three sets of values of K_i, K_b, and V_P were used in the analysis, and the values corresponded to the high, middle, and low end of the values measured in preliminary studies. Noise levels for each of these sets was set at either 0 (i.e. no noise) or 0.8 CT numbers. The value of 0.8 CT numbers was chosen based on two other values: 1) the SD of approximately 8 CT numbers for a single pixel within a water-filled phantom scanned using the CT scanner

Table 1. *Comparison of measured values of K_i, K_b, and V_P obtained from simulated CT-based studies of blood-brain barrier breakdown with actual values.*

Input Parameter Value[*]	Input Noise (CT #)	Measured:[†]		
		K_i ($ml \cdot 100\ ml^{-1} \cdot min^{-1}$)	K_b ($ml \cdot 100\ ml^{-1} \cdot min^{-1}$)	V_p
High	0	3.06	30.48	10.04
	0.8	2.91±0.91	30.68±9.33	10.28±1.89
Middle	0	2.01	15.07	5.05
	0.8	1.99±0.16	15.67±2.15	4.71±0.99
Low	0	1.00	1.01	2.53
	0.8	1.01±0.14	0.65±0.66	3.04±1.13

[*]   The values of the input parameters correspond to the three sets of values of K_i, K_b, and V_P used for calculation of the simulated ΔCT_{ART} and ΔCT_{ROI} data from which the K_i, K_b, and V_P were measured. The "high" input values of K_i, K_b, and V_P were 3 $ml \cdot 100\ ml^{-1} \cdot min^{-1}$, 30 $ml \cdot 100\ ml^{-1} \cdot min^{-1}$, and 10%, respectively, the "middle" values were 2 $ml \cdot 100\ ml^{-1} \cdot min^{-1}$, 15 $ml \cdot 100\ ml^{-1} \cdot min^{-1}$, and 5% respectively, and the "low" values were 1 $ml \cdot 100\ ml^{-1} \cdot min^{-1}$, 1 $ml \cdot 100\ ml^{-1} \cdot min^{-1}$, and 2.5% respectively.

[†]   Measured values are given as mean ± SD (n=5); no SD is supplied for the cases of 0 noise because there is no variation in the measured values for such cases.

settings used in the CT-based transfer constant measurements, and 2) the size of "typical" ROIs for a focal irradiation lesion within dog brain of 25 mm^2 (100 pixels) (see Equation 7).

The results shown in Table 1 in the cases of 0 noise demonstrate that derived values of K_i, K_b, and V_P generally agree with the input values with an error of ±1%. This suggests that the numerical method and accompanying computer algorithm used are accurate methods of determining the parameters of interest when there is no noise in the data. In the presence of noise, the standard deviations (SD) of the measured parameters demonstrate that there can be considerable error in a single measurement of K_i, K_b, and V_P, but the mean values obtained from repeated measurements (n=5) of the parameters were generally within ±10% of the known values of the parameters.

Cerebral Blood Flow

The validity of the CT method was evaluated by comparing it to an accepted method of blood flow measurement, the radioactive microspheres method. The feasibility, reproducibility, and accuracy of this technique of rCBF measurement were determined in a series of studies in beagle dogs under normal physiologic, altered physiologic, and pathophysiologic conditions.

Twenty-five dogs (16 male, 9 female) were assigned to three experimental study groups; some of the dogs were assigned to more than one study group. Two of the dogs received brain irradiation before entering Study 3.

Study 1, which included 12 normal dogs, was designed to test the feasibility of using ultrafast CT to measure rCBF. Regional CBF was measured as detailed above in the left and right internal capsule, neocortex, basal ganglia, and whole hemisphere (Figure 4), and the results from the various regions were compared. During scanning, dogs were ventilated mechanically,

using a tidal volume of 200 ml and a respiratory rate of 25 breaths per minute. To determine arterial carbon dioxide tension (p_aCO_2), 1 ml blood samples were collected from the femoral artery immediately after the last scan of the ultrafast CT procedure. To reduce variability in rCBF resulting from alterations in p_aCO_2, only those studies in which p_aCO_2 was 35-40 mm Hg were compared.

Study 2, which included 12 normal dogs, investigated the reproducibility of the ultrafast CT technique. For each dog, two rCBF measurements were made 10 minutes apart and the resulting rCBF values were compared. No mechanical ventilation was used and arterial blood samples were collected for the p_aCO_2 determination immediately after the last scan of each ultrafast CT procedure. In addition, to establish inter-observer reproducibility, 12 of the examinations were arbitrarily selected, and the rCBF values within the left and right hemispheric ROIs were determined independently by two observers. To derive the intra-observer reproducibility, five of these studies were evaluated twice, 1-2 weeks apart, by a single observer. Reproducibility was defined as the SD of the difference in two measurements expressed as a percent of the mean of the two measurements.[56]

Study 3 was used to validate the ultrafast CT technique against the radiolabeled microsphere method in both normal and abnormal brain. Three normal dogs, one dog with a focal radiation lesion caused by an ^{125}I brain implant[52] and one dog that had previously received a single radiation dose of 15 Gy to the right hemisphere[102] were included. Both of the radiation treatments produce significant and well-characterized increases in BBB permeability. Up to five simultaneous ultrafast CT/microsphere studies were done in each dog with an interval of 10-15 minutes between studies. To alter p_aCO_2, dogs were ventilated mechanically using a tidal volume of 200 ml and respiratory rates of either 10, 25, or 50 breaths per minute. Arterial blood

samples were collected for p_aCO_2 determination after each ultrafast CT/microsphere study.

For the microsphere studies, a 14 g pig-tail catheter was placed in the femoral artery and advanced to the left ventricle. Arterial pressure at the catheter tip was monitored to confirm proper placement. A second 14 g catheter was placed in a brachial artery. Between 1.5 and 2.0 x 10^6 microspheres, 15 μm in diameter, radiolabeled with ^{153}Gd, ^{57}Co, ^{85}Sr, ^{95}Nb, ^{54}Mn, or ^{65}Zn were injected into the left ventricle beginning with the start of administration of the iodinated contrast agent. A reference blood sample was withdrawn from the brachial artery at a rate of 7.5-8.0 ml/minute for 15 seconds before and for 55 seconds after microsphere injection.

After the last study, the skull was marked at the level of the CT scan plane, and the dog was euthanized with an overdose of pentobarbital. The left ventricle of the heart was opened to confirm proper catheter placement. The brain was removed, sectioned at the level of the scan plane, and fixed in formalin. Sections of the brain corresponding to the internal capsule, neocortex, and basal ganglia were dissected and weighed. Additional samples of the left and right frontal lobes were taken to verify adequate mixing of the microspheres and uniform distribution to the two sides of the brain. The activity of each isotope within each section was determined as described elsewhere.[103]

The errors in the gamma-variate curve fits used for CT-based blood flow determinations were calculated for Study 1 according to the formula

$$[\sum_{1}^{n'}(M_i-C_i)^2/(n'-1)]^{1/2} \cdot [n'/\sum_{1}^{n'}M_i] \tag{10}$$

in which M_i and C_i are the measured and computed values at time i, and n' is the number of fitted data points.

For the microsphere technique, blood flow was calculated using the relationship

$$Q_{ROI} = (Counts_{ROI}/Counts_{Ref}) \cdot Q_{Ref}, \tag{11}$$

in which Q_{ROI} is the blood flow (ml·min⁻¹) in the ROI and Q_{Ref} is the blood flow (ml·min⁻¹) in the reference arterial blood sample.[103] $Counts_{ROI}$ and $Counts_{Ref}$ are the radioactivity of the same samples, respectively.

Simple linear regression analysis was used to evaluate correlations between repeated measures of blood flow within the same region and between the ultrafast CT and the microsphere measurements of rCBF. Absolute differences were evaluated using a paired, two-tailed Student's t-test. The level of significance was assigned at the 0.05 level. Regional differences in CBF (neocortex *versus* basal ganglia, neocortex *versus* internal capsule, and basal ganglia *versus* internal capsule) were evaluated using a one-factor analysis of variance (ANOVA) followed by the Scheffe F-test, which corrects for multiple comparisons.[104] Because blood flow was measured up to five times for each ROI in each dog in the combined ultrafast CT/microsphere studies, combining all the individual ultrafast CT/microsphere values from all dogs did not constitute a perfectly random sample. Therefore, the five values obtained from each normal dog and from the unirradiated regions from each of the irradiated dogs were averaged for each ROI, and those mean values were used in the regression analyses and paired t-tests comparing the microsphere and ultrafast CT results.

The average time required to perform two ultrafast CT studies, including the time required for positioning and set-up of ancillary equipment, was approximately 30 minutes. The procedures used, including mechanical ventilation and in many cases repeated bolus injections, were well tolerated by all animals.

The best fits of the curve-fitting routine were for the data from the arterial, hemispheric, and neocortical ROIs. The average errors in the curve fits for those respective regions were small and were 0.055 ± 0.018, 0.065 ± 0.011, and 0.076 ± 0.018 (mean $\pm$ SD). In comparison, the errors for the basal ganglia and internal capsule were 0.137 ± 0.058 and 0.187 ± 0.085, respectively.

The lowest rCBF values measured in Study 1 were those within the internal capsule, a white matter region. For gray matter regions, the basal ganglia showed intermediate values, and the highest values were in the neocortex (Table 2). Significant regional differences in CBF were detected in all cases (basal ganglia *versus* neocortex as well as basal ganglia or neocortex *versus* internal capsule), and the variation in side-to-side differences in rCBF was small relative to the inter-animal variation (Table 2).

Study 2 showed that there was a significant positive correlation between two rCBF measurements obtained 10 minutes apart for the hemisphere ($r= 0.87$), basal ganglia ($r = 0.77$), internal capsule ($r= 0.85$), and neocortex ($r = 0.78$). There was a slight but insignificant increase in p_aCO_2 between the first and second study (3.2 ± 9.1 mm Hg, mean increase $\pm$ SD), which was accompanied by insignificant reductions in rCBF (Table 3). The inter-observer and intra-observer reproducibility in calculated rCBF were 10.2 and 9.9%, respectively.

In the ultrafast CT/microsphere study (Study 3), p_aCO_2 varied over a wide range (20.7-62.3 mm Hg) resulting in a ten-fold change in rCBF as determined

Table 2.   *Regional and side-to-side variation in CBF measured by ultrafast*

CT

Region	Left Brain	Right Brain	Left-Right Difference
Hemisphere	75.6 ± 29.4	76.1 ± 34.1	-0.5 ± 12.3
Basal Ganglia	68.4 ± 28.2	62.9 ± 26.9	-1.8 ± 14.5
Internal Capsule	41.2 ± 15.0	43.2 ± 16.4	-2.0 ± 9.4
Neocortex	80.8 ± 37.2	82.6 ± 34.2	5.5 ± 17.2

CBF, cerebral blood flow. Values are given in ml·100 g^{-1}·min^{-1} (mean ± SD; n=12).

Table 3.   *Comparison of percent differences* in ultrafast CT measured rCBF values obtained 10 minutes apart with left-right differences

Region	10 Minute % Difference	Left-Right % Difference
Hemisphere	14.0 + 27.0	18.2 ± 17.3
Basal Ganglia	22.2 ± 28.5	1.3 ± 13.0
Internal Capsule	16.8 ± 26.9	-9.4 ± 21.5
Neocortex	12.6 ± 33.6	5.2 ± 9.6

rCBF, regional cerebral blood flow. Values are given in ml·100 g^{-1}·min^{-1} (mean ± SD; n=12).

* Percent difference (mean ± SD) in two values is defined as (Value 1- Value 2)/(Average of Values 1 and 2)·100%, in which Value 1 is the measurement from the first of the two studies separated by 10 minutes or is the left rCBF measurement. Left and right ROIs were averaged for the computation of regional percent differences for rCBF values obtained 10 minutes apart, and the two values from the 10 minute studies were averaged for computation of left-right differences.

by the microsphere technique. A comparison of all of the ultrafast CT rCBF values with those determined using the microsphere technique revealed good agreement between the two methods for both normal and irradiated tissues (Figures 8 and 9). In the normal animals, simultaneous measurements of rCBF by the microsphere and ultrafast CT methods showed a significant correlation between averaged ultrafast CT and microsphere rCBF values for the hemisphere (r = 0.95), the basal ganglia (r= 0.95), and the neocortex (r = 0.94), but not for the internal capsule (r = 0.51). There were no significant differences between the rCBF values obtained using the microsphere method and those obtained with ultrafast CT for any region considered ($p > 0.10$). Both methods typically demonstrated differences of less than 20% between homologous ROIs on contralateral sides of the brain. In the focally irradiated dog, rCBF in the irradiated region was reduced relative to that in a homologous contralateral region by 76.4 ± 7.9% (mean ± SE for the four measurements of rCBF made using the microsphere technique and 70.7 ± 4.7% (mean ± SE) for the four measurements made using the ultrafast CT technique. These values were much greater than the left-right differences in the normal dogs (Tables 2 and 3). In contrast, left-right differences for the dog that had undergone hemibrain irradiation were 10.4 ± 3.2% for the hemisphere, 2.3 ± 12.5% for the basal ganglia, 32.3 ± 11.1% for the internal capsule, and 5.9 ± 9.6% for the neocortex (mean ± SE) when determined by the microsphere method, and 8.6 ± 10.1%, -4.5 ± 17.2%, -6.9 ± 41.3, and 9.2 ± 10.9%, respectively, when determined by the ultrafast CT method.

Regression analysis of rCBF response to alterations of p_aCO_2 showed that, for both the microsphere and ultrafast CT techniques, there were significant positive correlations between rCBF and p_aCO_2 for all brain regions considered (Table 4). The response of rCBF within the basal ganglia to p_aCO_2 alteration

Figure 8   Ultrafast CT versus microsphere measurements of regional cerebral blood flow (rCBF, ml·100 g⁻¹·min⁻¹)) for normal hemisphere, basal ganglia, internal capsule, and neocortex (top), and for a focal radiation lesion and various regions within an irradiated hemisphere (15 Gy, single dose) (bottom). There was a significant ($p<0.05$) correlation between the averaged ultrafast CT and microsphere rCBF measurements for the normal hemisphere (r=0.95), the basal ganglia (r=0.95), and the neocortex (r=0.94), but not for the internal capsule (r=0.51). In no case was the slope of the regression line significantly different from the line of unity, which is shown for comparison.

Figure with two scatter plots. Top plot: Ultrafast CT rCBF (y-axis, 0–180) versus Microsphere rCBF (x-axis, 0–180).

Legend (top plot):
- ✗ Hemisphere
- □ Basal Ganglia
- ▲ Internal Capsule
- ○ Neocortex
- ▣ Focal Lesion
- ■ Contra. to Lesion
- ● Irrad. Hemisphere
- ■ Irrad. Basal Ganglia
- ▲ Irrad. Internal Capsule
- ● Irrad. Neocortex

Bottom plot: Ultrafast CT rCBF (y-axis, 0–180) versus Microsphere rCBF (x-axis, 0–180).

Legend (bottom plot):
- ● Focal Lesion
- ✗ Irrad. Hemisphere
- □ Irrad. Basal Ganglia
- ▲ Irrad. Internal Capsule
- ○ Irrad. Neocortex

Figure 9   Regional cerebral blood flow measurements (mean ± SE in ml·100 g⁻¹·min⁻¹) within a homologous region contralateral to a focal radiation lesion (left) and within a focal lesion itself (right) as determined by both the microsphere and ultrafast CT methods. Both methods demonstrate a marked reduction in blood flow within the focal radiation lesion relative to the homologous contralateral region.
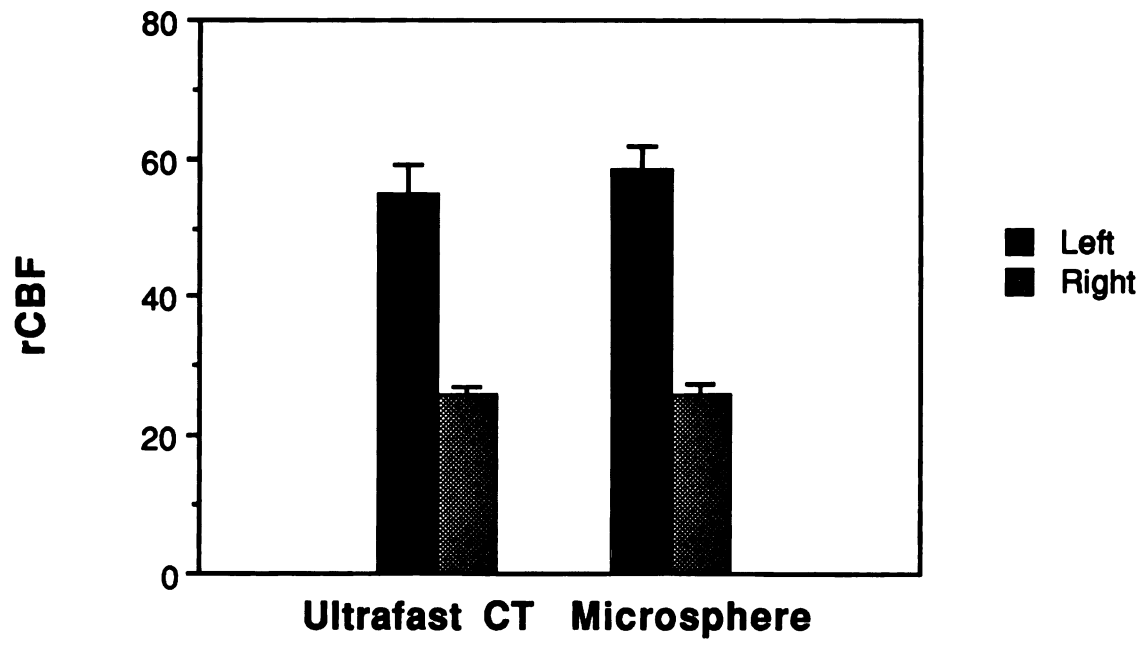
Table 4.   *Responsiveness of rCBF to alterations in p_aCO_2 determined Using ultrafast CT and the radioactive microsphere technique.*

Region	Average CBF Response to Alterations of CO_2	
	Ultrafast CT	Microsphere
Hemisphere	1.12 ± 0.32†	1.66 ± 0.22†
Neocortex	1.34 ± 0.36*	2.04 ± 0.26†
Basal Ganglia	0.80 ± 0.28*	1.77 ± 0.28†
Internal Capsule	0.51 ± 0.17†	0.90 ± 0.13†

p_aCO_2, arterial carbon dioxide tension. rCBF, regional cerebral blood flow. Values are given in ml·100 g^{-1}·min^{-1}·mm Hg^{-1}. The numbers in the table correspond to the average of the slopes ($\pm$ SE) of the regression lines from the regression analysis comparing measured ROI blood flow (left and right side averaged) versus p_aCO_2 in the three normal dogs used in the ultrafast CT/microsphere study. The p values correspond to the probability that the slopes differ from zero and that there is significant alteration in rCBF associated with alteration in p_aCO_2.

* $p < 0.05$

† $p < 0.01$

determined by the microsphere technique was significantly greater than the response determined by the ultrafast CT technique ($p<0.05$), and the rCBF response within the internal capsule determined by the microsphere technique approached being significantly greater ($p<0.10$). However, the trends of the regional responses determined by the two techniques were similar, the neocortex showing the greatest responsiveness, the internal capsule the least, and the basal ganglia an intermediate level (Table 4).

The significant correlation between the two methods of measuring rCBF demonstrated that CT is a valid method of quantifying rCBF under a variety of conditions. However, although there was good overall agreement of the results obtained with ultrafast CT and the microsphere method over a wide range of rCBF values (Figure 8), there were instances in which the two techniques appeared to differ. In the case of the left-right differences in the blood flow to the internal capsule of the dog that had undergone hemibrain irradiation, the microsphere method detected a greater difference than detected by the ultrafast CT method. In addition, rCBF seemed to be somewhat less responsive to alterations in p_aCO_2 when measured by the ultrafast CT method. However, studies of rCBF response to p_aCO_2 using the microsphere method have shown a tendency to report values of rCBF responsiveness that are 1.5-2.0 times higher than those determined using other methods of rCBF estimation, such as hydrogen and xenon clearance.[56] Lastly, measurements within the internal capsule showed an insignificant correlation between the ultrafast CT and microsphere values. This result may have been due to the low range of flow values within the internal capsule relative to the uncertainty of rCBF values obtained using these two methods, rather than to an actual disagreement between the two methods. Furthermore, some of the differences between the two methods used here could probably be attributed to an unavoidable margin

for error in sampling exactly the same tissues with the two techniques and to some imprecision in the measurement of rCBF using the microsphere method.[105]

Improper fitting of the ultrafast CT data by the gamma-variate fitting algorithm might have also contributed to differences between the two methods in measurement of rCBF. When the data were noisy or there was only a slight rise in the CT number within the ROI, the algorithm was more likely to incorrectly pick the "proper" initial point for curve fitting, and this was evident from the data deviating substantially from the fitted curves. In addition, there were instances where a single point differed markedly from the surrounding points and drastically altered the fit. The gamma-variate fit algorithm may have contributed to the poor fits by logarithmically transforming the data; by doing so, the algorithm actually minimized the deviations between the logarithmic transformation of the fitted function and the logarithmic transformation of the data rather than the absolute deviations between the fitted function and the data. Substantial deviations between the data and the fitted function would appear to be less substantial following logarithmic transformation, and this could and apparently did in some cases lead to poor fits. A way to avoid such problems would be to use a non-linear least-squares method of fitting the gamma-variate function to the data, such as the Marquardt method,[106] which can be used to minimize the true (rather than the logarithmic) deviations between the fitted function and the data. In the present study, because the Marquardt method was not implemented within the ultrafast CT scanner software, it was found that the most expedient method of improving a fit was to exclude data points which appeared to substantially differ from the surrounding data points. However, because of the observer bias that this could potentially introduce, a more objective method of non-linear curve-fitting would be

preferable. Preliminary results suggest that the correlation between the two methods of rCBF measurement are likely to improve when the Marquardt method of curve-fitting is fully implemented.

The most apparent deviations between the microsphere and ultrafast CT rCBF values arose at flow values greater than 120 ml·100 g^{-1}·min^{-1} (Figure 8). Because blood flow is proportional to the inverse of the mean transit time (Equation 3), it was evident that underestimation of the very short mean transit times which accompany high blood flow could result in significant overestimation of blood flow as mentioned in the theoretical analysis of the method. In the case of radiation injury, measurement of low rCBF was considered to be generally of greater concern. Nonetheless, to avoid the overestimation of rCBF, a minimal acceptable mean transit time could be established for blood flow calculations. In our study, all blood flow values of greater than 120 ml·100 g^{-1}·min^{-1} had corresponding mean transit times in the range of 0.8-0.9 seconds, which was more than two SDs below the average mean transit time for all regions combined. Based on this, one second might be set as a reasonable minimal acceptable mean transit time, and rCBF values corresponding to mean transit times shorter than this could be handled differently, such as by recalculating the rCBF with the mean transit time set equal to one.

The SD of percent differences of ultrafast CT studies done 10 minutes apart (Table 3) indicates that short-term reproducibility in our study was approximately 30%. This value is poorer than the 10-15% reproducibility obtained with invasive methods such as the microsphere technique.[56, 105] However, based on our 10% inter-observer and intra-observer reproducibility, about one-third of the short-term reproducibility was accounted for by differences in how the ROIs were drawn for evaluation of each of the two

studies. The poorer reproducibility could also have been related to hemodynamic alterations, such as arterial vasodilatation,[107-109] induced by hyperosmotic contrast agents. However, such effects generally do not appear until 3-4 seconds after exposure of arteries to the contrast, so it seemed unlikely that the time-concentration data used for ultrafast CT flow calculations would be significantly affected by these agents. Consequently, it was felt that a single flow study would be valid, but the contrast agent might modify the blood flow in such a way that subsequent measurements would be altered relative to the first measurement.[109]

Another potential source for the poorer reproducibility of ultrafast CT was the use of a single value for n in Equation V.13. The parameters that comprise n and that might have changed between subsequent studies were m and HCT_{PA}. The factor m could have been altered due to changes in the arrival time of the bolus at the peripheral artery used for computation of rCBF relative to the actual arrival time of the bolus at the ROI (see Equation V.12 and related discussion). HCT_{PA} could change due to changes in cardiac output resulting in differing amounts of dilution of the hematocrit by the contrast agent. However, when changes in m and HCT_{PA} were accounted for on a study-by-study and region-by-region basis, there was no appreciable change in the reproducibility, suggesting that the use of a single value for n was warranted.

An important finding was that there was good agreement between the microsphere and CT methods despite the presence of radiation-induced BBB disruption. This supported the theoretical argument (Appendix V) suggesting that BBB disruption should not significantly alter dynamic CT-based rCBF measurements. It also indicated that the method would be valid for the study of changes in rCBF following focal irradiation.

Lastly, in agreement with others,[110] the data suggested that left-right differences in rCBF in normal brain tended to be small. For example, whereas the reproducibility data suggested that sequential measurements of rCBF might normally differ by as much as ±30%, left-right differences were consistently in the range of ±10-20%. It was evident that this characteristic of rCBF could be particularly helpful in evaluating pathologic changes in rCBF confined to one hemisphere, such as a focal radiation lesion. For this reason, sequential studies of rCBF following irradiation were analyzed for both absolute and relative (i.e. left *versus* right) changes in blood flow.

Because of the desire to use the best method possible for rCBF evaluation following irradiation, the ultrafast CT method was compared to the xenon CT method, which is an accepted and available method of non-invasive, CT-based rCBF measurement.[83] Six male and 6 female purebred adult beagle dogs were used for the comparison. Cerebral blood flow was measured in selected regions in both hemispheres of each dog using xenon CT and ultrafast CT. The regions examined included the left and right neocortex, basal ganglia, internal capsule, and whole hemisphere (Figure 4). Xenon CT studies preceded the ultrafast CT studies in all but one dog, and at least 48 hours elapsed between the two examinations.

Ultrafast CT studies were carried out as described above. For the xenon flow measurements, a GE 9800 CT scanner outfitted with a GE Xenon Blood Flow Imaging System (General Electric Medical Systems, Milwaukee, Wisconsin) was used. Dogs were placed in sternal recumbency with the head extended onto a plastic head rest within the CT scanner. Initial xenon studies were conducted in a manner similar to that used clinically, with the dogs respiring spontaneously. However, the resultant expired xenon concentration data, which were used to derive the arterial input function of xenon, [83] were so

variable that the data could not be used (Figure 10). To stabilize xenon uptake, all subsequent studies were carried out using a mechanical respirator. The endotracheal tube was connected to a Harvard Respirator set at 200 ml tidal volume and 16 breaths per minute. The xenon administration tank was then connected to the inflow valve of the respirator. Expired xenon concentration was monitored by the system and used to calculate the arterial input function as detailed elsewhere.[111] The xenon gas mixture was nominally 31% xenon, 0.6-0.8% CO_2, and the balance O_2; the CO_2 in the mixture was designed to stabilize respiration and thus optimize the calculation of the arterial input function. A venous blood sample was obtained for hematocrit determination as required by the GE Xenon System.

A lateral computed radiograph was taken of the skull and transverse CT scans of the brain were obtained for localization of the desired scan plane. A scan level comparable to that used in the ultrafast CT/microsphere studies was chosen for the xenon CT study. Two baseline scans were obtained prior to the inhalation of xenon, and six scans were obtained over a 6 minute period after the start of xenon inhalation. Scanning parameters were 80 kVp and 200 mA with a 4 sec scan time; scan thickness was 5 mm. Images were reconstructed on a 256 X 256 matrix with a pixel size of 0.488 mm.

Following the xenon flow study, the system software smoothed all the images to reduce pixel noise, averaged the two baseline CT scans, and subtracted the resulting pixel density from each of the post-xenon inhalation scans on a pixel-by-pixel basis to determine the xenon enhancement as a function of time. By combining the pixel enhancement data with the end-tidal xenon concentration data, rCBF values were derived for each CT image pixel according to methods previously described in detail.[83] A functional perfusion image of the brain, in which the gray scale represented the rCBF values within

Figure 10   Xenon uptake curves (xenon concentration in expired air vs. time after start of xenon inspiration) obtained during spontaneous respiration (A, top) and during forced ventilation (B, bottom) demonstrating the irregularity of such curves when obtained during spontaneous respiration.

A

XENON UPTAKE CURVE

% XENON vs TIME (MINUTES)
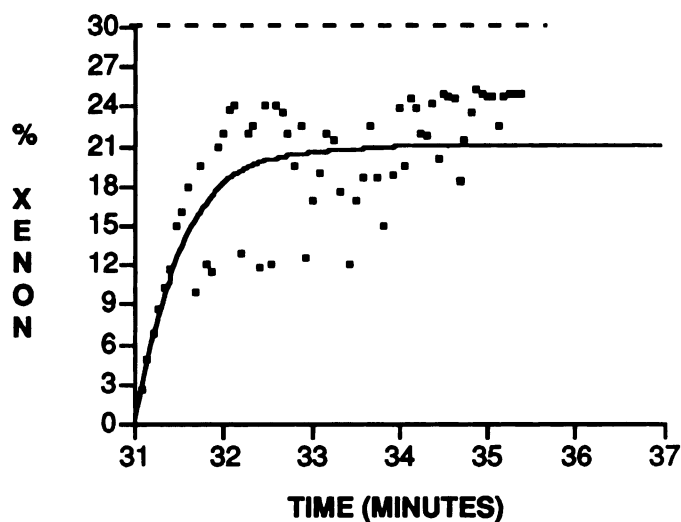
- – – – – ▪ % XENON IN STORAGE BAG
- —————— ▪ XENON UPTAKE CURVE
- • • • • • • ▪ INDIVIDUAL XENON SAMPLE POINTS

B

XENON UPTAKE CURVE

% XENON vs TIME (MINUTES)
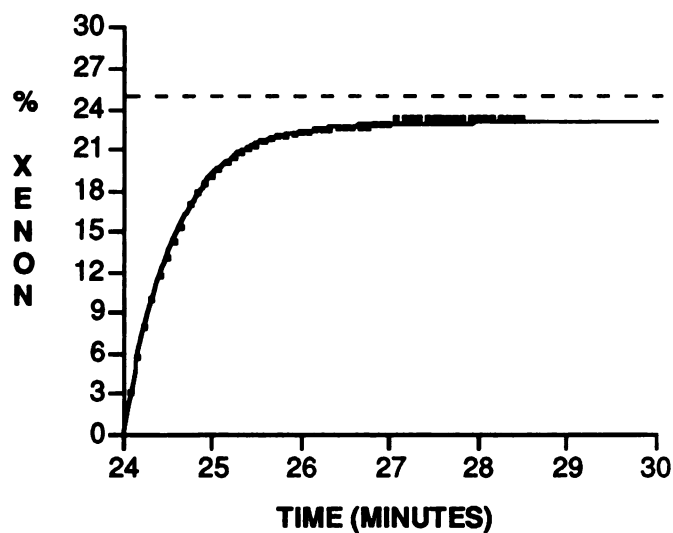
- – – – – ▪ % XENON IN STORAGE BAG
- —————— ▪ XENON UPTAKE CURVE
- • • • • • • ▪ INDIVIDUAL XENON SAMPLE POINTS

each voxel, was generated from these data. Original scans and computed xenon images were converted to a standard file format and transferred to a specially-programmed off-line computer system for analysis.

Irregular ROIs, corresponding to the left and right neocortex, basal ganglia, internal capsule, and hemisphere, were drawn using a manually-directed, trackball-guided cursor on the CT scan obtained at the peak of xenon enhancement. Each ROI was then mapped on the corresponding location on the functional perfusion image, and the average rCBF was recorded. The same ROIs were also used in the ultrafast CT studies (Figure 4), and rCBF for these studies was computed as described above.

The rCBF within each ROI examined, including left and right hemisphere, neocortex, basal ganglia, and internal capsule was compared to the rCBF within every other ROI. Separate comparisons were carried out for the two methods of rCBF determination. Differences in rCBF were evaluated for significance using a single factor, repeated measures ANOVA (see Appendix X. Analysis of Variance - Description and Rationale) followed by a Scheffe F-test, which corrects for multiple comparisons.[104] Differences in variances were evaluated using a two-tailed variance ratio test using the F distribution. Side-to-side correlations for the various ROIs considered were analyzed using simple linear regression analysis. Significance was assigned at the 0.05 level.

The use of mechanical ventilation resulted in appreciably less variability in the uptake of xenon (Figure 10). Only data from studies carried out with the mechanical respirator are included here.

The areas (mean ± SE) of the ROIs used in data analysis of the xenon CT studies were 4.72 ± 0.12 cm^2 for the hemisphere, 1.51 ± 0.31 cm^2 for the neocortex, 0.60 ± 0.02 cm^2 for the basal ganglia, and 0.66 ± 0.02 cm^2 for the internal capsule. In the data analysis of the ultrafast CT studies, the areas were

3.78 ± 0.15, 2.05 ± .10, 0.59 ± 0.02, and 0.67 ± 0.02 cm^2 for the same respective regions.

The ranges of blood flow in the hemisphere, neocortex, basal ganglia, and internal capsule were 41-71, 46-80, 38-87, and 22-73 ml·100 ml^{-1}·min^{-1}, respectively, when measured by the xenon CT technique, and 35-177, 41-219, 34-210, and 16-107 ml·100 ml^{-1}·min^{-1} when measured by the ultrafast CT technique. The variances of the rCBF values determined using ultrafast CT were significantly greater than those determined using xenon CT for all regions evaluated. Ultrafast CT detected significantly lower rCBF within the left and right internal capsule relative to the left and right hemisphere. In addition, ultrafast CT detected significantly lower blood flow in the white matter region of the internal capsule relative to the gray matter regions of the neocortex and basal ganglia in all cases (Figure 11). In contrast, when rCBF was measured using xenon CT, rCBF was significantly lower in the left or right internal capsule relative to the other regions only in some cases; blood flow in white matter regions was not consistently lower than that within the hemispheres and within gray matter regions (no significant difference for left internal capsule *versus* left hemisphere, left internal capsule *versus* right hemisphere, and left internal capsule *versus* right neocortex). Neither technique detected significant differences in blood flow between the neocortex and basal ganglia or between homologous regions on opposite sides of the brain.

When rCBF was measured using ultrafast CT, there was a highly significant side-to-side correlation for all regions considered, including the hemisphere (r = 0.97), the neocortex (r =.97), the basal ganglia (r =.98), and the internal capsule (r = 0.88) (Figures 12 and 13). In contrast, only the side-to-side correlation for the basal ganglia approached significance (r = 0.53, *p* < 0.10) when rCBF was measured using xenon CT (Figures 12 and 13).

Figure 11   Absolute rCBF (mean ± SE in ml·100 ml^{-1}·min^{-1}) within the left (black) and right (gray) hemisphere (Hemi), neocortex (NC), basal ganglia (BG), and internal capsule (IC) determined using both the xenon CT and ultrafast CT technique. Although there is greater variance in the rCBF values determined using ultrafast CT, both methods detected significantly lower rCBF within the white matter region of the internal capsule relative to the gray matter regions of the neocortex and basal ganglia. The hemisphere was not included in the analysis of regional differences in rCBF and is included for comparison purposes only.

Xenon CT
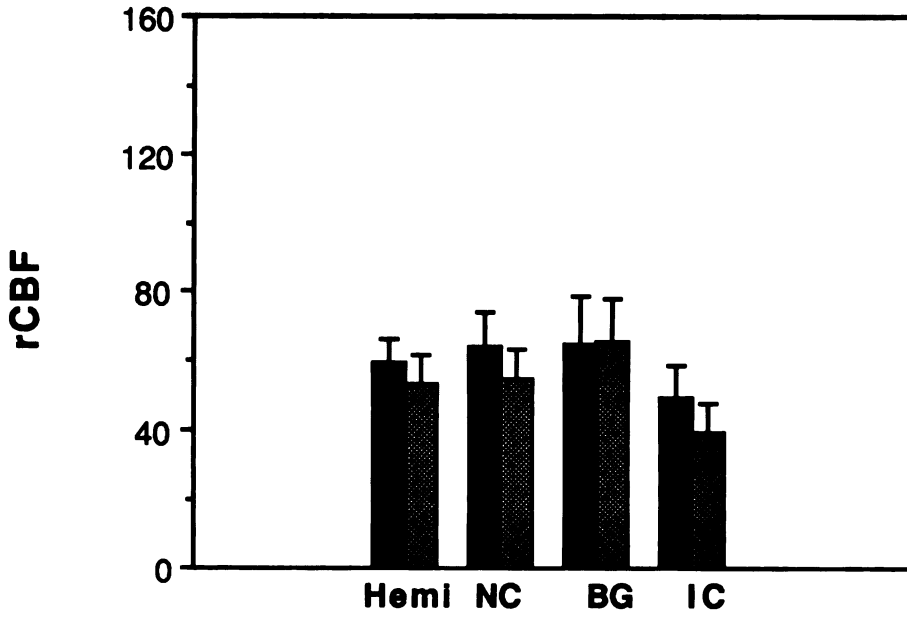
Ultrafast CT
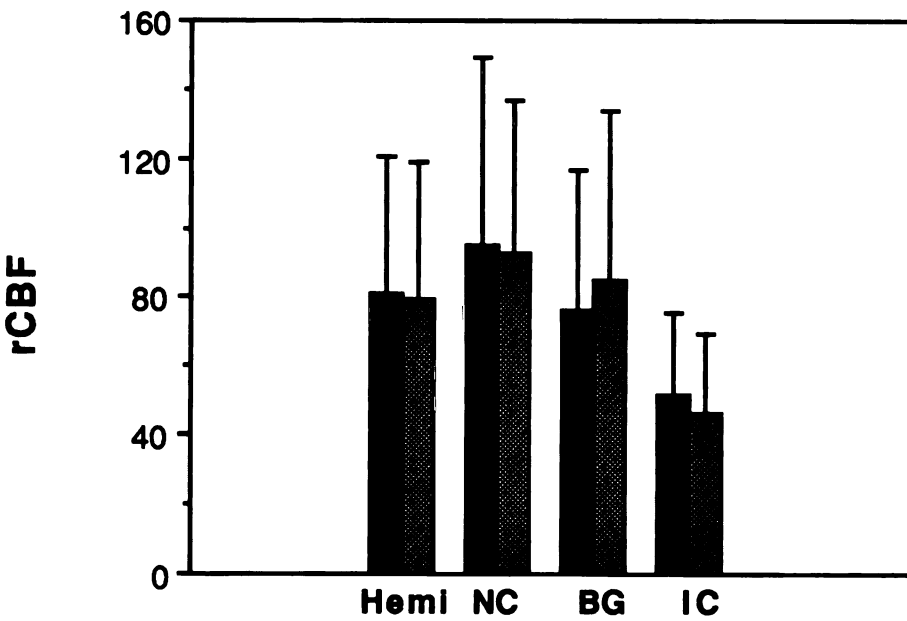
Figure 12   Comparison of left and right-sided rCBF (ml·100 ml^{-1}·min^{-1}) for the hemisphere (top, circles) and the basal ganglia (bottom, squares) demonstrating the strong side-to-side correlation present in rCBF when determined using ultrafast CT (closed symbols) but not when determined using xenon CT (open symbols).   The line of unity is drawn on each graph for comparison.

Ultrafast CT

Xenon CT
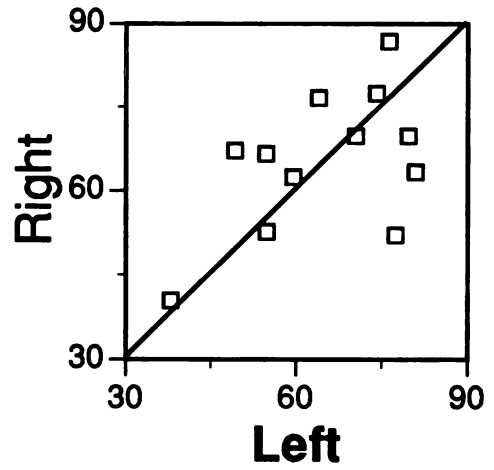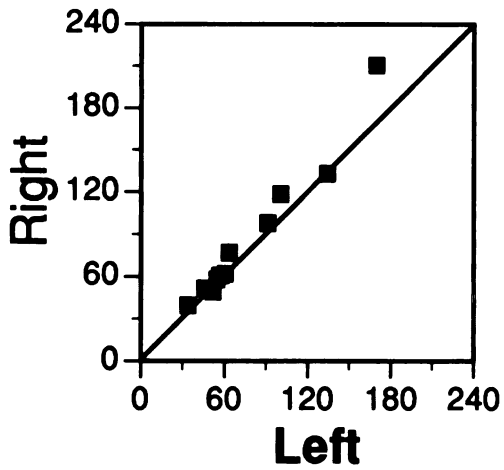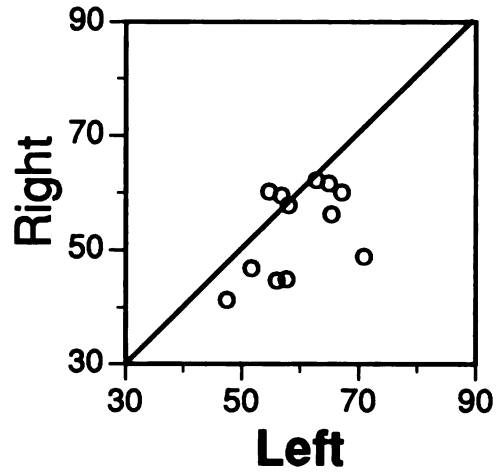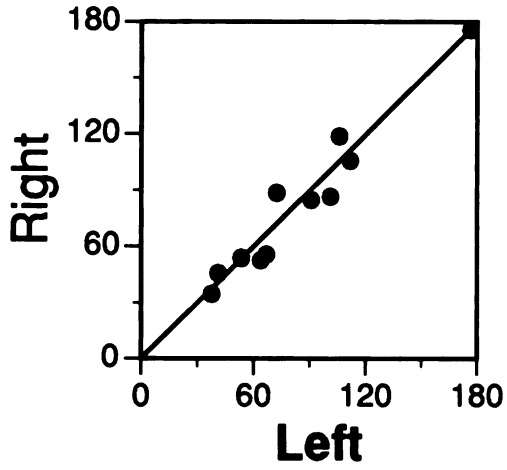
Figure 13   Comparison of left and right-sided rCBF (ml·100 ml⁻¹·min⁻¹) for the neocortex (top, circles) and the internal capsule (bottom, squares) demonstrating the strong side-to-side correlation present in rCBF when determined using ultrafast CT (closed symbols) but not when determined using xenon CT (open symbols).   The line of unity is drawn on each graph for comparison.

Ultrafast CT

Xenon CT
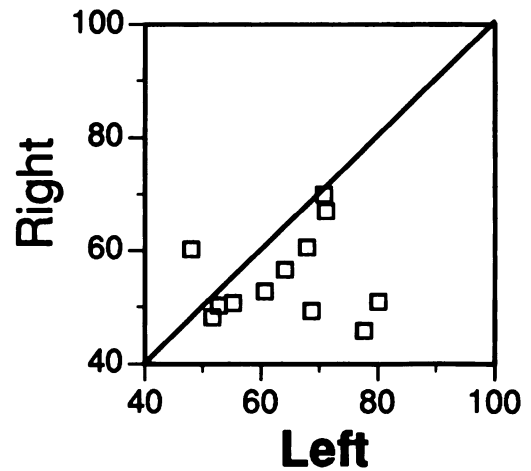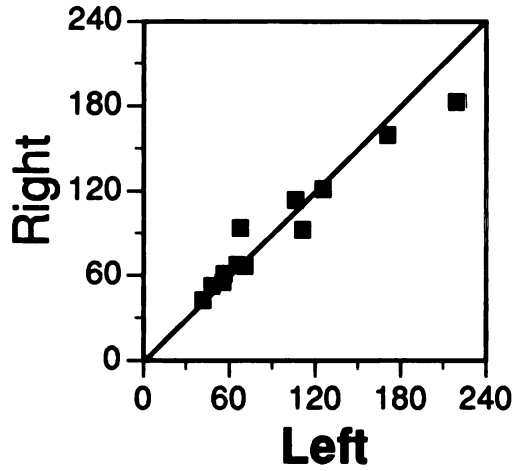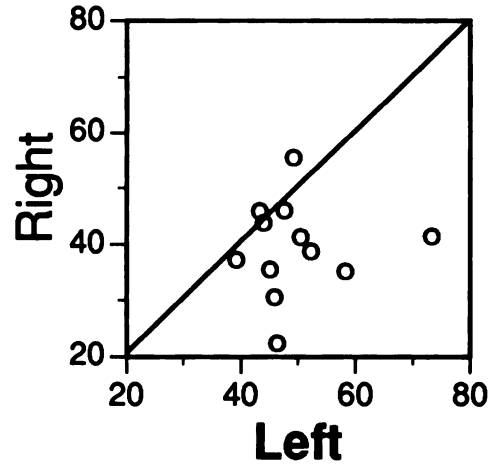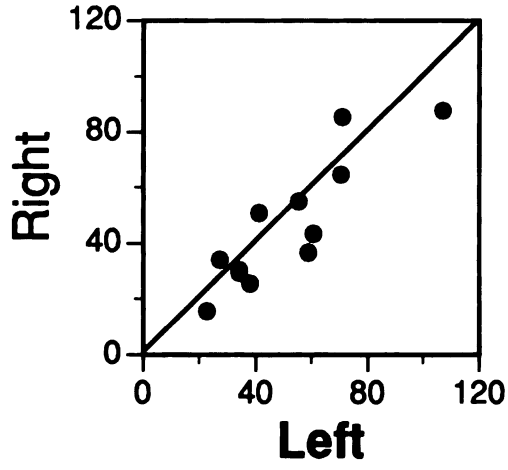
Invasive measurements of rCBF within normal white and gray matter regions of normal brain have repeatedly demonstrated that blood flow within the white matter regions is typically 1/4 to 1/2 that of gray matter.[56] A non-invasive method of rCBF measurement with a sensitivity comparable to invasive methods should therefore consistently detect differences in blood flow between white and gray matter. While xenon CT was able to detect regional differences in blood flow between white and gray matter in many cases, it did not detect such differences consistently. There were no significant differences between rCBF in the left internal capsule and the right neocortex. The rCBF within the internal capsule should also be less than that within the hemisphere, which is a mixture of both gray and white matter, but xenon CT did not detect lower flow in the left internal capsule relative to either left or right hemisphere. Ultrafast CT, on the other hand, detected significantly lower flow in the left and right internal capsule relative to pure gray matter regions and relative to left or right hemisphere in all cases. Based on these findings, ultrafast CT appeared to be more sensitive than xenon CT to regional differences in rCBF.

The xenon CT studies were restricted to a minimum scan thickness of 5 mm, and the most comparable scan thickness available, 6 mm, was selected for the ultrafast CT study. Because the scan thicknesses used for the two methods differed, the volumes of tissue sampled were also different, and it was conceivable that this might have accounted, at least in part, for the greater ability of the ultrafast CT method to detect differences in rCBF. Because small ROIs sample minimal amounts of tissue, there is a greater uncertainty in the CT numbers taken from such samples due to image noise, and thus there is greater uncertainty in the rCBF values derived from changes in those CT numbers. On the other hand, larger sample volumes taken from thicker scans may lead to

greater volume averaging within a given ROI, resulting in more averaging of gray and white matter within any ROI selected to be pure gray or white matter. This could also make it more difficult to detect differences in rCBF. Based on these arguments, it seemed unlikely that ROI volume alone could explain the observed differences in sensitivity between the two methods.

The absolute rCBF values determined by ultrafast CT varied over a wider range than those determined using xenon CT. The reason for this difference was unclear, but the agreement of rCBF values obtained using xenon CT and ultrafast CT with those obtained using the radiolabeled microsphere technique suggested that the difference was not due to inaccuracies in either of the CT techniques. It may have been related to the hemodynamic alterations induced by the iodinated contrast agent used in the ultrafast CT studies[107-109] and the xenon/CO_2/O_2 gas mixture used in the xenon CT studies.[83]

The variability of the ultrafast CT measurements reported here could make detection of alterations in rCBF on the basis of absolute measurements difficult. Because ultrafast CT demonstrated such good side-to-side correlations for both large (hemispheric) and small (basal ganglia) ROIs, the evaluation of relative (i.e. left-right) differences in rCBF seemed to be the most viable method of using ultrafast CT for the detection of slight rCBF alterations. Such an approach appeared to be less feasible for the analysis of xenon CT data due to the low side-to-side correlation of such data acquired from normal brain. In addition, ultrafast CT provided other hemodynamic information in addition to rCBF, including the mean transit time and vascularity. For these reasons, ultrafast CT was chosen over xenon CT as the method to study cerebrovascular alterations following focal brain irradiation.

STUDIES OF RADIATION-INDUCED CEREBROVASCULAR ALTERATIONS

Methods

<u>Animals</u> Thirteen male and 3 female purebred adult beagle dogs, 1-1.5 years old were studied. Cerebrospinal fluid (CSF) (1-1.5 ml) was collected from the cisterna magna for polyamine analysis, and 3 ml of venous blood (3 ml) was collected from a peripheral vein for determination of hematocrit and serum cortisol levels 2 weeks prior to irradiation and weekly after irradiation for up to 6 weeks. Collected CSF was spun at 2000 RPM for 10 minutes and the supernatant collected to remove any possible contamination by red or white blood cells. Baseline CSF samples were obtained at the time of chronic intravenous catheter implantation, and all subsequent samples were obtained under general anesthesia following the ultrafast CT studies. .

<u>DFMO treatment</u> A chronic intravenous catheter was implanted as described (see Appendix VII. Chronic Intravenous Catheter Implant) for the continuous infusion of either DFMO or physiologic saline. Three ml of heparinized (3 U/ml of heparin) normal saline was flushed through the line every day throughout the course of the study. In addition, 1 ml of a heparin (100 U·ml^{-1}) and penicillin (25,000 U·ml^{-1}) solution was flushed into the line and withdrawn three times weekly. Subcutaneous injections of antibiotic (penicillin G benzathine 150,000 U·ml^{-1} and penicillin G procaine 150,000 U·ml^{-1}) were administered (0.1 ml·kg^{-1}) daily, from one day before to 12 days after surgery.

In all studies, DFMO or saline infusion was started 7 days after placement of the intravenous line and 2 days before implantation of ^{125}I sources. Drug/saline treatment was continued during the 2 day irradiation period and for

14 days after removal of the implant. DFMO was supplied by the Marion Merrell Dow Research Institute, and stored in powder form in a refrigerator until use. The DFMO was weighed, diluted in physiologic saline and passed through a 0.2 μ Millipore filter immediately before use. Drug dose was 150 $mg \cdot kg^{-1} \cdot day^{-1}$ and was given by continuous infusion at a rate of 8 $ml \cdot day^{-1}$ using a calibrated infusion pump (Travenol Auto-Syringe; Travenol Laboratories, Hooksett, NH).

Nine animals were randomly assigned to the radiation plus saline group and 7 animals to the radiation plus DFMO group.

Radiation Treatment High activity ^{125}I sources ranging from 16-24 mCi were supplied by the Department of Radiation Oncology, UCSF. Under CT guidance sources were implanted into the white matter of the right frontal lobe via a twist drill hole in the skull as described (see Appendix VIII. [125]I Implant and Removal). A dose of 20 Gy was delivered to a reference point 0.75 cm away (see Appendix IX. Dose Calculation); dose rate at the reference point was approximately 45 $cGy \cdot hr^{-1}$. Radiation dose to a tissue region in the contralateral hemisphere comparable to the site of implant was calculated to be 200-300 cGy; dose rate was 4-7 $cGy \cdot hr^{-1}$. Sources remained in the brain for 38-56 hours depending upon source activity and then were removed.

Computed Tomography: Volumetric studies Computed tomographic exams were performed for implantation of ^{125}I sources and weekly thereafter for up to 6 weeks to measure pathologic changes in the brain. CT scans were analyzed for tissue attenuation (CT number) and for volumes of tissue injury. Volume of edema was determined from precontrast CT images and was defined as the volume of excess water within the right, irradiated hemisphere relative to the contralateral hemisphere (see above for details). Volumes of necrosis and

contrast enhancement (RE) were measured on post-contrast images (Figure 1; see above for details).

Transfer Constants, CBF, Mean Transit Time, and Vascularity

Measurements were done weekly from the time of ^{125}I implantation until the time of euthanasia as detailed above. Briefly, for determination of blood-to-brain transfer constants and brain-to-blood transfer constants, a series of 40 CT scans were obtained over approximately 20 minutes following the intravenous bolus infusion of 20 ml of an iodinated contrast agent. Immediately following this study, for the determination of rCBF, vascularity, and mean transit time, a series of 20 CT scans were obtained in approximately 20 seconds following the intravenous bolus infusion of 15 ml of iodinated contrast media.

Histopathology Animals were killed with a concentrated pentobarbital solution, and the brains were removed immediately after death. Samples were taken for determination of tissue polyamine levels (see below), and the remaining tissue was immersion fixed in a 10% buffered formalin solution for 1 week. Tissue samples containing the focal radiation lesion were embedded in paraffin and stained with hematoxylin and eosin. Of the 9 animals in the radiation control group, 2 were killed 2 weeks after irradiation, 3 at 4 weeks and the remaining 4 at 6 weeks after irradiation. In the radiation plus DFMO group, 2 were killed at 2 weeks after irradiation, 2 at 4 weeks and 3 at 6 weeks.

Polyamine analysis Tissue polyamine levels (putrescine, spermidine, and spermine) were determined in tissues from animals killed at 2, 4 and 6 weeks after irradiation. Tissues within the radiation lesion, including the

necrosis and the RE were obtained for analysis. CSF polyamine levels were measured from samples obtained weekly. Sample preparation and high performance liquid chromotography analysis of tissue and CSF polyamines have been described.[112]

Statistical Analysis All statistical analyses were done using the Data Desk 3.0 statistical software package (Odesta Corporation, Northbrook, IL). Analyses of variance were used to analyze the significance of the effect of radiation with and without DFMO treatment on alterations in CSF polyamine levels from baseline levels.

When there were repeated measures of parameters within individual animals, i.e., volumes of edema, necrosis, and contrast enhancement, transfer constants, vascularity, blood flow, mean transit time, CSF polyamine levels, hematocrit, and serum cortisol, mixed-model ANOVAs (see Appendix X) were used to test for the effect of DFMO *versus* saline infusion on the magnitude of those parameters. In these analyses, both drug (DFMO vs. saline) and weeks after irradiation were included as main factors. An interaction term of drug treatment and weeks after irradiation (drug-week) was included to determine if any effects of DFMO were dependent upon time after treatment. In addition, in these and all other analyses of variance, dog (number 1 to 16) was included as a factor to account for the fact that measurements were repeated weekly in each dog and such measurements were therefore not completely independent. The drug, weeks after irradiation, and interaction terms were considered fixed effects and dog number was considered a random effect. If the interaction term was significant, a Student's two-tailed *t*-test was used to determine the weeks at which the differences between the treatment groups were most significant. If the

interaction term proved to be insignificant ($p>0.10$), the term was removed and the model re-analyzed.

Mixed-model ANOVAs were also used to determine if RE volume was a significant factor in estimating edema volume independent from the effects of DFMO, and if K_i, V_p, or the interaction of K_i and V_p, had a significant influence on the estimation of edema volume. Lastly, a mixed model ANOVA was used to determine if K_i, V_p, or the interaction of K_i and V_p were significant factors in estimating RE volume.

Changes in rCBF, vascularity, and mean transit time were calculated as percent differences between regions within the irradiated hemisphere (IH) and comparable regions within the contralateral hemisphere (CH), the percent difference being defined as $100\% \cdot (\text{Value}_{IH} - \text{Value}_{CH})/\text{Value}_{IH}$ where value refers to the parameter of interest. A Student's t statistic was used to determine if the percent differences were significantly different from zero. Mixed-model ANOVAs were used to determine if edema or K_i were significantly related to changes in rCBF, vascularity, and mean transit time.

Pooled tissue polyamine levels from the DFMO and saline treated animals were compared using Fisher's exact test.

For all endpoints and analyses, significance was assigned at the $p<0.05$ level. Results with a $p<0.10$ were also reported in order to indicate trends.

Results

Implantation of the vena caval catheter, surgical implantation and removal of the ^{125}I source, CSF taps and weekly imaging procedures were well tolerated by all animals. Radiation treatments were similarly well tolerated, with only minimal neurological signs consisting of left-sided weakness and loss of conscious proprioception in the left rear limb occurring within the first 1-2

days after removal of the source. By the third day, and throughout the follow-up period, no further neurologic signs were observed.

Saline Treated Animals In animals treated with radiation plus saline, CSF putrescine levels were significantly elevated from baseline levels at 1 (Figure 14) and 6 weeks post-irradiation, CSF spermidine levels were elevated at 4 weeks, and CSF spermine was not significantly altered from baseline at any time. In agreement with previously reported results,[52] necrosis and edema volume within this group peaked 3-4 weeks after removal of the ^{125}I source and began to decrease after 4 weeks (Figures 15 and 16). In contrast, the volume of contrast enhancement continued to increase throughout the course of the follow-up period (Figure 17).

Measurements of K_i and K_b within the radiation plus saline treated animals demonstrated that blood-to-brain and brain-to-blood transfer of iodinated contrast was increased relative to normal values (i.e. 0) throughout the follow-up period. The rates appeared to plateau at 1-2 weeks after irradiation before further increases from 3-6 weeks (Figure 18).

Average blood flow parameters were significantly altered within all regions of the hemisphere containing the focal radiation lesion (Figures 19-22). Within the lesion itself (Figure 19), blood flow was significantly decreased by 20-40% relative to a comparable region within the opposite hemisphere throughout the follow-up period. Vascularity was significantly decreased 20-35% from 1-3 weeks after irradiation before becoming significantly increased by 70% at 6 weeks. Mean transit time was not significantly altered until late in the follow-up period; it was increased at 4 and 6 weeks post-irradiation by 30 and 130%, respectively.

Blood flow changes within brain surrounding the lesion (i.e. within the hemisphere containing the lesion but outside the region of necrosis and

Figure 14   Cerebrospinal fluid putrescine, spermidine, and spermine levels (mean ± SE) in dogs that received radiation plus saline infusion (●) or radiation plus DFMO infusion (▲), as a function of time after removal of a single ^{125}I source.   The asterisks represent significant ($p<0.05$) differences in the polyamine level relative to the baseline values (i.e. the values at 0 weeks after irradiation, n=11).   Sample sizes at 1, 2, 3, 4, and 6 weeks after irradiation were 8, 7, 5, 5, and 2 for the saline treated group and 4, 5, 3, 2, and 1 for the DFMO treated group.

Figure 15   Volume of necrosis (mean ± SE) as a function of time after removal of a single ^{125}I source in animals treated with either radiation plus saline (●) or radiation plus DFMO (▲). An analysis of variance indicated that DFMO treatment altered necrosis volume and that the effect was dependent upon time after irradiation.   The daggers indicate the points at which the differences in the volumes for the two treatment groups were most significantly different ($p<0.10$ for all) according to a Student's t test. Sample sizes at 1, 2, 3, 4, and 6 weeks after irradiation were 8, 8, 5, 6, and 3 for the saline treated group and 4, 7, 5, 3, and 3 for the DFMO treated group.
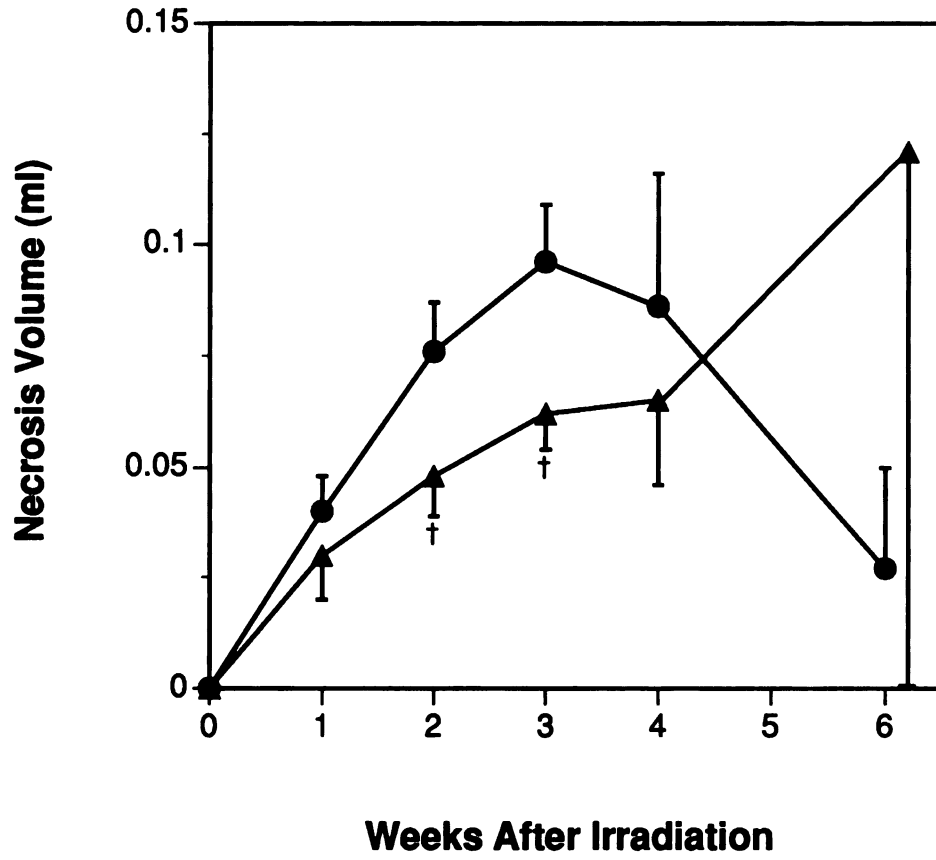
Figure 16   Volume of edema (mean ± SE) as a function of time after removal of a single ^{125}I source in animals treated with either radiation plus saline (●) or radiation plus DFMO (▲). An analysis of variance demonstrated that the DFMO altered the volume of edema, and the effect was dependent upon time after irradiation. The asterisks indicate the points at which the volume of edema of the DFMO group was most significantly different ($p<0.05$) from the saline group. Sample sizes at 1, 2, 3, 4, and 6 weeks after irradiation were 9, 9, 7, 7, and 4 for the saline treated group and 6, 7, 5, 5, and 3 for the DFMO treated group.
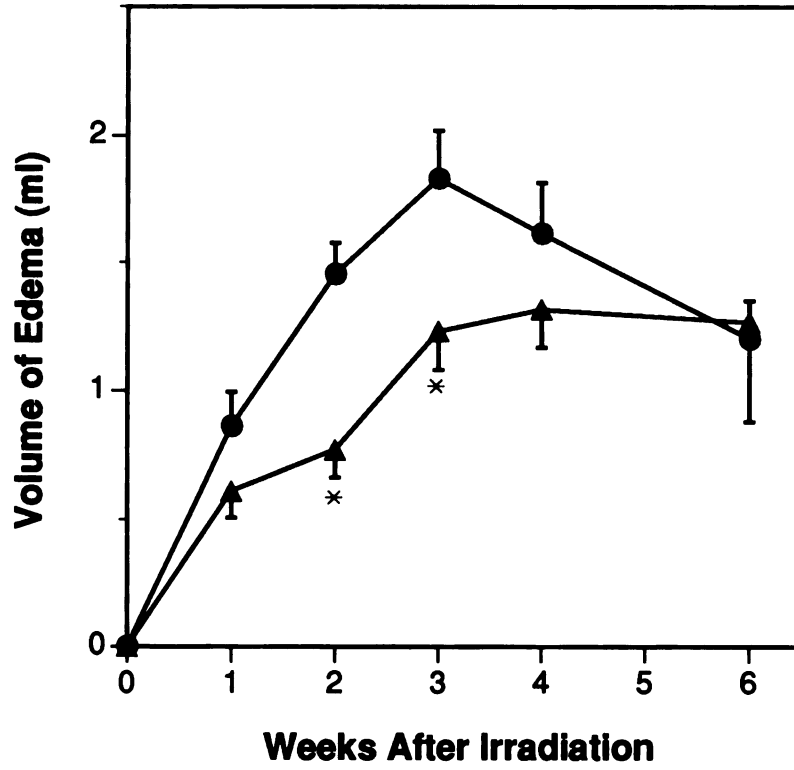
Figure 17   Volume of the ring of contrast enhancement (RE) (mean ± SE) as a function of time after removal of a single ^{125}I source in animals treated with either radiation plus saline (●) or radiation plus DFMO (▲). An analysis of variance indicated that DFMO treatment altered RE volume and that the effect was dependent upon time after irradiation.   The daggers indicate the points at which the differences in the volumes for the two treatment groups were most significantly different ($p<0.10$ for all) according to a Student's t test.   Sample sizes at 1, 2, 3, 4, and 6 weeks after irradiation were 8, 8, 5, 6, and 3 for the saline treated group and 4, 7, 5, 3, and 3 for the DFMO treated group.
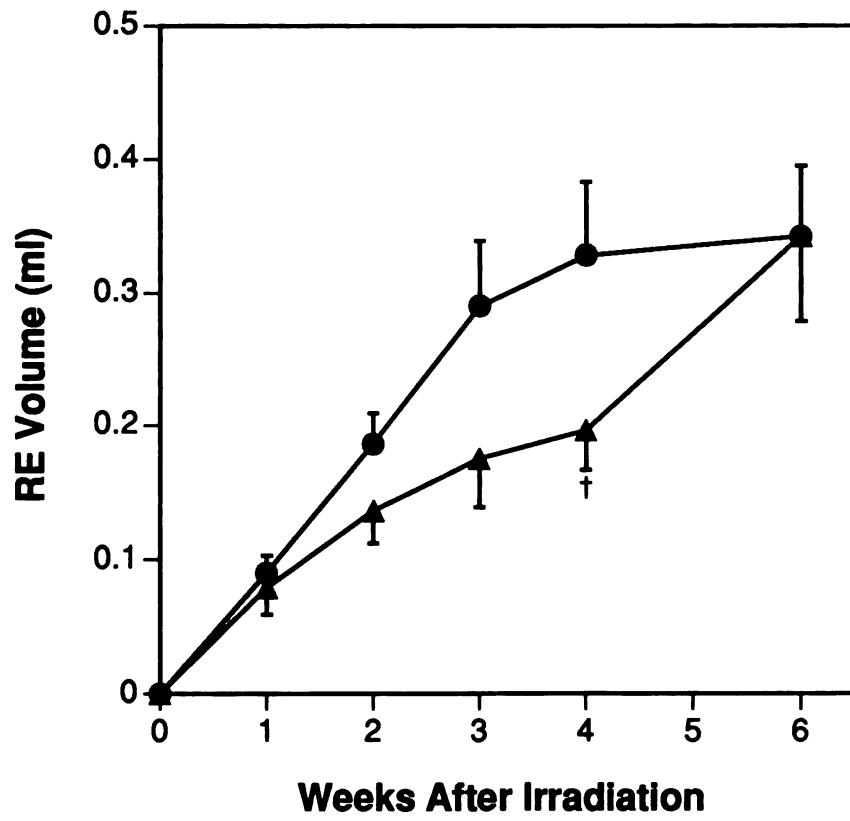
Figure 18   Blood-to-brain (K_i, top) and brain-to-blood (K_b, middle) transfer constants and vascularity (V_p, bott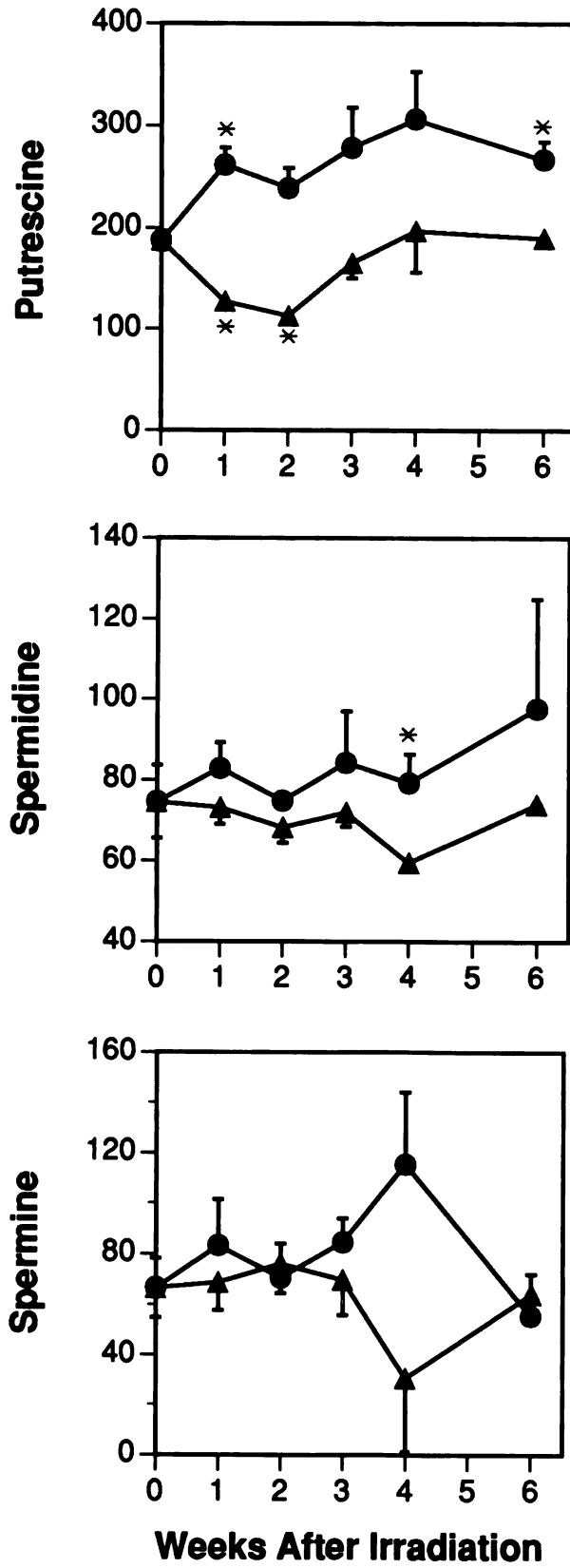om) (mean $\pm$ SE) as a function of time after removal of a a single ^{125}I source in animals treated with either radiation plus saline ($\bullet$) or radiation plus DFMO ($\blacktriangle$). An analysis of variance demonstrated that the pattern of change of all three parameters as a function of time after irradiation was significantly altered in the DFMO treatment group. The asterisks indicate the time points at which the parameters for the two treatment groups were most significantly different ($p<0.05$) according to a Student's t test. Sample sizes at 1, 2, 3, 4 and 6 weeks after irradiation were 8, 8, 5, 6 and 3 for the saline treated group and 4, 7, 5, 3, and 2 for the DFMO treated group.

Weeks After Irradiation
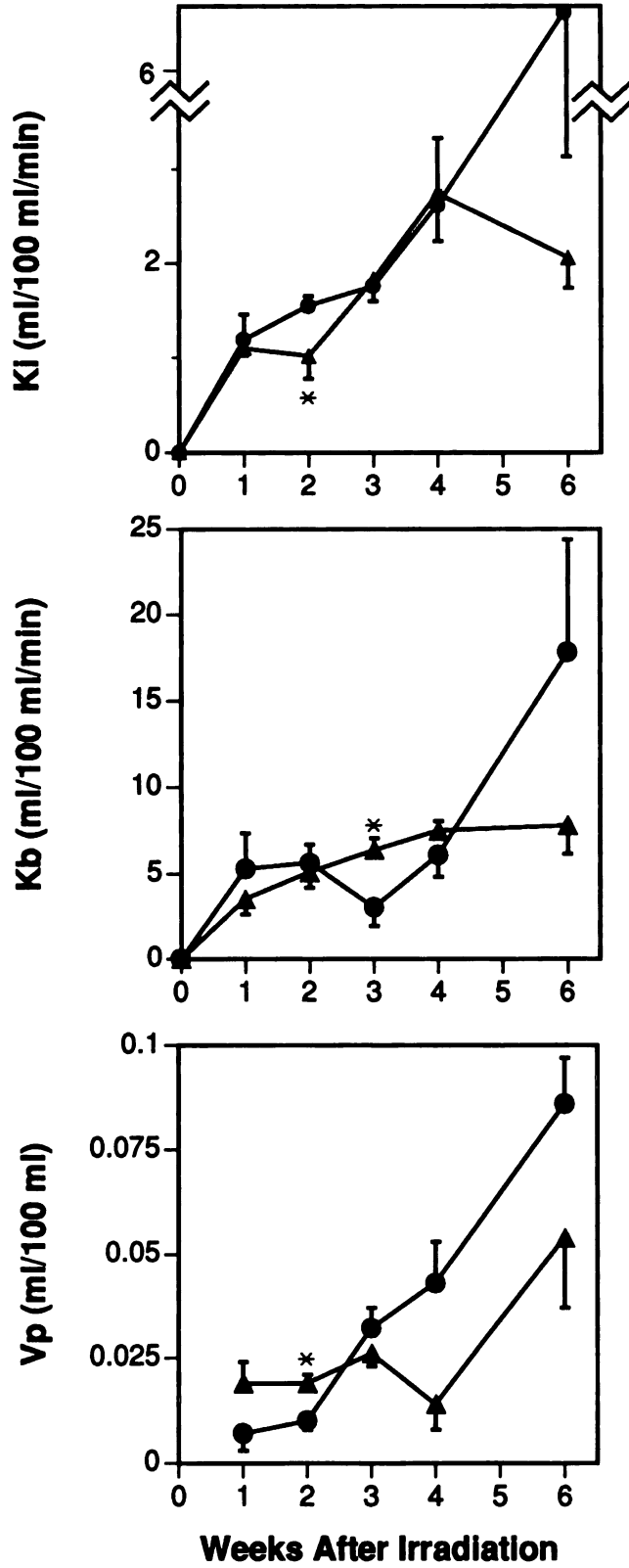
Figure 19   Percent differences (mean ± SE) in blood flow (top), vascularity (middle), and mean transit time (bottom) within the focal radiation lesion relative to a comparable region within the contralateral hemisphere as a function of time after removal of a a single ^{125}I source in animals treated with either radiation plus saline (solid bars) or radiation plus DFMO (gray bars). The asterisks represent the time points at which the lesion values were significantly altered ($p<0.05$) relative to the contralateral region according to a Student's t statistic. An analysis of variance suggested that DFMO administration may have altered the percent differences in vascularity (p=0.055) and mean transit time (p=0.091), and the effect was dependent upon time after irradiation. The dagger indicates the point at which the percent differences in vascularity for the two treatment groups were most significantly different ($p<0.05$) according to a Student's t test. Sample sizes at 1, 2, 3, 4 and 6 weeks after irradiation were 8, 8, 4, 5, and 3 for the saline treated group and 4, 7, 5, 4, and 3 for the DFMO treated group. Percent difference=100%·(Lesion Value - Contralateral Value)/Contralateral Value.
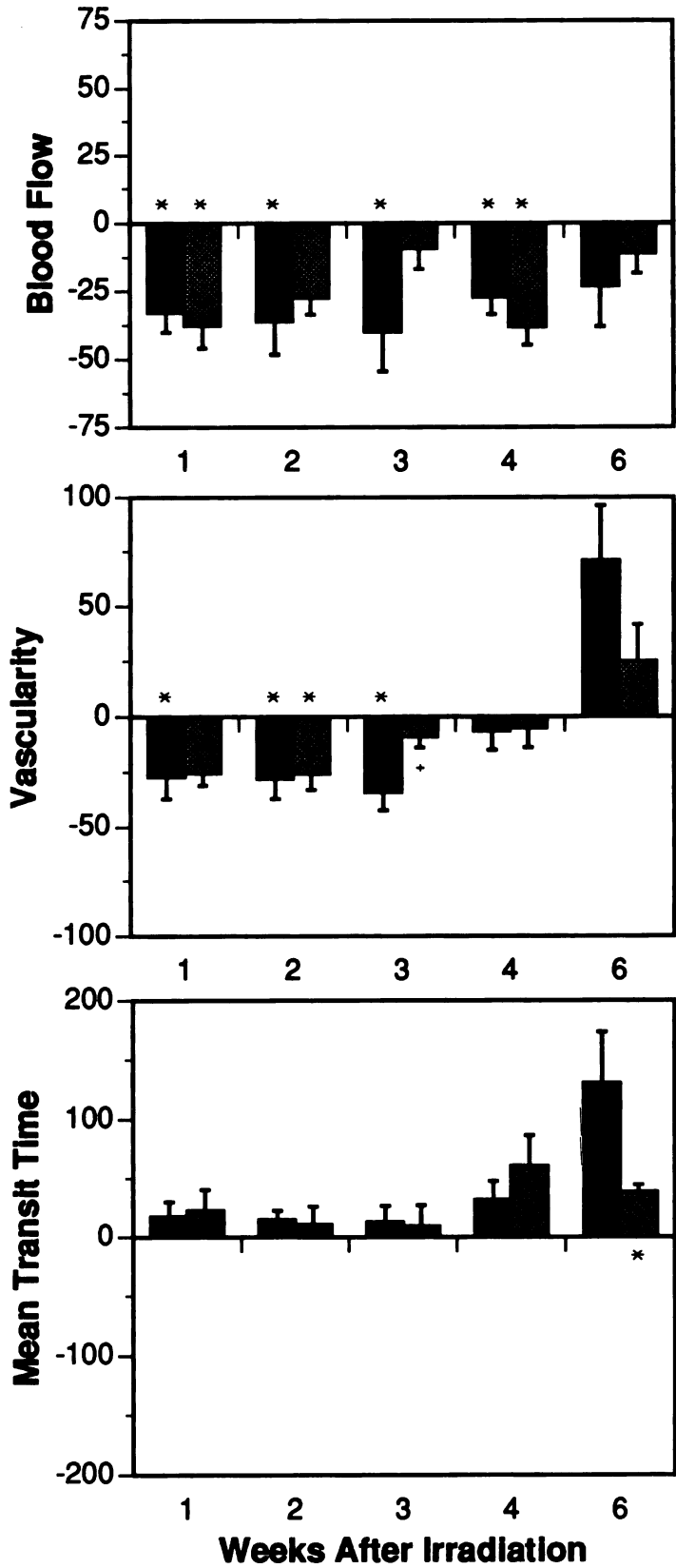
Figure 20   Percent differences (mean ± SE) in blood flow (top), vascularity (middle), and mean transit time (bottom) within the brain surrounding the focal radiation lesion relative to a comparable region within the contralateral hemisphere as a function of time after removal of a single ^{125}I source in animals treated with either radiation plus saline (solid bars) or radiation plus DFMO (gray bars). The asterisks represent the time points at which the values within the region of brain surrounding the lesion were significantly altered ($p<0.05$) relative to a comparable contralateral region according to a Student's t statistic. There were no significant differences between the DFMO and saline treated groups by ANOVA. Sample sizes at 1, 2, 3, 4 and 6 weeks after irradiation were 8, 8, 4, 5, and 3 for the saline treated group and 4, 7, 5, 4, and 3 for the DFMO treated group. Percent difference=100%·(Brain Surrounding Lesion Value - Contralateral Value)/Contralateral Value.
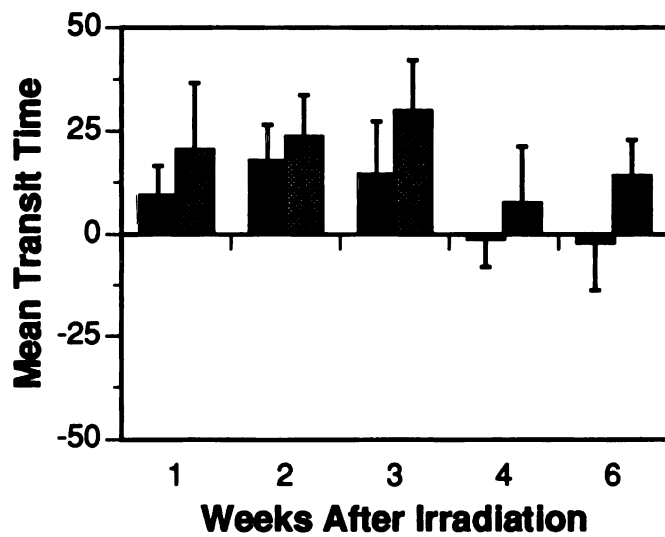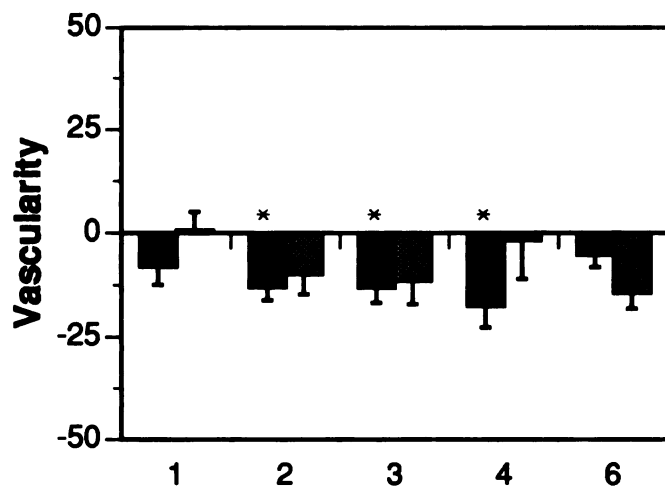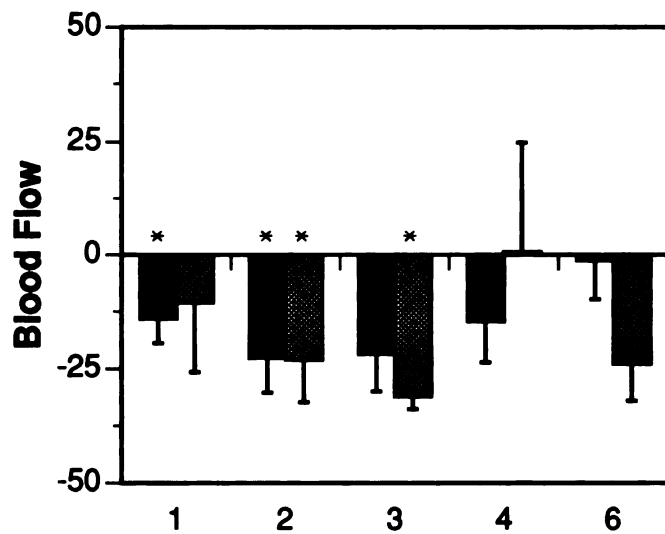
Figure 21   Percent differences (mean ± SE) in blood flow (top), vascularity (middle), and mean transit time (bottom) within the white matter of the irradiated hemisphere relative to a comparable region within the contralateral hemisphere as a function of time after removal of a a single ^{125}I source in animals treated with either radiation plus saline (solid bars) or radiation plus DFMO (gray bars). The asterisks represent the time points at which the values within the region of brain surrounding the lesion were significantly altered ($p<0.05$) relative to a comparable contralateral region according to a Student's t statistic. There were no significant differences between the DFMO and saline treated groups by ANOVA. Sample sizes at 1, 2, 3, 4 and 6 weeks after irradiation were 8, 8, 4, 5, and 3 for the saline treated group and 4, 7, 5, 4, and 3 for the DFMO treated group. Percent difference=100%·(Irradiated White Matter Value - Contralateral Value)/Contralateral Value.
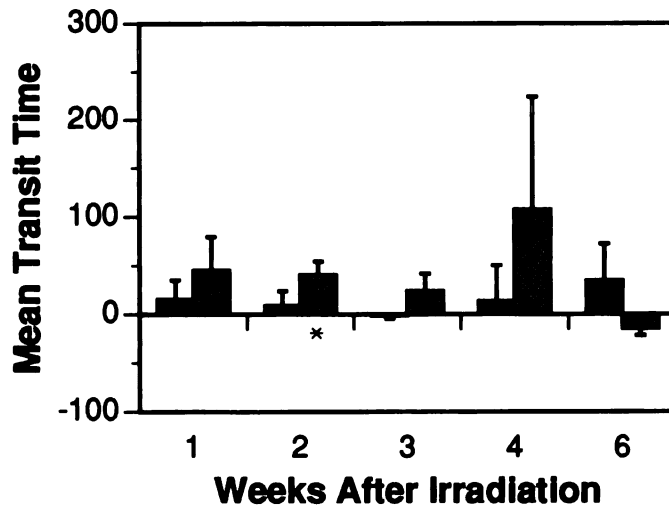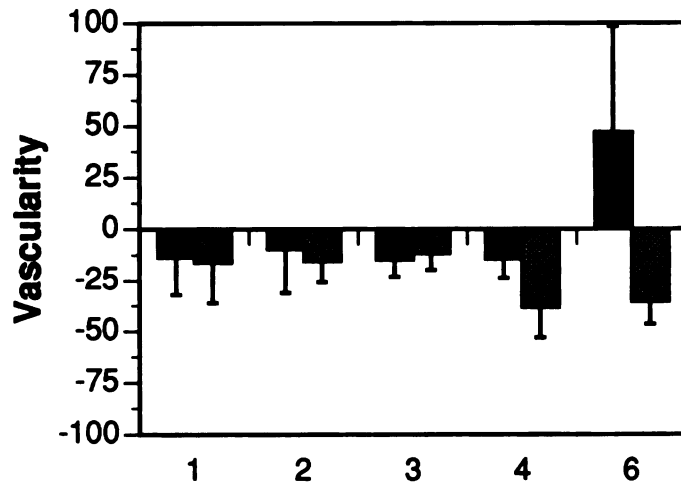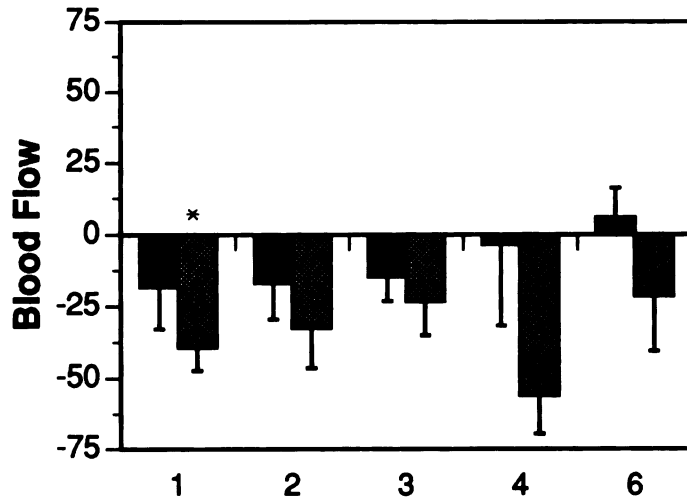
Figure 22   Percent differences (mean ± SE) in blood flow (top), vascularity (middle), and mean transit time (bottom) within the gray matter of the irradiated hemisphere relative to a comparable region within the contralateral hemisphere as a function of time after removal of a single ^{125}I source in animals treated with either radiation plus saline (solid bars) or radiation plus DFMO (gray bars). The asterisks represent the time points at which the values within the region of brain surrounding the lesion were significantly altered (p<0.05) relative to a comparable contralateral region according to a Student's t statistic. There were no significant differences between the DFMO and saline treated groups by ANOVA. Sample sizes at 1, 2, 3, 4 and 6 weeks after irradiation were 8, 8, 4, 5, and 3 for the saline treated group and 4, 7, 5, 4, and 3 for the DFMO treated group. Percent difference=100%·(Irradiated Gray Matter Value - Contralateral Value)/Contralateral Value.
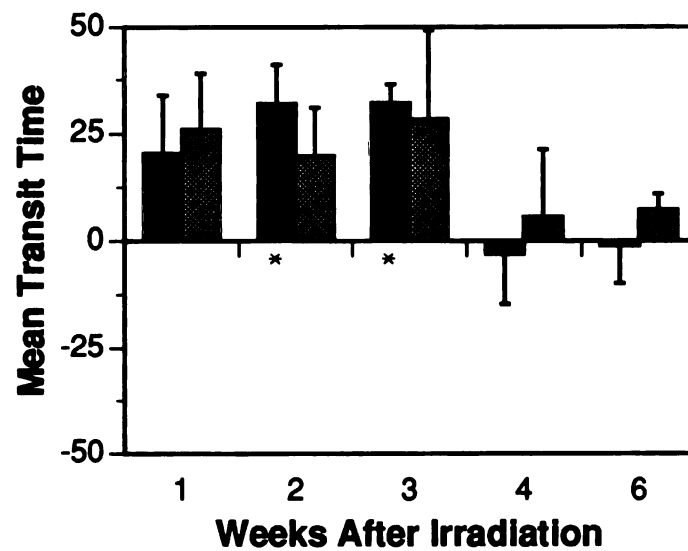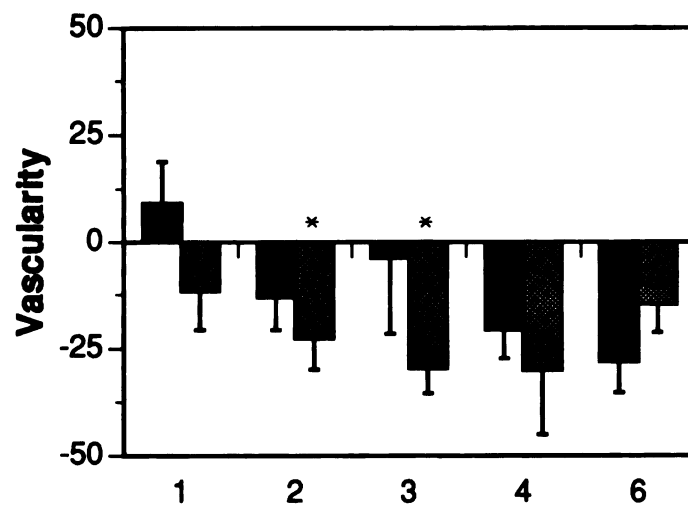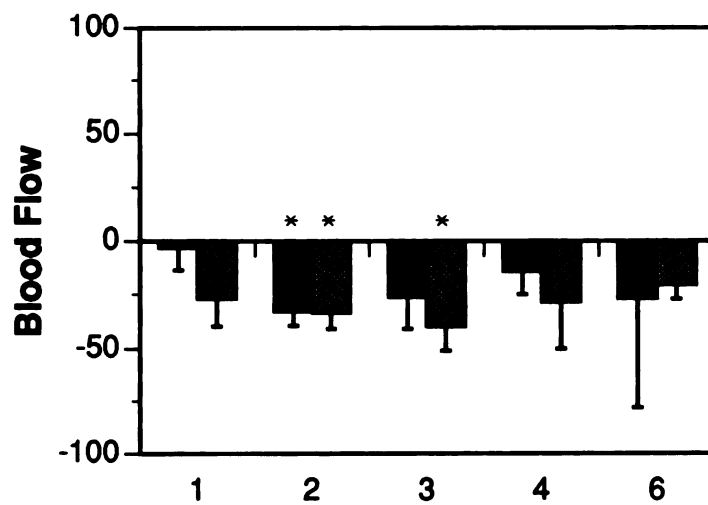
contrast enhancement) appeared to mirror the changes in volume of edema, with the greatest decreases in blood flow occurring at approximately the time of maximum edema (Figures 16 and 20). Blood flow changes in the specific regions of white matter and gray matter were similar (Figures 21 and 22). Blood flow within surrounding brain was significantly reduced relative to contralateral blood flow by 14-23% at 1-3 weeks; at 6 weeks, there was virtually no detectable alteration in blood flow. Vascularity was also reduced within this region with significant decreases in vascularity of 13-18% at 2-4 weeks. Mean transit time was increased by 10-18% at 1-3 weeks, although the only significant change was at the 2 week time point.

An ANOVA was used to examine the relationship between alterations in blood flow, edema, and blood-to-brain transfer. Both edema and blood-to-brain transfer were found to be significant factors in predicting changes in blood flow within surrounding brain (Figure 20). They were also significant factors in determining the alterations in mean transit time but not the alterations in vascularity. The inclusion of blood-to-brain transfer in the model increased the significance of edema volume as a predictor of blood flow (p=0.0009 *versus* p=0.0028) and as a predictor of mean transit time (p=0.0022 *versus* p=0.01).

DFMO Treated Animals Administration of DFMO resulted in gastrointestinal changes, including vomiting and diarrhea, during the last 1-2 days of drug treatment in 3 of the 7 animals; based on skin turgor, 2 of the 3 dogs showed some degree of dehydration. Twenty-four hours after discontinuing the drug, all clinical signs of dehydration subsided. Although an ANOVA suggested (p<0.10) that the hematocrit might be altered by the presence of DFMO depending upon the time after irradiation, there were no significant differences (Student's t test; p>0.10) in hematocrit at the time of dehydration or any other time point. In addition, there were no significant

differences in CT number of the contralateral hemisphere or serum cortisol levels between animals that received radiation plus saline or radiation plus DFMO (ANOVA; $p>0.10$).

In contrast to saline controls, CSF putrescine levels in animals that received DFMO were significantly reduced relative to baseline at 1 and 2 weeks (Figure 14), and CSF spermidine levels were not significantly altered from baseline. ANOVAs demonstrated significant differences in CSF putrescine and spermidine levels between the saline and DFMO treated groups. There were no significant differences in average CSF spermine levels between the 2 treatment groups.

There was a wide variability in putrescine levels within the regions of necrosis and contrast enhancement with ranges of 5-204 nmol·ml^{-1} for saline treated animals and below detectable limits (< 5 nmol·ml^{-1}) - 166 nmol·ml^{-1} for DFMO treated animals. The variability combined with the small numbers of samples analyzed, made it impossible to determine significant alterations in putrescine as a function of time or treatment. However, a significantly greater proportion of samples from the DFMO treated group had putrescine levels below detectable limits (7 of 14 for DFMO group vs. 0 of 16 for saline group; Fisher's Exact test). There were no apparent differences in spermidine or spermine levels between the 2 treatment groups.

An ANOVA was performed on data from sequential CT studies and showed that volume of edema was significantly reduced in DFMO treated dogs, and that the reduction was dependent upon week after irradiation (Figure 16). In addition, there was a significant effect of DFMO on both necrosis and RE volume that was dependent upon time after irradiation. Although the time response of the DFMO treated animals was similar to that of the saline treated animals, the average volume of necrosis was reduced relative to radiation plus

saline at all time points except 6 weeks where 1 out of 3 animals showed an increase in necrosis volume (Figure 15). The average RE volume in DFMO treated animals was reduced relative to saline treated dogs at 2, 3, and 4 weeks after irradiation (Figure 17).

ANOVA showed that the interaction term of drug treatment and week after irradiation was a significant factor in determining the magnitude of K_i, K_b, and V_p, suggesting that DFMO altered the pattern of change in all three of these parameters as a function of time following irradiation (Figure 18).

Because of a strong correlation between K_b and V_p, K_b was not included in the mixed model ANOVAs assessing the influence of various vascular-related parameters on RE and edema volume. These analyses indicated that both RE volume and the interaction of K_i and V_p were significant factors in predicting the volume of edema and that the interaction of K_i and V_p was also significant factor in predicting the RE volume.

The changes in the blood flow in the focal lesion of the DFMO treated animals were not significantly different from those of the saline controls (Figure 19) (ANOVA, $p>0.10$), but ANOVA suggested that the interaction term of drug treatment and week after irradiation might be a significant factor in determining the change in vascularity ($p=0.055$) and mean transit time ($p=0.091$), suggesting that DFMO administration altered the pattern of change in these two parameters. However, there was no evidence (ANOVA, $p>0.10$) to suggest that DFMO significantly altered the blood flow changes occurring after irradiation within regions outside the focal lesion (Figures 20-22).

Histopathology Histopathologic analysis of tissues showed no apparent difference between animals that received radiation alone and animals that received radiation plus DFMO. The changes observed were similar to those previously reported.[52] At 2 weeks, a focus of coagulation necrosis was

observed within which were blood vessels with fibrinoid necrosis of vessel walls (Figure 23). The reactive tissue immediately around the necrosis, i.e. the RE on CT scan, showed variable degrees of vessel damage ranging from fibrinoid necrosis of capillary walls and piling up of cells perivascularly to normal appearing and apparently patent vessels (Figure 23). In some regions, an eosinophilic exudate was present perivascularly. Swollen axis cylinders were noted (Figure 24), and there was considerable tissue rarefraction, indicative of edema. There was no apparent increase in glial cells. At 4 weeks there still was some necrotic tissue at the site of the implant, but there was much more reactive tissue including the presence of macrophages and the appearance of fibrous tissue (Figure 25). Endothelial cell proliferation was also observed. At six weeks, the previously necrotic tissue was completely replaced with fibrous tissue, new blood vessels, and macrophages (Figure 26). The amount of microscopic edema was reduced relative to earlier times.

Figure 23   Histopathologic section of the brain taken 2 weeks after removal of a single ^{125}I source demonstrating the region of necrosis and surrounding tissue. The top photograph (magnification 40X) is centered such that the focus of necrosis is visible to the left and relatively normal tissue is visible to the far right. Numerous blood vessels with fibrinoid necrosis of vessel walls are visible within the necrotic region (arrows). Outside this necrotic region, the vessel damage is variable ranging from fibrinoid necrosis of vessel walls (arrowheads) and piling up of perivascular cells (white arrows) to normal appearing and apparently patent vessels (open arrows). The bottom photograph (magnification 100X) demonstrates perivascular accumulation of exudate (open arrows) and tissue rarefaction (arrows).
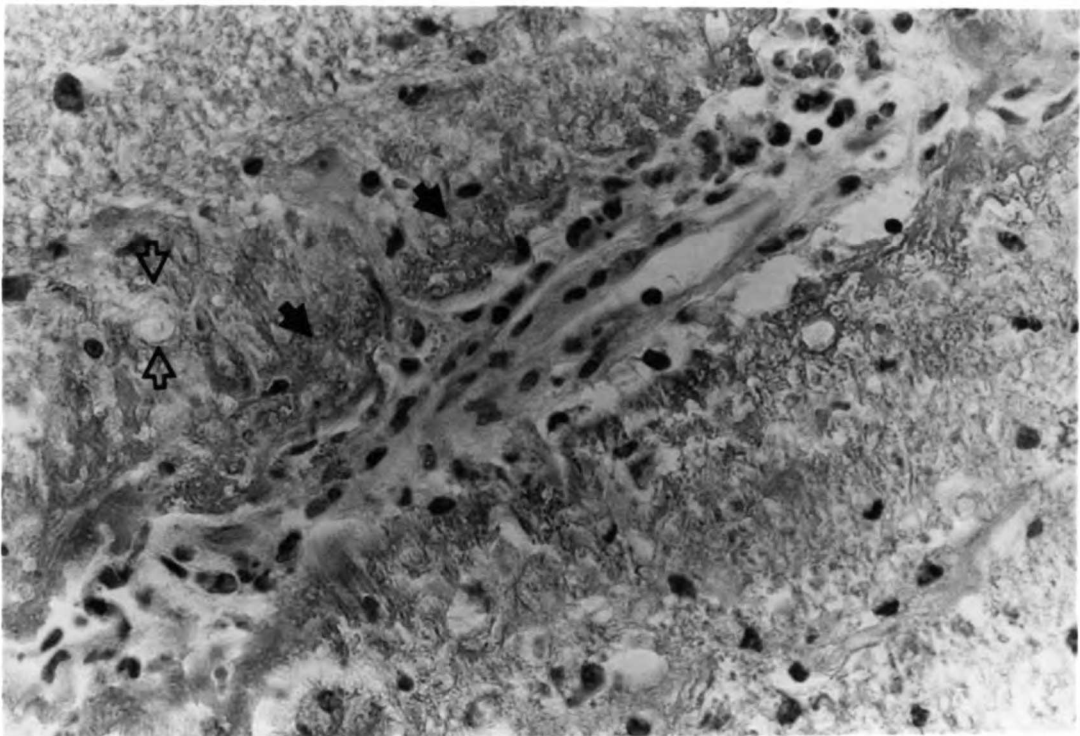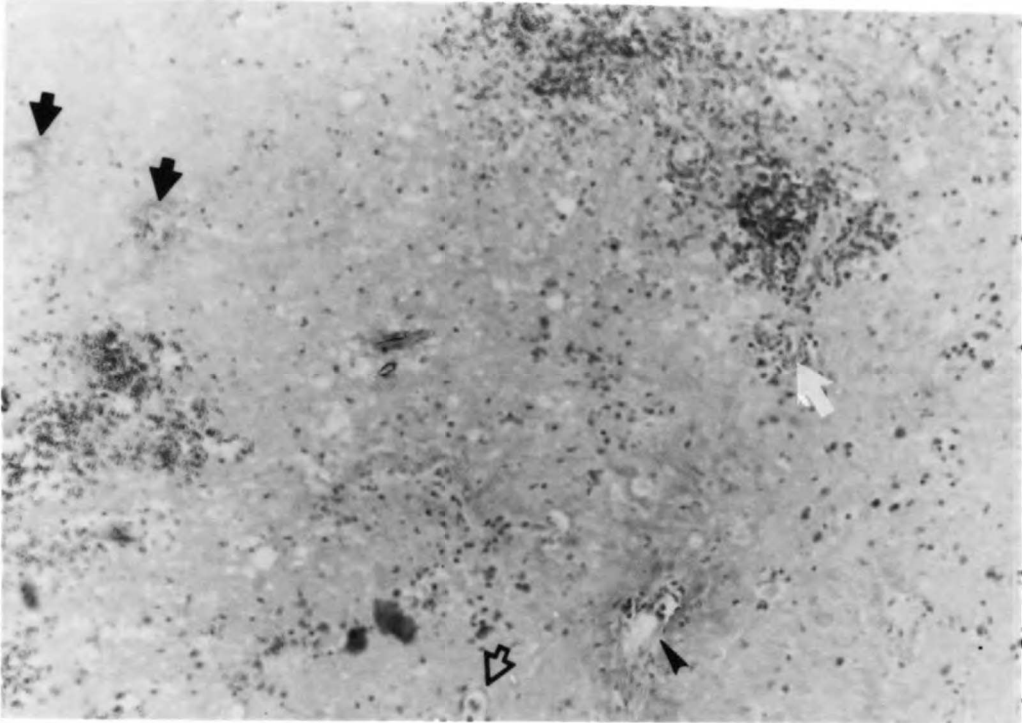
Figure 24   Histopathologic section (magnification 100X) of the brain taken 2 weeks after removal of a single ^{125}I source demonstrating a swollen axis cylinder (arrow).
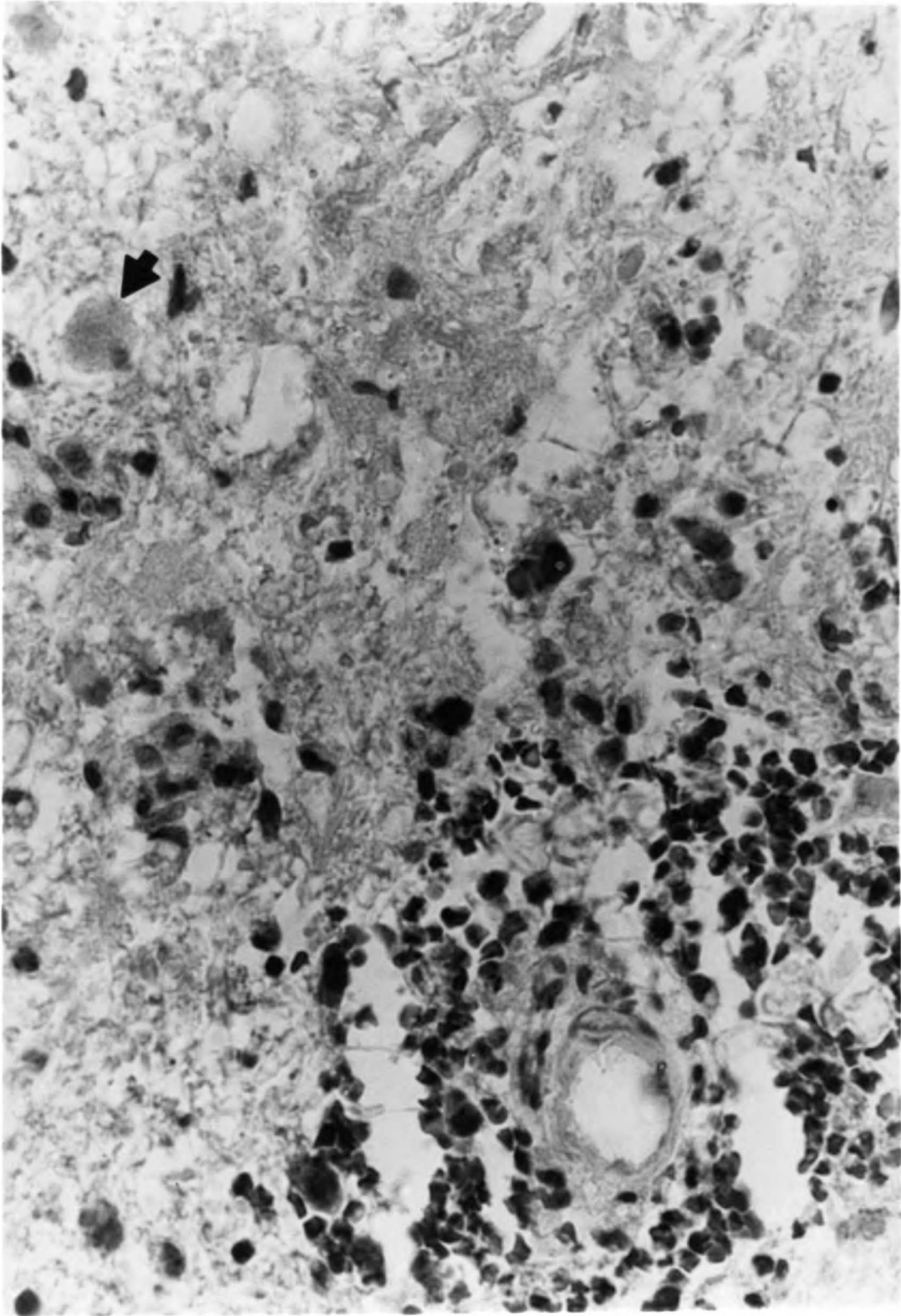
Figure 25   Histopathologic section of the brain taken 4 weeks after removal of a single ^{125}I source. The top photograph (magnification 100X) demonstrates the influx of macrophages (closed arrows), visible as large, round cells with fairly abundant cytoplasm, and vessels (open arrows), visible due to the presence of red blood cells within their lumens, into the necrotic region. The bottom photograph (magnification 100X) also shows an influx of vasculature (open arrows) as well as fibroblast-like cells (arrowheads), which are characterized by their spindle shape.
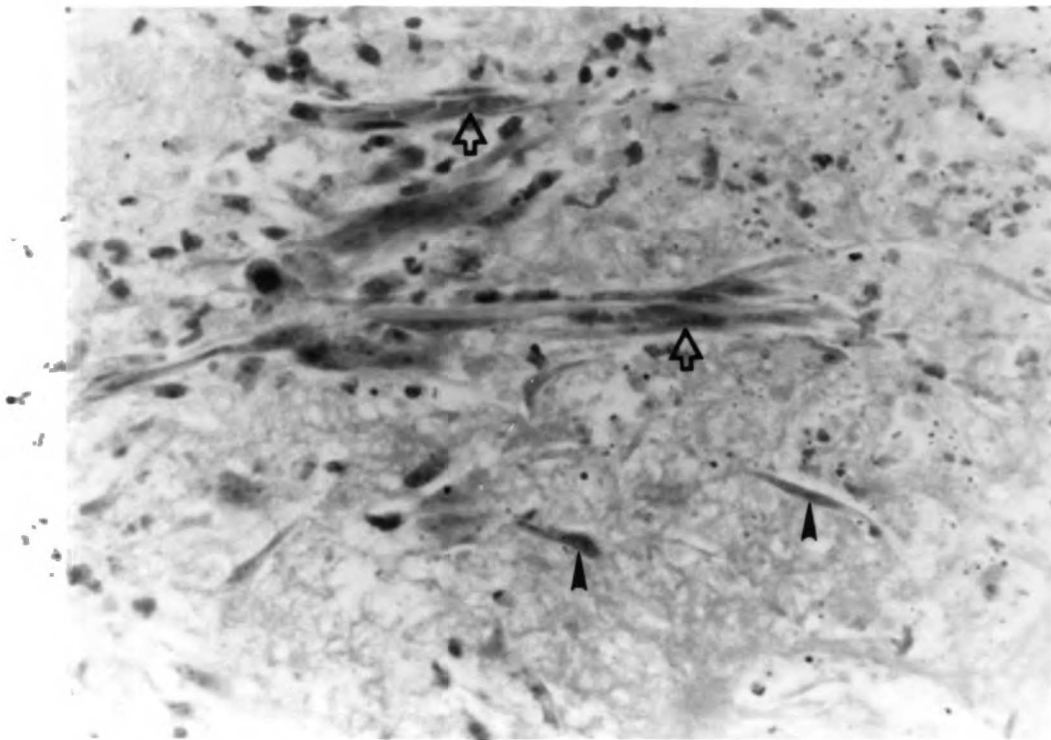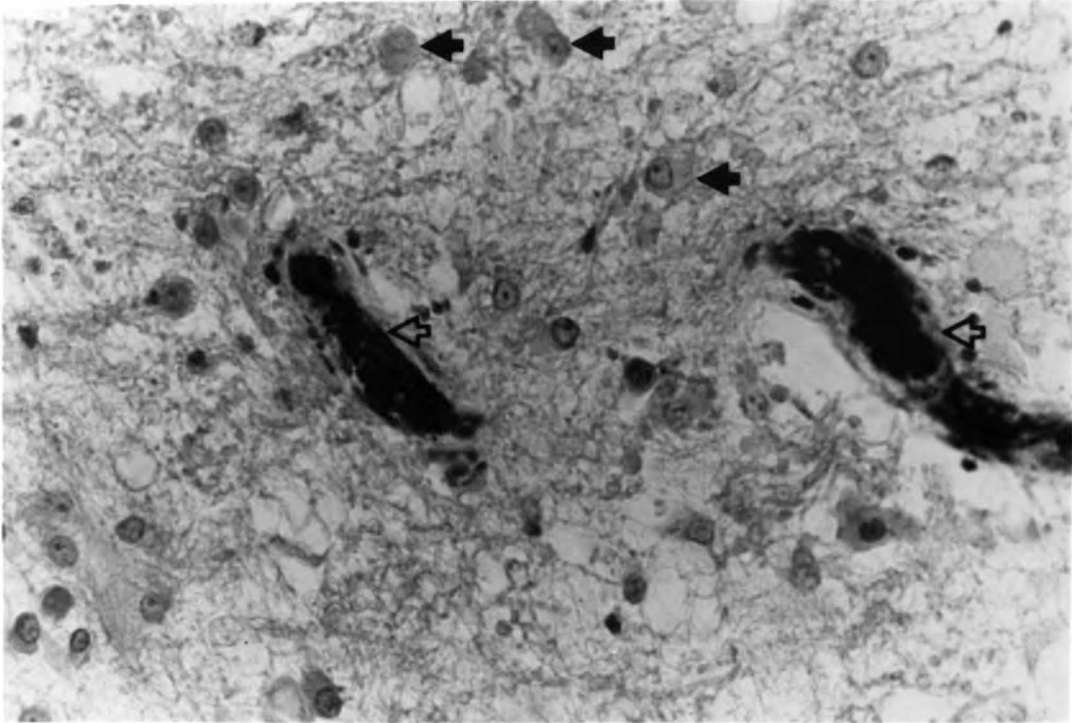
Figure 26   Histopathologic section (magnification 100X) of the brain taken 6 weeks after removal of a single ^{125}I source. The previously necrotic region has been almost completely replaced by macrophages (arrows), visible as large, round cells with fairly abundant cytoplasm, fibrous tissue and fibroblast-like cells (arrowheads), which are characterized by their spindle shape, and new capillaries (open arrows), which are visible due to the presence of red blood cells within their lumens.
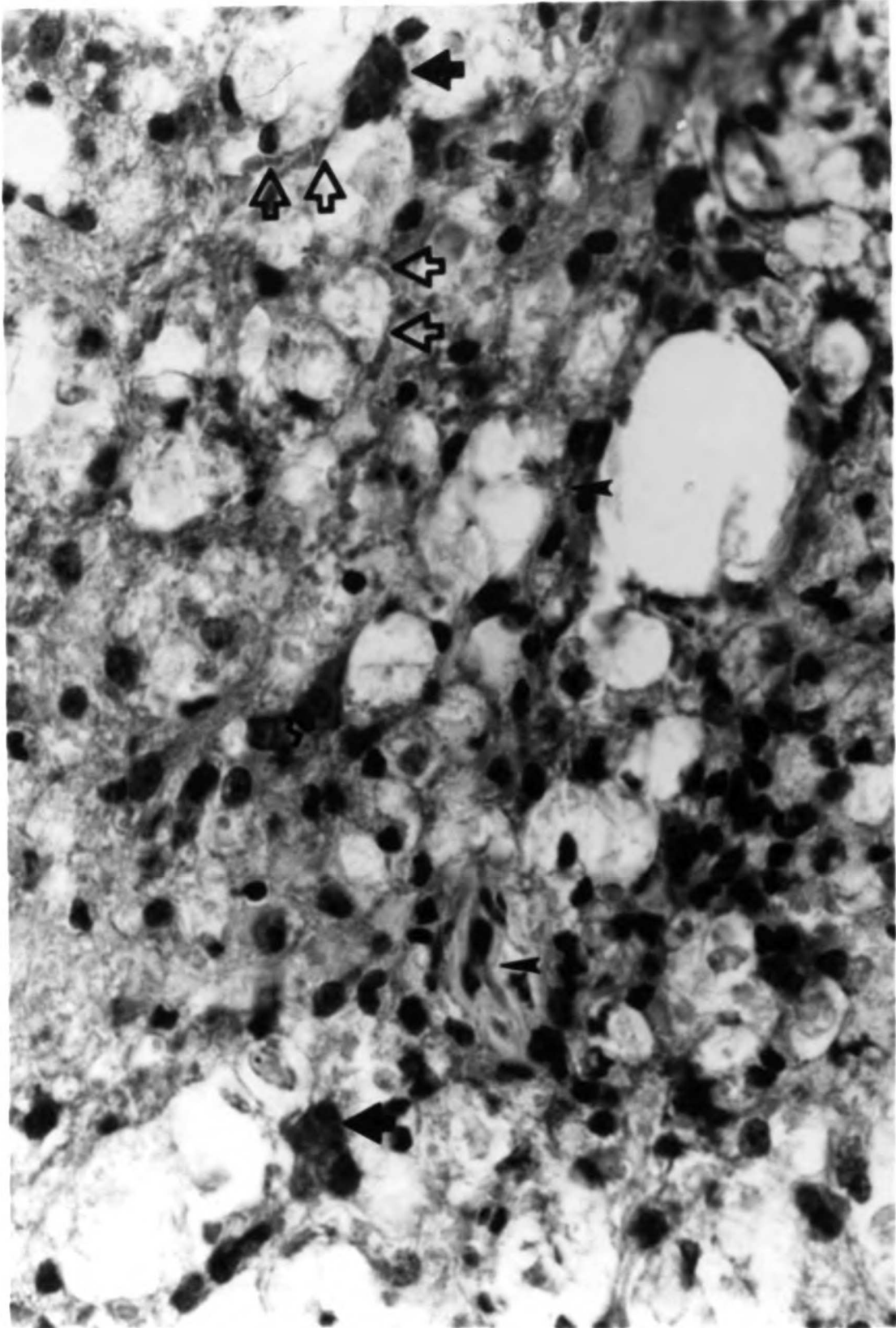
DISCUSSION AND CONCLUSIONS

OVERVIEW

Radiation-induced brain injury is characterized by cell death, BBB breakdown, and vasogenic edema, similar to other types of brain injury, such as ischemic infarction or traumatic compression.[45, 113-115] However, unlike other types of brain injury, radiation-induced injury continues to develop over a prolonged period of time - weeks in the case of the canine model used in the present study and months in the case of irradiated brain tumor patients. The prolonged development is undoubtedly related to the slow turnover and thus slow mitotic-linked death of the proliferating brain cell populations, such as the glial and endothelial cells.[17-20] The mitotic-linked death results from lack of repair or misrepair of radiation-induced DNA damage so that the DNA cannot be properly allocated during cell division.[116] Although it is apparent from this that DNA damage plays a significant role in the development of radiation brain injury, there are also indications that physiologic factors, such as blood pressure and cerebrovascular permeability,[36, 37, 48] and the interdependence of cell populations within a tissue, such as the dependence of all cells on vascular endothelial integrity,[31] can also influence the development of injury. Understanding the role that physiologic factors play in radiation injury could provide clues as to how to modify of that injury. The present study was undertaken to better understand the relationship between physiologic changes occurring after focal brain irradiation and the development of injury so that possible methods of modifying injury, unrelated to modifying DNA damage, might become clearer.

A canine model of focal radiation brain injury was used because of its similarities to the radiation necrosis that occurs in brain tumor patients treated with brachytherapy.[1, 52, 117] In addition, the injury develops over a relatively

short period of time compared to that following hemibrain irradiation, so that studies of post-irradiation physiologic changes can be focused within a reasonably short time. Lastly, because of the well characterized and reproducible morphologic character of the injury, it was postulated that physiologic alterations would be reproducible, which would facilitate characterization of those physiologic changes.

Radiation injury in the dog model has been characterized radiographically by a focus of low density surrounded by a ring of tissue that is markedly enhanced by iodinated contrast media (Figure 1). The low density corresponds to necrosis, and the histologic character of the surrounding region suggests that the ring corresponds to a region with vascular damage in the early stages of development (Figure 23 and 24) and vascular proliferation in the latter stages (Figures 25 and 26). The cell death that occurs within 1-2 mm of the radioactive implants, where radiation dose can approach 1000 Gy, is probably due to interphase death and presumably occurs acutely (within 24-48 hours of the insult) as in ischemic injury.[113] The continued increase in lesion size for up to 4 weeks after irradiation (Figure 15) is probably due in part to mitotic-linked death of cells, which would account for the delay in the expression of injury as mentioned above. Evidence of a proliferative response is provided by the histologic demonstration of regions of vascular thickening due to piling up of cells in perivascular regions (Figure 23). As vascular endothelial and/or glial cells die, there is a loss of BBB integrity, which leads to the leakage of blood-borne molecules that are normally excluded from the brain interstitium, such as albumin and other plasma proteins (Figure 24). This leakage likely leads to greater osmotic pressure within the brain interstitium and thus leads to increased brain water to offset this gradient.[118] This probably accounts for the relationship between the RE volume, which is the leaky region,

and edema volume, which was reported previously [52] as well as in the present study. In addition, cellular breakdown after cell death also likely increases interstitial osmolarity and brain water due the release of cellular constituents, such as proteins and membrane lipids. This probably accounts for the observation that the amount of edema parallels the volume of necrosis. Eventually the necrotic region is replaced by the influx of macrophages, fibrous tissue, and neovasculature (Figure 26) so that the amount of edema and volume of necrosis are eventually reduced (Figures 15, 16, and 27).

Although the relationship of necrosis and contrast enhancement to edema volume had been examined prior to the present study, no quantitative measures were used to definitively establish a relationship between blood-to-brain transfer of materials and edema.[52] In addition, prior to the present work, there had been no known studies to determine if edema leads to vascular compression and ischemia and whether such effects might exacerbate radiation-induced damage. The development and validation of non-invasive, computed tomographic methods of measuring edema volume, blood-to-brain and brain-to-blood transfer constants, rCBF, blood mean transit time, and vascularity made it possible to quantitatively and sequentially evaluate the relationship of these parameters to the evolution of radiation injury. More specifically, the development of these methods made it possible to determine whether BBB breakdown was related to edema formation, whether edema formation might lead to vascular compression and ischemia, and whether modification of BBB breakdown might reduce the amount of edema, the extent of ischemia, and thus the overall extent of tissue injury.

Figure 27   Graphs illustrating a model of the cellular basis of the formation and radiographic resolution of a focal radiation lesion. The amount of cell death and cell proliferation as a function of time after irradiation is assumed to be sigmoidal in shape. As the amount of cell death increases due to cells undergoing both interphase and mitotic-linked death (top left, solid line), the size of the focal radiation lesion increases (top right). Eventually, some non-lethally irradiated cells are able to mount a proliferative response (top left, dashed line) such that the focal lesion decreases in size. The focal lesion size at any time (right graphs) is a function of the difference (shown as solid bars) between the total amount of cell death (solid line, left) and the total amount of cell proliferation occurring up to that time (dotted line, left). The maximal size of the lesion (middle right, solid line) can be reduced if the rate of cell death is slowed (middle left, solid line) while the rate of cell proliferation stays the same (middle, left graph, dashed line). The maximal size of the lesion can also be reduced if the rate of cell death is slowed (bottom left, solid line) and the rate of cell proliferation is also slowed (bottom left, dashed line), but the resolution of the lesion (reduction of lesion size to zero) will be delayed. The focal lesion size from the top left graph (i.e. normal rate of cell proliferation) is reproduced for comparison as a dashed line on the middle and bottom left graphs.

Number of Dead/New Cells
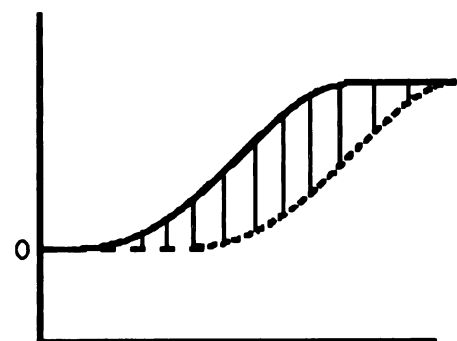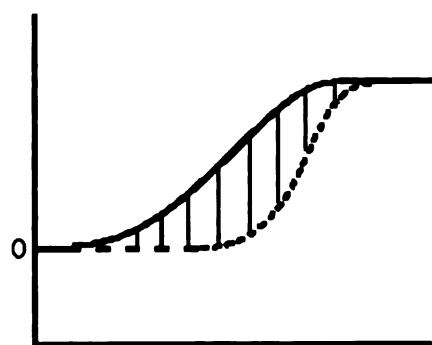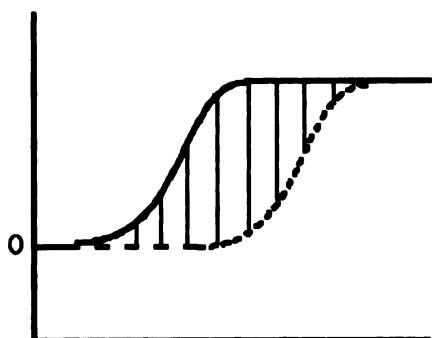
Focal Necrosis Size
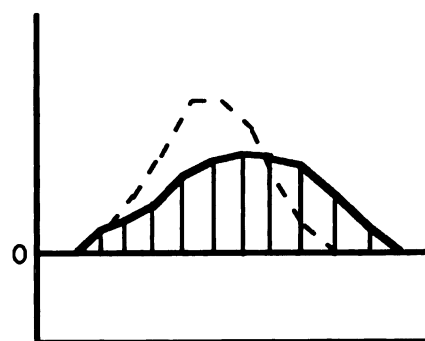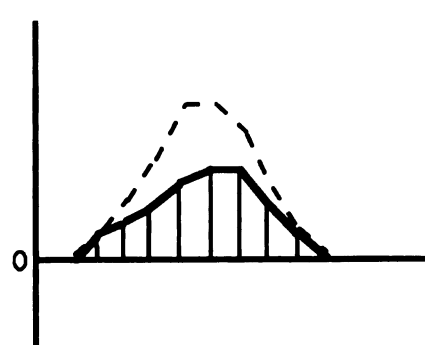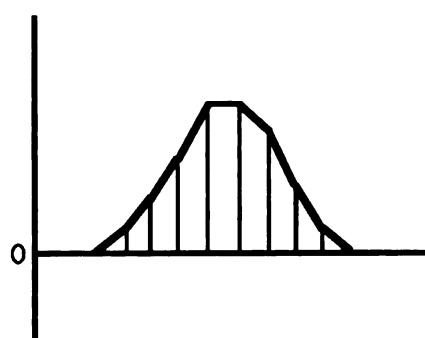
Time After Irradiation

CEREBROVASCULAR EFFECTS OF RADIATION

The results shown here are largely consistent with the hypothesis that radiation-induced alterations in cerebrovascular permeability lead to cerebral edema, which reduces blood flow in the edematous region and exacerbates radiation-induced necrosis. The relationship of permeability to edema is supported by the finding that focal irradiation resulted in a prolonged increase in BBB permeability, as evidenced by the continuous increase in K_i (Figure 18), and that the magnitude of K_i was strongly related to volume of edema. In addition, DFMO administration altered K_i and reduced the amount of edema.

The significant relationship between edema volume and blood flow in the tissue surrounding the focal lesion supports the contention that edema causes vascular compression and reduces blood flow, which may then lead to ischemic injury. The finding that the vascularity and blood flow were reduced in parallel (Figure 20) also supports this hypothesis. A possible criticism is that the relationship between edema, blood flow, and vascularity might be explained by a reduction in cell number per unit tissue volume due to excess tissue water. A corresponding decrease in vascularity, blood flow, and metabolic demand of the tissue would be expected to accompany the reduction in cell number per unit volume. If alterations in blood flow matched alterations in metabolic demand, there should not be any deleterious effects on the tissue. However, a wet/dry weight analysis demonstrated that tissue water within white matter and gray matter of the lesioned hemisphere was increased by approximately 10% and 5% at 2 and 4 weeks post-irradiation, respectively (data not shown). Reductions in blood flow and vascularity were larger and ranged from 10-20% at these times, indicating that the relationships between edema, blood flow, and vascularity can only partially be explained by changes in cell density and that the reduced blood flow reported here could potentially result in tissue injury.

Whether such reductions in blood flow truly lead to metabolic compromise (i.e. reduced ability to maintain ATP levels and continue normal cellular function) of the tissues requires further investigation. Measurement of tissue Na^+/K^+ ratios would provide a method of analyzing the metabolic state of the tissue; intracellular and tissue Na^+ tends to increase in the presence of metabolic deficits due to breakdown of the ATP-driven sodium-potassium pump.[119] Alternatively, quantitative nuclear magnetic resonance measurements of tissue Na^+ or ATP levels in the region of reduced blood flow, would provide a non-invasive and perhaps more appealing method to correlate changes in perfusion with possible metabolic deficits.

Edema volume and changes in vascularity proved to be significant factors in an ANOVA modelling alterations in mean transit time as a function of time after irradiation. The relationship of these two factors to mean transit time probably arises from the effects of edema on vascularity (i.e. vascular compression) and the effects of reduced vascularity on flow dynamics. Vascular compression increases resistance to flow through tissue, resulting in slower flow through existing vessels. However, this could then lead to a reduction in perfusion pressure and collapse of some capillaries, which would accentuate the reduced vascularity. Because of the relationship blood flow = vascularity/mean transit time (Equation 3), if the vascularity was reduced while blood flow remained constant, the mean transit time would necessarily have to increase. Thus, although vascular compression can potentially increase mean transit time, the effects may be lessened by accompanying vascular collapse. This would explain why changes in vascularity were more apparent than alterations in mean transit time (Figure 20).

There were no apparent *a priori* reasons to believe that K_i might be related to blood flow or mean transit time as was found in the present study.

One possible explanation for these relationships is that the increased K_i increased the blood-to-brain transfer of blood-borne vasoactive agents, such as serotonin and norepinephrine.[120] Such agents might then have acted to contract or relax smooth muscles of the vasculature, altered tissue resistance, and thereby altered both mean transit time and blood flow.

Although the BBB breakdown and cerebral edema appeared to reduce blood flow in tissues surrounding the focal lesion, it should be kept in mind that cells within these tissues, while appearing undamaged histologically, did receive substantial doses of radiation. The dose varied due to the rapid fall off in radiation as a function of distance from the source. Irradiation of vascular cells in these tissues may have contributed to the reduction in blood flow by modifying the ability of the cells to function physiologically without causing any cell loss. Although it is difficult to separate blood flow changes due to BBB breakdown and edema from changes due to cellular DNA damage, the time course of edema suggests one possible method of doing so. If the ability of the vasculature to function physiologically is truly altered, there might be accompanying alterations in the response of the vasculature to changes in arterial CO_2 tension or to vasodilatory drugs, such as acetazolamide.[121] Therefore, to separate the effects of edema on vascular function from those of DNA damage, the response of the vasculature to altered CO_2 could be tested prior to the onset of edema formation (i.e. <1 week Figure 16), at the point of maximum edema volume (i.e. 3-4 weeks), and after the resolution of edema (i.e. > 6 weeks). Alterations in vascular function occurring prior to edema formation or after the resolution of edema would be suggestive of effects due to radiation-induced DNA damage, and alterations occurring only at the point of maximum edema volume would suggest that the cerebrovascular changes were due to the radiation-induced edema.

DFMO-INDUCED MODIFICATIONS OF RADIATION INJURY

The alteration of radiation-induced brain injury by DFMO was presumably mediated by its modulation of polyamine levels, particularly Pu. There were elevated levels of putrescine in the CSF of saline treated animals at all time points following irradiation, whereas the putrescine levels in DFMO treated animals were depressed relative to baseline 1-2 weeks after irradiation (Figure 14). Furthermore, the polyamine levels of all tissue samples from saline treated animals were within the measurable range, whereas half of the samples from animals treated with DFMO were below detectable limits, suggesting that DFMO reduced putrescine levels in brain tissue as well as in CSF. Although the relationship between tissue and CSF putrescine levels is unclear, the data support the thesis that chronic intravenous infusion of DFMO can cause a generalized reduction in putrescine. At this time the precise role of putrescine in radiation-induced edema is not known, but other reports of focal brain injury have implicated this polyamine as an important biochemical correlate of morphologic cell damage[91] and as a mediator in disturbances of the BBB.[89, 92]

Because the CT method of measuring cerebral edema is not strictly dependent on the amount of tissue water (see Methodology, Validation, and Results - CT-Based Method Development and Validation: Cerebral Edema), there was concern that the DFMO-induced reduction of edema might reflect differences in some parameter besides water. For example, the CT method overestimated the amount of tissue water when compared to the wet/dry method. This indicates that the increase in tissue water could not fully account for the low CT number of the irradiated hemisphere. CT number of a tissue is determined by the CT number of its components, which are primarily water, protein, and lipid. Measurements of the standard phantom used in the present

study (Figure 2) demonstrate that the CT number of water and lipid are both lower than that of tissue, while protein is higher. Therefore, the only way to account for the overestimation of water content would appear to be that the increase in water was accompanied by an increase in lipid. This lipid could arise from breakdown of cellular membranes or products such as triglycerides leaking into the tissue across the damaged BBB. If there were differences in the amount of lipid within the irradiated hemispheres of the two groups, regression lines relating wet/dry water to CT measured water should be different for the two groups. However, an ANOVA did not detect any significant effect of DFMO on the relation between wet/dry and CT measured water, suggesting that the DFMO effect on edema is primarily attributable to differences in tissue water.

The clinical usefulness of DFMO in the treatment of cerebral edema remains to be determined. DFMO has been used to treat protozoal infections[122] and to inhibit cell proliferation in a variety of clinical situations, and, in general, it has been well tolerated.[123] But due to its cytostatic effects, it can have adverse effects, particularly in rapidly proliferating tissues such as the gut. In our study, some of the animals treated with DFMO developed gastrointestinal toxicity, including clinical dehydration, 1-2 days before the end of drug treatment. Brain edema measurements of those animals were in agreement with those obtained from animals showing no gastrointestinal symptoms, but there was concern that dehydration might adversely affect the brain water measurements. Furthermore, there was a possibility that the stress accompanying such symptoms could lead to the elevation of endogenous steroids, which could conceivably reduce brain water. However, the findings of the present study do not support a role for either of these factors in the observed effects of DFMO; there were no significant differences in the average brain

density (CT number) of the contralateral hemisphere, the serum hematocrit, or serum cortisol levels between the two treatment groups.

The reduction of edema by DFMO was probably mediated by the alteration of K_i by DFMO, as suggested by the significant relationship between edema and K_i mentioned earlier. The effect of DFMO on K_i is in general agreement with the study of Trout et al,[92] who demonstrated that DFMO could alter BBB permeability following focal cold-injury. However, changes in K_i alone could not account for all the alterations in edema volume attributed to DFMO and, in particular, the alteration seen 3 weeks after irradiation (Figure 16). Interestingly, K_b, the brain-to-blood transfer constant, was significantly elevated in the DFMO treated animals at that time (Figure 18), suggesting that the difference in edema at three weeks may involve faster backflux of materials from the brain into the blood rather than a slower blood-to-brain transfer. Likewise, the elevation of K_b in the saline treated group 6 weeks after irradiation might account for why edema volume was not increased at that time despite an increased K_i (Figures 16 and 18).

The effect of DFMO on contrast enhancement volume (Figure 17) is likely related to the effects of DFMO on K_i and V_P, as suggested by the ANOVA demonstrating a significant relationship between RE and those two factors. Contrast enhancement in the brain is generally considered to be a result of BBB breakdown,[124] but the data presented here demonstrate that it is also due to a change in vascular volume.

The morphologic basis of the DFMO-induced alteration in K_i is unknown at this point, but two possible explanations are related to the poly-cationic nature of polyamines. Polyamines may assist in the fusion of vesicles with cell membranes;[125] the positively charged amine groups on polyamines appear to neutralize the negatively-charged head groups of membrane lipids, allowing

two membranes to approach.[125] DFMO-mediated polyamine depletion might therefore inhibit transcellular vesicular transport, as reported following cold-injury,[92] by inhibiting membrane fusion. Alternatively, polyamine depletion might reduce the endothelial cell tight junction breakdown that is reported following brain injury.[126, 127] The intravenous administration of poly-lysine and protamine sulfate, both poly-cations, has been shown to increase BBB leakage and movement of horseradish peroxidase through cerebral endothelial tight junctions.[128, 129] Based on this finding, DFMO might reduce the degree of tight junction breakdown by reducing the tissue polyamine levels and thus reducing the level of a highly cationic species. However, the only explanation that is supported by data from the present study is linked to the relationship of K_i to V_P; both appeared to show a similar response over the 6 week post-irradiation period (Figure 18), and both were altered by DFMO. Since contrast leaks through openings in a damaged vascular wall, V_P determines the amount of leaky tissue and thereby is a factor in determining K_i. In addition, DFMO appears to lessen both the radiation-induced loss of vasculature (such as at 2 weeks - Figure 18) and the vascular response occurring at 6 weeks post-irradiation. Since BBB leakage in radiation-damaged brain is at least partly through dead or dying endothelial cells[76] and since new vessels within the brain appear to have increased BBB leakage,[130] both of these phenomena (i.e. reduced vascular loss and response) could account for the alteration in K_i.

The vascular volume was measured two different ways in the present study. The parameter termed "V_P" was measured during the assessment of K_i and K_b (Equation 2), and it is not really applicable to normal tissues in which there is no BBB breakdown (K_i and K_b are effectively zero). Therefore, V_P measured within the focal lesion could not be compared to any V_P measurement within normal, non-leaky tissue. The parameter which has been

termed "vascularity" in the present study was measured during the assessment of blood flow and mean transit time. Vascularity as well as blood flow and mean transit time were measured both within leaky and non-leaky tissue, which made it possible to evaluate changes in those parameters within the irradiated hemisphere relative to measurements within the contralateral hemisphere. Based upon these relative measurements (i.e. percent differences, Figures 19-22), with the possible exception of 3 weeks after irradiation in the DFMO group, both groups showed a reduction in blood flow within the focal lesion throughout the follow-up period (Figure 19). The initial reduction (1-2 weeks after irradiation) was probably due to loss of the vasculature through necrosis, as demonstrated by the reduction in vascularity and increase in necrosis during this time period. There were apparent differences between the DFMO and the saline treated group in the vascular response associated with this blood flow reduction. At 3 weeks, vascularity within lesion of the DFMO group was not reduced relative to the contralateral hemisphere, suggesting that there may have been either an ingrowth of new vessels or dilatation of existing vessels in the focal lesion at this time point. An ANOVA suggested ($p=0.0546$) that the vascularity in the saline control group was somewhat different, which agrees with the results from the analysis of V_P; not until 4 weeks did the vascularity within the lesion approach that of the opposite hemisphere, and the response at 6 weeks was over twice that of the DFMO group. Some of the vascular response at 6 weeks is clearly due to the ingrowth of new vessels, because there was histopathologic evidence of vessels within previously necrotic regions at this time point. Despite the increase in vascularity at 4-6 weeks, blood flow still appeared to be somewhat reduced at these times, which is accounted for by the increased mean transit time at these times (see Figure 19 and Equation 3). A similar phenomenon, in which increased mean transit time

corresponded to the time of increased vascularity, was seen following focal brain hyperthermia.[133] Interestingly, the cerebrovascular response was delayed following irradiation relative to the response following hyperthermia. The increase in vascularity following hyperthermia was apparent at 1-2 weeks post treatment, which compares to the increase at 3-6 weeks in the present study. These differences in the response are probably not related to differences in lesion size - the maximal size of the hyperthermia lesions were similar to the maximal size of the focal radiation lesions in the present study. The delayed response following irradiation is probably due to mitotic-linked death which may occur as endothelial cells divide in order to vascularize the necrotic area. The accelerated vascular response following hyperthermia made it possible to determine that mean transit time returns to normal when vascularity returns to normal.

The basis for the finding that the increase in vascularity was accompanied by an increase in mean transit time may be related to the immaturity of the new vessels. Following neovascularization of a tissue, there is a period during which there is a reduction in vascularity,[131] a process commonly referred to as maturation. New immature vessels may be redundant and/or tortuous, like those seen in tumors,[132] which should slow transit of blood through a region. The vessel loss accompanying neovascular maturation would reduce the variety of possible paths by which blood could cross a region and reduce the average path length of molecules traversing the region. Thus, vessel maturation would be accompanied by a reduction in mean transit time.

THEORIES CONCERNING THE DFMO-INDUCED EFFECTS

The results of the present study demonstrate that DFMO can modify many of the characteristics of radiation-induced brain injury. The fact that DFMO not only altered the degree of BBB breakdown but also altered of the magnitude of necrosis supports the contention that cerebrovascular permeability plays a significant role in the development of radiation-induced brain injury. However, it is important to keep in mind that the size of focal necrosis is dependent on at least three factors: the total amount of cell death, the rate of cell death, and the rate at which surviving cells proliferate to replace dead cells. A change in any of these could potentially alter the magnitude of focal necrosis. A hypothesis of the present work was that DFMO would reduce the magnitude of injury by diminishing the first factor - the total amount of cell death. The presumed mechanism was that altered cerebrovascular permeability would limit subsequent edema, vascular compromise, and degree of ischemia. While there were differences in the amount of edema between DFMO and saline treated groups, there were no differences between the groups with respect to blood flow changes in the tissue surrounding the focal lesion. This finding argues against the effect of DFMO on necrosis magnitude being mediated through a difference in the degree of ischemic injury. However, an alternative mechanism by which DFMO-mediated modification of cerebrovascular permeability might alter the amount of cell death and which is consistent with the present results is by reducing the movement of potentially harmful blood-borne materials, such as glutamate,[134] into the brain interstitium.

Both of the above proposed mechanisms to explain the effect of DFMO on necrosis depend upon the drug directly modifying permeability, either by changes in the amount of vesicular transport or the degree of tight junction breakdown. However, as discussed above, the data suggest that the DFMO-

mediated effect on permeability (or K_i) was more likely due to its effect on vascular volume rather than direct effects on vesicular transport or tight junctions. This suggests that the effect of DFMO on necrosis may not be secondary to the alterations in cerebrovascular permeability. Instead, alterations in cerebrovascular permeability may be secondary to DFMO-induced modifications of cell necrosis. DFMO could alter the evolution of radiation injury by altering the rate of mitotic-linked cell death. This suggestion is related to the thesis of Michalowski,[135] who has suggested that mitotic stimulation following irradiation of slowly proliferative tissues, such as nervous tissue, would be detrimental. At least some of the cell death occurring following focal irradiation should be attributable to mitotic-linked death, although the high doses near the seed probably produce interphase death. DFMO reduces the rate of cellular proliferation[136] and would likely slow the proliferative response of the cells which attempt to fill in the necrotic area resulting from interphase death (see Figures 25 and 26) This would delay the onset of mitosis of such cells and thus delay the onset of any mitotic-linked death. Such a scenario would result in a reduction of the maximal size of the lesion (Figure 27). This could account for the differences in the amount of necrosis and the differences in permeability and perhaps edema formation. If there was less vascular damage at any given time point due to a reduced loss of endothelial cells, the BBB breakdown would also be lessened. This would in turn lead to less leakage of plasma proteins, less of an osmotic gradient forcing the movement of water from blood into brain, and thus less cerebral edema. An additional mechanism by which a reduction in the rate of cell death might lessen the degree of cerebral edema is that slower cell death would result in a slower breakdown of cells. Osmolarity of the surrounding tissue would still increase due to release of breakdown products but at a slower rate. A slowed increase

in osmolarity would then slow the rate at which water would move from blood to brain. Thus, DFMO-induced slowing of the rate of cell proliferation might account for a number of the phenomena observed in the present set of experiments, such as reduced focal necrosis, altered permeability, and reduced edema. However, simply slowing the rate of mitotic-linked cell death should be accompanied by a slower rate of replacement with proliferating cells as well, so that there should be a delay in lesion resolution. While this appears to be consistent with the present data (Figure 15), preliminary experiments treating irradiated dogs with a dose of 75 mg/kg of DFMO also results in a reduction in the amount of necrosis but does not appear to slow the radiographic resolution.

Finally, the possibility that is most controversial yet most consistent with the present data is that DFMO directly alters the total number of cells that die. By delaying the onset of cell proliferation, DFMO might allow cells to better repair radiation-induced DNA damage. Although most findings have suggested that DFMO inhibits repair, as demonstrated by DFMO-induced inhibition of potentially lethal damage repair (PLDR),[137] others have suggested that DFMO may facilitate PLDR in some cell lines.[138] In addition, the phenomenon referred to as slow repair of radiation damage, which is reported to have a half-time of approximately 10 days in lung,[139] might be facilitated by the presence of DFMO. Decreasing the total number of cells that die could account for not only the alteration in the necrosis volume but also alterations in permeability (less vascular injury) and edema (less vascular injury and less osmotic changes due to cellular breakdown - see above).

FUTURE DIRECTIONS

There are a number of experiments that might allow one to determine if DFMO is altering radiation-induced injury via effects on vesicle formation, tight

junctions, rate of cell death, or cell survival. For example, histopathology demonstrated that the cellular changes of the focal lesion could range from frank coagulation necrosis to areas of interstitial edema and vascular proliferation to normal tissue over just a few millimeters. Based on this, it would probably be difficult to quantitatively distinguish effects of DFMO on cerebrovascular permeability based on ultrastructural features such as the amount of vesicular transport or degree of tight junction breakdown. However, such effects might be more easily distinguished using a simpler and more homogeneous system, such as an endothelial cell culture system. That system should make it possible to uniformly irradiate a homogeneous set of cells and quantify phenomena such as alterations in vesicular transport in the presence or absence of DFMO. This system has already been used to study the effects of irradiation +/- DFMO on the permeability of an endothelial cell monolayer.[95] Whether such a monolayer system would allow the study of radiation-induced change in tight junctions remains to be determined - the induction of tight junctions is dependent upon the presence of astrocytes, [140, 141] so that a co-culture of astrocytes and endothelial cells might be required for those studies. The co-culture of astrocytes and endothelial cells has been reported with some degree of success at inducing the formation of tight junctions.[140]

An approach to determining whether DFMO is altering the rate of mitotic-linked cell death was provided by Zeman and colleagues,[43] who used ^{3}H-thymidine to label proliferating cells in animals treated with spinal cord irradiation. They noted that animals sacrificed at longer times after labelling had a reduced number of ^{3}H-thymidine positive cells, which has been attributed to mitotic-linked death of some of the labelled cells.[42] It might be possible to quantify the amount of mitotic-linked death by determining the rate at which labelling decreased. Of course, at later times after labelling, proper corrections

would have to also be made for the increased amount of labelling resulting from successful division of ^{3}H-thymidine positive cells.

An *in vitro* cell culture system might make it possible to determine whether long-term DFMO administration (i.e. >48 hrs) alters radiation sensitivity of cell and thus alters the amount of cell death. In a preliminary experiment, rat glioma 9L cells were treated with 1 mM DFMO for 48 hours prior to and after irradiation with 4.0 Gy. Forty-eight hours after irradiation, the media was changed to a DFMO-free solution, and putrescine was added in order to replete polyamines in DFMO-treated cells. Cell colony formation was then assayed at 12 days after the media change. There was no significant difference in cell survival in the DFMO treated group, which might be attributed to the relatively high level of cell survival (approximately 10%). Drug effects on cell survival following irradiation are often times not evident until survival is reduced to 0.1-0.01%.[142] Therefore, the experiment needs to be repeated using higher radiation doses and perhaps longer DFMO exposures.

CONCLUSIONS

DFMO administration can diminish radiation-induced injury such as cerebral edema and perhaps focal necrosis. However, the modification of necrosis volume by DFMO does not appear to result from the modification of edema and an associated amelioration of blood flow deficits as was originally hypothesized. More likely, DFMO modification of permeability reduces tissue injury by decreasing the blood-to-brain movement of harmful blood-borne materials. Although effects of DFMO on repair of radiation-induced DNA damage may also play a part in the DFMO-mediated modification of radiation injury, the association of DFMO's effects on BBB breakdown with its effects on tissue necrosis strongly supports a role for cerebrovascular permeability in the

development of radiation-induced injury. This suggests that changes in the physiologic function of a tissue can play a significant role in the development of radiation damage. While many prior studies have concentrated on altering radiation injury via changes in cell radiosensitivity, the present study indicates that the modification of changes in physiologic function might provide an alternative means of treating radiation injury.

BIBLIOGRAPHY

1.   Leibel SA, Gutin PH, Wara WM, Silver P, Larson DA, Edwards MSB, Lamb SA, Ham B, Weaver KA, Barnett C, Phillips TL: Survival and quality of life after interstitial implantation of removable high-activity iodine-125 sources for the treatment of patients with recurrent malignant gliomas. *Int J Radiat Oncol Biol Phys* 1989; 17:1129-1139

2.   Gutin PH, Leibel SA, Wara WM, Choucair A, Levin VA, Phillips TL, Silver P, Da Silva V, Edwards MSB, Davis RL, Weaver KA, Lamb S: Recurrent malignant gliomas: survival following interstitial brachytherapy with high-activity iodine-125 sources. *J Neurosurg* 1987; 67:864-873

3.   Walker MD, Alexander E, Hunt WE, MacCarty CS, Mahaley MS, Mealey J, Norrell HA, Owens G, Ransohoff J, Wilson CB, Gehan EA, Strike TA: Evaluation of BCNU and/or radiotherapy in the treatment of anaplastic gliomas. *J Neurosurg* 1978; 49:333-343

4.   Walker MD, Strike TA, Sheline GE: An analysis of dose-effect relationship in the radiotherapy of malignant gliomas. *Int J Radiat Oncol Biol Phys* 1979; 5:1725-1731

5.   Sheline GE, Wara WM, Smith V: Therapeutic irradiation and brain injury. *Int J Radiat Oncol Biol Phys* 1980; 6:1215-1228

6.   Gutin PH, Leibel SA: Stereotaxic interstitial brachytherapy for malignant brain tumors, in Withers HR, Peters LJ (eds): *Medical Radiology Innovations in Radiation Oncology.* Berlin, Springer-Verlag, 1988, pp 167-174

7.   Gutin PH: Corticosteroid therapy in patients with cerebral tumors: Benefits, mechanisms, problems, practicalities. *Semin Oncol* 1975; 2:49-56

8.   Haynes RC, Larner J: Adrenocorticotropic hormone; adrenocortical steroids and their synthetic analogs; inhibitors of adrenocortical steroid biosynthesis, in Goodman LS, Gilman A (eds): *The Pharamacological Basis of Therapeutics.* New York, MacMillan Publishing Co., Inc., 1975, pp 1472-1506

9.   Bagg HJ: The effect of radium emanation on the adult mammalian brain. An experimental study upon animals, with special reference to the therapeutic dose in the treatment of brain tumor. *Am J Roentgenol* 1921; 8:536-547

10.   Horsley V, Finzi NS: The action of filtered radium rays when applied directly to the brain. *Br Med J* 1911; 2:898-899

11.   Williamson CS, Brown RO, Butler JW: A study of the effects of radium on normal brain tissue. *Surg Gynecol Obstet* 1920; 31:239-242

12.   Alpers BJ, Pancoast HK: The effect of irradiation of normal and neoplastic brain tissue. *Am J Cancer* 1933; 17:7-24

13.   Davidoff LM, Dyke CG, Elsberg CA, Tarlov IM: The effect of radiation applied directly to the brain and spinal cord. I. Experimental investigations on Macacus Rhesus monkeys. *Radiology* 1938; 31:451-463

14.   Lyman RS, Kupalov PS, Scholz W: Effect of roentgen rays on the central nervous system. Results of large doses on the brain of adult dogs. *Arch Neurol Psychiat* 1933; 29:57-87

15.   Scholz W, Hsü YK: Late damage from roentgen irradiation of the human brain. *Arch Neurol Psychiat* 1938; 40:928-936

16.   Ross JP: The treatment of cerebral tumours with radium. *Br J Surg* 1931; 18:618-635

17.   Hopewell JW, Campling D, Calvo W, Reinhold HS, Wilkinson JH, Yeung TK: Vascular irradiation damage: its cellular basis and likely consequences. *Br J Cancer* 1986; 53, Suppl. VII:181-191

18.   Withers HR, Peters LJ, Kogelnik HD: The pathobiology of late effects of irradiation, in Meyn R, Withers HR (eds): *Radiation Biology in Cancer Research*. New York, Raven Press, 1980, pp 439-448

19.   Korr H, Schultze B, Maurer W: Autoradiographic investigations of glial proliferation in the brain of adult mice. II. Cycle time and mode of proliferation in neuroglia and endothelial cells. *J Comp Neurol* 1975; 160:477

20.   Schultze B, Korr H: Cell kinetic studies of different cell types in the developing and adult brain of the rat and mouse: a review. *Cell Tissue Kinet* 1981; 14:309-325

21.   Hobson B, Denekamp J: Endothelial proliferation in tumours and normal tissues: continuous labeling studies. *Br J Cancer* 1984; 49:405-413

22.   Arnold A, Bailey P: Alterations in the glial cells following irradiation of the brain in primates. *Arch Pathol* 1954; 57:383-391

23.   Arnold A, Bailey P, Harvey RA, Haas LL, Laughlin JS: Changes in the central nervous system following irradiation with 23-mev x-rays from the betatron. *Radiology* 1954; 62:37-44

24.   Vogel FS, Pickering JE: Demyelinization induced in the brains of monkeys by means of fast neutrons: pathogenesis of the lesion and comparison with the lesions of multiple sclerosis and Schilder's disease. *J Exp Med* 1956; 104:435-442

25.   Wachowski TJ, Chenault H: Degenerative effects of large doses of roentgen rays on human brain. *Radiology* 1945; 45:227-246

26.   O'Connell JEA, Brunschwig A: Observations on the roentgen treatment of intracranial gliomata with especial reference to the effects of irradiation upon the surrounding brain. *Brain* 1937; 6:230-258

27.   Zeman W, Samorajski T: Effects of irradiation on the nervous system, in Berdjis CC (eds): *Pathology of Irradiation*. Baltimore, Williams & Wilkins, 1971, pp 213-277

28.   Gross PM, Sposito NM, Pettersen SE, Fenstermacher JD: Differences in function and structure of the capillary endothelium in gray matter, white matter and a circumventricular organ of rat brain. *Blood Vessels* 1986; 23:261-270

29.   Calvo W, Hopewell JW, Reinhold HS, Yeung TK: Time- and dose-related changes in the white matter of the rat brain after single doses of X rays. *Br J Radiol* 1988; 61:1043-1052

30.   Rose RG: The influence of ionizing radiations on the penetration of sodium into the central nervous system. *Int J Appl Radiat Isotopes* 1958; 4:50-57

31.   Myers R, Rogers MA, Hornsey S: A reappraisal of the roles of glial and vascular elements in the development of white matter necrosis in irradiated rat spinal cord. *Br J Cancer* 1986; 53 Suppl. VII:221-223

32.   Blakemore WF, Patterson RC: Suppression of remyelination in the CNS by X-irradiation. *Acta Neuropathol (Berl)* 1978; 42:105-113

33.   van der Kogel AJ: Radiation-induced damage in the central nervous system: An interpretation of target cell responses. *Br J Cancer* 1986; 53:207-217

34.   Delattre JY, Rosenblum MK, Thaler HT, Mandell L, Shapiro WR, Posner JB: A model of radiation myelopathy in the rat: pathology, regional capillary permeability changes and treatment with dexamethasone. *Brain* 1988; 111:1319-1336

35.   Clemente CD, Holst EA: Pathological changes in neurons, neuroglia and blood-brain barrier induced by x-irradiation of heads of monkeys. *Arch Neurol Psych* 1954; 71:66-79

36.   Ascher AW, Anson SG: Arterial hypertension and irradiation damage to the nervous system. *Lancet* 1962; 2:1343-1346

37.   Hopewell JW, Wright EA: The nature of latent cerebral irradiation damage and it modification by hypertension. *Br J Radiol* 1970; 43:161-167

38.   Michalowski A, Wheldon TE, Kirk J: Can cell survival parameters be deduced from non-clonogenic assays of radiation damage to normal tissues? *Br J Cancer* 1984; 49, Suppl. VI:257-261

39.   Wheldon TE, Michalowski AS, Kirk J: The effect of irradiation on function in self-renewing normal tissues with differing proliferative organisation. *Br J Radiol* 1982; 55:759-766

40.   van der Kogel AJ: Central nervous system radiation injury in small animal models, in Gutin PH, Leibel SA, Sheline GE (eds): *Radiation Injury to the Nervous System.* New York, Raven Press, 1991 , pp 91-112

41.   Hornsey S, Myers R, Coultas PG, Rogers MA, White A: Turnover of proliferative cells in the spinal cord after X irradiation and its relation to time-dependent repair of radiation damage. *Br J Radiol* 1981; 1081-1085

42.   Hubbard BM, Hopewell JW: Changes in the neuroglial cell populations of the rat spinal cord after local x-irradiation. *Br J Radiol* 1979; 52:816-822

43.   Zeman W: Disturbances of nucleic acid metabolism preceding delayed radionecrosis of nervous tissue. *Proc Natl Acad Sci USA* 1963; 50:626-630

44.   Blakemore WF, Palmer AC: Delayed infarction of spinal cord white matter following x-irradiation. *J Pathol* 1982; 137:273-280

45.   Feigin I: Sequence of pathological changes in brain edema, in Klatzo I, Seitelberger F (eds): *Brain Edema.* New York, Springer, 1967, pp 128-151

46.   Janzer RC, Kleihues P, Ostertag CB: Early and late effects on the normal dog brain of permanent interstitial iridium-192 irradiation. *Acta Neuropathol (Berl)* 1986; 70:91-102

47.   Groothuis DR, Wright DC, Ostertag CB: The effect of ^{125}I interstitial radiotherapy on blood-brain barrier function in normal canine brain. *J Neurosurg* 1987; 67:895-902

48.   Joó F, Szücs A, Csanda E: Metiamide-treatment of brain oedema in animals exposed to [90]yttrium irradiation. *J Pharm Pharmacol* 1976; 28:162-163

49.   Lo EH, Frankel KA, Delapaz RL, Poljak A, Woodruff KH, Brennan KM, Phillips MH, Valk PE, Steinberg GK, Fabrikant JI: Cerebrovascular and metabolic perturbations in delayed heavy charged particle radiation injury. *Brain Res* 1989; 504:168-172

50.   Tanaka A, Ueno H, Yamashita Y, Caveness WF: Regional cerebral blood flow in delayed brain swelling following x-irradiation of the right occipital lobe in the monkey. *Brain Res* 1975; 96:233-246

51.   Warnke PC, Hans FJ, Wagner S, Ostertag CB: *The effect of dexamethasone on capillary permeability and rCBF in radiation induced brain edema.* Eighth International Symposium on Brain Edema, 1990, Bern, Switzerland. p 158

52.   Turowski K Fike, J.R., Cann, C.E., Higgins, R.J., Davis, R.L., Gutin, P.H., Phillips, T.L., Weaver, K.A.: Normal brain iodine-125 radiation damage: Effect of dose and irradiated volume in a canine model. *Radiology* 1986; 158:833-838

53.   Blasberg RG, Fenstermacher JD, Patlak CS: Transport of alpha-aminoisobutyric acid across brain capillary and cellular membranes. *J Cereb Blood Flow Metab* 1983; 3:8-32

54.   Csanda E: Radiation Brain Edema, in Cervós-Navarro J, Ferszt R (eds): *Advances in Neurology.* New York, Raven Press, 1980, pp 125-146

55.   Fike JR, Cann CE, Turowski K, Higgins RJ, Chan ASL, Phillips TL, Davis RL: Radiation dose response of normal brain. *Int J Radiat Oncol Biol Phys* 1988; 14:63-70

56.   Lacombe P, Meric P, Seylaz J: Validity of cerebral blood flow measurements obtained with quantitative tracer techniques. *Brain Res* 1980; 203:105-169

57.   Berg NO, Lindgren M: Time-dose relationship and morphology of delayed radiation lesions of the brain in rabbits. *Acta Radiol* 1958; Suppl 167:1-118

58.   Fike JR, Cann CE, Phillips TL, Bernstein M, Gutin PH, Turowski K, Weaver KA, Davis RL, Higgins RJ, DaSilva V: Radiation brain damage induced by interstitial 125-I sources: A canine model evaluated by quantitative computed tomography. *Neurosurg* 1985; 16:530-537

59.   Gobbel GT, Cann CE, Iwamoto HS, Fike JR: Measurement of regional cerebral blood flow using ultrafast computed tomography: Experimental validation. *Stroke* In Press

60.   Gobbel GT, Cann CE, Fike JR: Measurement of regional cerebral blood flow using ultrafast computed tomography: Theoretical aspects. *Stroke* In Press

61.   Iannotti F, Fieschi C, Alfano B, Picozzi P, Punzo A, Del Vecchio G, Lenzi G, Salvatore M, Conforti P: Simplified, noninvasive PET measurement of blood-brain barrier permeability. *J Comput Assist Tomogr* 1987; 11:390-397

62. Hellman RS, Tikofsky RS: An overview of the contribution of regional cerebral blood flow studies in cerebrovascular disease: is there a role for single photon emission computed tomography. *Semin Nucl Med* 1990; 20:303-324

63. Phelps ME, Hoffman EJ, Mullani NA, Ter-Pogossian MM: Application of annihilation coincidence detection of transaxial reconstruction tomography. *J Nucl Med* 1975; 16:210-224

64. Kuhl DE, Barrio JR, Huang SC, Selin C, Ackermann RF, Lear JL, Wu JL, Lin TH, Phelps ME: Quantifying local cerebral blood flow by N-isopropyl-p-[^{123}I]iodoamphetamine (IMP) tomography. *J Nucl Med* 1981; 23:196-203

65. Valk PE: *Personal Communication* 1990

66. Haymaker W, Laquer G, Nauta WJH, Pickering JE, Sloper JC, Vogel FS: The effects of barium^{149}-lanthanum^{140} [gamma] radiation on the central nervous system and pituitary gland of macaque monkeys. *J Neuropath Exp Neurol* 1958; 17:12-57

67. Russell DS, Wilson CW, Tansley K: Experimental radionecrosis of the brain in rabbits. *J Neurol Neurosurg Psychiat* 1949; 12:187-195

68. Barranco D, Sutton LN, Florin S, Greenberg J, Sinnwell T, Ligeti L, McLaughlin AC: Use of ^{19}F NMR spectroscopy for measurement of cerebral blood flow: a comparative study using microspheres. *J Cereb Blood Flow Metabol* 1989; 9:886-891

69.   Ewing JR, Branch CA, Helpern JA, Smith MB, Butt SM, Welch KMA: Cerebral blood flow measured by NMR indicator dilution in cats. *Stroke* 1989; 20:259-267

70.   Hayakawa K, Yamashita K, Mitsumori M, Nakano Y: Blood-brain barrier injury following intracarotid injection of radiographic contrast media: *in vivo* quantification using magnetic resonance imaging and Gd-DTPA. *Acta Radiol* 1990; 31:203-208

71.   Le Bihan D, Breton E, Lallemand D, Grenier P, Cabanis E, Laval-Jeantet M: MR imaging of intravoxel incoherent motions: application to diffusion and perfusion in neurologic disorders. *Radiology* 1986; 161:401-407

72.   Le Bihan D, Breton E, Lallemand D, Aubin M, Vignaud J, Laval-Jeantet M: Separation of diffusion and perfusion in intravoxel incoherent motion MR imaging. *Radiology* 1988; 168:497-505

73.   Rosen BR, Belliveau HW, Betteridge D, Cohen MS, Weisskoff RM, Vevea JM, Rzedzian RP, Brady TJ: Perfusion imaging with magnetic-susceptibility contrast media: real-time MR imaging. *Radiology* 1989; 173P:383

74.   Seiderer M, Krappel W, Moser E, Hahn D, Schmmeidek PB, Kirsch C, Lissner J: Detection and quantification of chronic cerebrovascular disease: comparison of MR imaging, SPECT, and CT. *Radiology* 1989; 170:545-548

75.   Young IR, Bydder GM, Payne JA: Flow measurement by the development of phase differences during slice formation in MR imaging. *Magn Reson Med* 1986; 3:175-179

76.   Bernstein M, Marotta T, Stewart P, Glen J, Resch L, Henkelman M: Brain damage from ^{125}I brachytherapy evaluated by MR imaging, a blood-brain barrier tracer, and light and electron microscopy in a rat model. *J Neurosurg* 1990; 73:585-593

77.   Grossman RI, Hecht-Leavitt CM, Evans SM, Lenkinski RE, Holland GA, Van Winkle TJ, McGrath JT, Curran WJ, Shetty A, Joseph PM: Experimental radiation injury: combined MR imaging and spectroscopy. *Radiology* 1988; 169:305-309

78.   Hendrick RE: Image contrast and noise, in Stark DD, Bradley WG (eds): *Magnetic Resonance Imaging.* St. Louis, C.V. Mosby, 1988, pp 66-83

79.   Jaschke W, Gould RG, Assimakopoulos PA, Lipton MJ: Flow measurements with a high-speed computed tomography scanner. *Med Phys* 1987; 14:238-243

80.   Jaschke W, Lipton MJ, Boyd D, Moss AA, Cann C, Goldberg HI, Margulis AR, Sievers R: Dynamic CT scanning of the normal canine liver: interpretation of time density curves resulting from an intravenous bolus injection of contrast material. *Eur J Radiol* 1985; 5:256-260

81. Jaschke WR, Gould RG, Cogan MG, Sievers R, Lipton MJ: Cine-CT measurement of cortical renal blood flow. *J Comput Assist Tomogr* 1987; 11:779-784

82. Gould RG, Lipton MJ, McNamara MT, Sievers RE, Koshold S, Higgins CB: Measurement of regional myocardial blood flow in dogs by ultrafast CT. *Invest Radiol* 1988; 23:348-353

83. Yonas H, Gur D, Latchaw R, Wolfson SK: Stable xenon CT/CBF imaging: laboratory and clinical experience. *Adv Tech Stand Neurosurg* 1987; 15:3-37

84. Axel L: Cerebral blood flow determination by rapid-sequence computed tomography: a theoretical analysis. *Radiology* 1980; 137:679-686

85. Hopper JL, Davis SM, Tress BM, Kaye AH, Rossiter SC, Derrick PL: Analysis of dynamic computed tomography scan brain images. *Invest Radiol* 1987; 22:651-657

86. Norman D, Axel L, Berninger WH, Edwards MS, Cann CE, Redington RW, Cox L: Dynamic computed tomography of the brain: techniques, data analysis, and applications. *Am J Roentgenol* 1981; 136:759-770

87. Haimson J: X-ray source without moving parts for ultra-high speed tomography. *IEEE Trans Nucl Sci* 1979; 26:2857-2861

88. Dempsey RJ, Roy MW, Meyer K, Meyer TH, Olson JW: Polyamine and prostaglandin markers in focal cerebral ischemia. *Neurosurg* 1985; 17:635-640

89.   Koenig H, Goldstone AD, Lu CY: Blood brain barrier breakdown in brain edema following cold injury is mediated by microvascular polyamines. *Biochem Biophys Res Commun* 1983; 55:1039-1048

90.   Koenig H, Goldstone AD, Lu CY: Blood-brain barrier breakdown in cold-injured brain is linked to a biphasic stimulation of ornithine decarboxylase activity and polyamine synthesis: both are coordinately inhibited by verapamil, dexamethasone, and aspirin. *J Neurochem* 1989; 52:101-109

91.   Paschen W, Schmidt-Kastner R, Hallmayer J, Djuricic B: Polyamines in cerebral ischemia. *Neurochem Pathol* 1988; 9:1-20

92.   Trout JJ, Koenig H, Goldstone AD, Lu CY: Blood-brain barrier breakdown by cold injury - polyamine signals mediate acute stimulation of endocytosis, vesicular transport, and microvillus formation in rat cerebral capillaries. *Lab Invest* 1986; 55:622-631

93.   Pegg AE: Polyamine metabolism and its importance in neoplastic growth and as a target for chemotherapy. *Cancer Res* 1988; 48:759-774

94.   Schmitz MP, Combs DJ, Dempsey RJ: Difluoromethylornithine inhibition of polyamine pathway synthesis decreases postischemic edema and blood-brain barrier breakdown. *Neurosurg* 1989; 24:943

95. Friedman M, Strickland DL, Chaney EL, Kwock L: α-difluoromethylornithine (DFMO) protects pulmonary endothelium *in vitro* from injury caused by ionizing radiation. *Am Rev Resp Dis* 1986; 133:A268

96. Brooks RA, Di Chiro G: Beam-hardening in x-ray reconstructive tomography. *Phys Med Biol* 1976; 21:390-398

97. Putlan BR, Ritchings RT, Isherwood I: Accuracy and meaning of computed tomography attenuation values, in Newton TH, Potts DG (eds): *Radiology of the Skull and Brain.* St. Louis, Mosby, 1981, pp 3904-3917

98. Reiderer SJ, Pelc NJ, Chesler DA: The noise power spectrum in computed x-ray tomography. *Phys Med Biol* 1978; 23:446-454

99. Glover GH, Pelc NJ: Nonlinear partial volume artifacts in x-ray computed tomography. *Med Phys* 1980; 7:238-248

100. Kaufman L, Deconinck RF, Price DC, Guersry P, Wilson CJ, Hruska B, Swann SJ, Camp DC, Voegele AL, Friesen RD, Nelson JA: An automated fluorescent excitation analysis system for medical applications. *Invest Radiol* 1976; 137:679-686

101. Fike JR, Cann CE, Berninger WH: Quantitative evaluation of the canine brain using computed tomography. *J Comput Assist Tomogr* 1982; 6:325-333

102. Fike JR, Cann CE, Davis RL, Borcich JK, Phillips TL, Russell LB: Computed tomography analysis of the canine brain: effects of hemibrain x irradiation. *Radiat Res* 1984; 99:294-310

103. Iwamoto HS, Kaufman T, Keil LC, Rudolph AM: Responses to acute hypoxemia in fetal sheep at 0.6-0.7 gestation. *Am J Physiol* 1989; 256:H613-H620

104. Devore J: *Probability and Statistics for Engineering and the Sciences* Monterey, California, Brooks/Cole Publishing Company, 1987, pp 672

105. Dole WP, Jackson DL, Rosenblatt JI, Thompson WL: Relative error and variability in blood flow measurements with radiolabeled microspheres. *Am J Physiol* 1982; 243:H371-H378

106. Press WH, Flannery BP, Teukolsky SA, Vetterling WT: *Numerical Recipes in Pascal: The Art of Scientific Computing* New York, Cambridge University Press, 1989, pp 759

107. Hilal SK: Hemodynamic changes associated with the intra-arterial injection of contrast media. *Radiology* 1966; 86:615-633

108. Lardani H, Rinaldi G, Cingolani H: Effects of angiographic contrast medium on isolated canine coronary arteries. *Am J Cardiol* 1982; 50:869-873

109. Schmidek H, Moreira D, Harder D: Diatrizoate meglumine-induced dilation of rat basilar artery: an *in vitro* study. *Neurosurg* 1983; 12:137-141

110.   Podreka I, Baumgartner C, Suess E, Müller C, Brücke T, Lang W, Holzner F, Steiner M, Deecke L: Quantification of regional cerebral blood flow with IMP-SPECT: reproducibility and clinical relevance of flow values. *Stroke* 1989; 20:183-191

111.   Yonas H, Wolfson SK, Gur D, Latchaw RE, Good WF, Leanza R, Jackson DL, Jannetta PJ, Reinmuth OM: Clinical experience with the use of xenon-enhanced CT blood flow mapping in cerebral vascular disease. *Stroke* 1984; 15:443-450

112.   Kabra PM, Lee HK, Lubich WP, Marton LJ: Solid-phase extraction and determination of dansyl derivatives of unconjugated and acetylated polyamines by reverse phase liquid chromatography: improved separation systems for polyamines in cerebrospinal fluid, urine and tissue. *J Chromatogr Biomed Appl* 1986; 380:19-32

113.   Kuroiwa T, Seida M, Tomida S, Hiratsuka H, Okeda R, Inaba Y: Discrepancies among CT, histological and blood-brain barrier findings in early cerebral ischemia. *J Neurosurg* 1986; 65:517-524

114.   Matsuoka Y, Hossman K-A: Brain tissue osmolality after middle cerebral artery occlusion in cats. *Exp Neurol* 1982; 599-611

115.   Tornheim PA, McLaurin RL: Effects of mechanical impact to the skull on tissue density of the cerebral cortex, in *Recent Progress in the Study and Therapy of Brain Edema.* New York, Plenum Press, 1984, pp 81-92

116. Hall EJ: *Radiobiology for the Radiologist* (3rd ed.). Philadelphia, Lippincott, 1988, pp 535

117. Leibel SA, Sheline GE: Tolerance of the central and peripheral nervous system to therapeutic irradiation, in Lett JT, Altman KI, Ehmann UK, Cox AB (eds): *Advances in Radiation Biology.* New York, Academic Press, 1987, pp 257-288

118. Kuroiwa T, Cahn R, Juhler M, Goping G, Capbell G, Klatzo I: Role of extracellular proteins in the dynamics of vasogenic brain edema. *Acta Neuropathol (Berl)* 1985; 66:3-11

119. Chan PH, Fishman RA: Brain Edema, in Lajtha A (eds): *Handbook of Neurochemistry.* New York, Plenum Publishing Corporation, 1985, pp 153-174

120. Owman C, Hardebo JE: Experimental opening of the blood-brain barrier affects cerebral blood flow and alters flow response to circulating transmitter amines and peptides, in Johansson BB, Owman C, Widner H (eds): *Pathophysiology of the blood-brain barrier.* New York, Elsevier, 1990, pp 113-130

121. Rogg J, Rutigliano M, Yonas H, Johnson DW, Pentheny S, Latchaw RE: The acetazolamide challenge: imaging techniques designed to evaluate cerebral blood flow reserve. *Am J Roentgenol* 1989; 153:605-612

122. Sjoedsma A, Schechter PJ: Chemotherapeutic implications of polyamine biosynthesis inhibition. *Clin Pharmacol Ther* 1984; 35:287-300

123. Griffin CA, Slavik M, Chien SC, Hermann J, Thompson G, Blanc O, Luk GD, Baylin SB, Abeloff MD: Phase I trial and pharmacokinetic study of intravenous and oral α-difluoromethylornithine. *Invest New Drugs* 1987; 5:177-186

124. Zagzag D, Goldenberg M, Brem S: Angiogenesis and blood-brain barrier breakdown modulate CT contrast enhancement: an experimental study in a rabbit brain-tumor model. *Am J Neuroradiol* 1988; 10:529-534

125. Hong K, Schuber F, Papahadjopoulos D: Polyamines: biological modulators of membrane fusion. *Biochim Biophys Acta* 1983; 732:469-472

126. Olsson Y, Klatzo I, Carsten A: The effect of acute radiation injury on the permeability and ultrastructure of intracerebral capillaries. *Neuropath Appl Neurobiol* 1975; 1:59-68

127. Cervos-Navarro J, Mrsulija BJ: Morphofunctional aspects of the normal and pathological blood-brain barrier. *Acta Neuropath (Berl)* 1983; Suppl. VIII:1-19

128. Nagy Z, Peters H, Hüttner I: Charge-related alterations of the cerebral endothelium. *Lab Invest* 1983; 49:662-671

129.   Needham L, Hellewell PG, Williams TJ, Gordon JL: Endothelial functional responses and increased vascular permeability induced by polycations. *Lab Invest* 1988; 59:538-548

130.   Liu H: Neovasculature and blood-brain barrier in ischemic brain infarct. *Acta Neuropathol (Berl)* 1988; 75:422-426

131.   Connolly SE, Hores TA, Smith LEH, D'Amore PA: Characterization of vascular development in the mouse retina. *Microvasc Res* 1988; 36:275-290

132.   Orita T, Nishizaki T, Aoki H, Harada K, Okamura T: The microvascular architecture of human malignant glioma: a scanning electron microscopic study of a vascular cast. *Act Neuropath (Berl)* 1988; 76:270-274

133.   Fike JR, Gobbel GT, Satoh T, Stauffer PR: Normal brain response after interstitial microwave hyperthermia. *Int J Hyperthermia* In Press

134.   Johansson BB, Nordborg C, Westergren I: Neuronal injury after a transient opening of the blood-brain barrier: modifying factors, in Johansson BB, Owman C, Widner H (eds): *Pathophysiology of the blood-brain barrier.* New York, Elsevier, 1990, pp 145-157

135.   Michalowski A: On radiation damage to normal tissues and its treatment I. growth factors. *Acta Oncol* 1990; 29:1017-1023

136.   Tabor CW, Tabor H: Polyamines. *Annu Rev Biochem* 1984; 53:749-790

137. Gerner EW, Tome ME, Fry SE, Bowden GT: Inhibition of ionizing radiation recovery processes in polyamine-depleted Chinese hamster cells. *Radiat Res* 1988; 48:4881-4885

138. Stea B, Stringer DE, Cress AE, Gerner EW: *Polyamine-dependent radiation responses of human tumor cells.* 37th Annual Meeting of the Radiation Research Society, 1990, New Orleans, Louisiana. p 152

139. Hornsey S, Field SB: Slow repair and residual injury, in Meyn R, Withers HR (eds): *Radiation Biology in Cancer Research.* New York, Raven Press, 1980, pp 489-499

140. Arthur FE, Shivers RR, Bowman PD: Astrocyte-mediated induction of tight junctions in brain capillary endothelium: an efficient *in vitro* model. *Brain Res Dev Brain Res* 1987; 36:155-159

141. Goldstein GW: Endothelial cell-astrocyte interactions: a cellular model of the blood-brain barrier. *Ann NY Acad Sci* 1988; 529:31-39

142. Teicher BA, Herman TS, Kaufmann ME: Cytotoxicity, radiosensitization, and DNA interaction of platinum complexes of thiazin and xanthene dyes. *Radiat Res* 1990; 121:187-195

143. Dean PB, Kivisaari L, Kormano M: The diagnostic potential of contrast enhancement pharmacokinetics. *Invest Radiol* 1978; 13:533-540

144. Gibson JG, Seligman AM, Peacock WC, Aub JC, Fine J, Evans RD: The distribution of red cells and plasma in large and minute vessels of the normal dog, determined by radioactive isotopes of iron and iodine. *J Clin Invest* 1946; 25:848-857

145. Mullani NA, Gould KL: First-pass measurements of regional blood flow with external detectors. *J Nucl Med* 1983; 24:577-581

146. Zierler KL: Theoretical basis of indicator-dilution methods for measuring flow and volume. *Circ Res* 1962; 10:393-407

147. Zierler KL: Equations for measuring blood flow by external monitoring of radioisotopes. *Circ Res* 1965; 16:309-321

148. Thompson HK, Starmer F, Whalen RE, McIntosh HD: Indicator transit time considered as a gamma variate. *Circ Res* 1964; 14:502-515

149. Bracewell R: *The Fourier Transform and Its Applications* (2nd ed.). San Francisco, McGraw-Hill, 1986, pp 474

150. Bassingthwaighte J, Ackerman F, Wood E: Applications of the lagged normal density curve as a model for arterial dilution curves. *Circ Res* 1966; 18:398-415

151. Dawson CA, Capen RL, Latham LP, Hanson WL, Hofmeister SE, Bronikowski TA, Rickaby DA, Wagner WW: Pulmonary arterial transit times. *J Appl Physiol* 1987; 63:770-777

152. Carlsen O, Hedegaard O: Evaluation of regional cerebral circulation based on absolute mean transit times in radionuclide cerebral angiography. *Phys Med Biol* 1987; 32:1457-1467

153. Phelps ME, Kuhl DE: Pitfalls in the measurement of cerebral blood volume with computed tomography. *Radiology* 1976; 121:375-377

154. Bäck SE, Krutzén E, Nilsson-Ehle P: Contrast media as markers for glomerular filtration: a pharmacokinetic comparison of four agents. *Scand J. Clin Lab Invest* 1988; 48:247-253

155. Welling PG: *Pharmacokinetics Processes and Mathematics* Washington, D.C., American Chemical Society, 1986, pp 218-221

156. Bernstein M, Gutin PH, Weaver KA, Deen DF, Barcellos MH: [125]I interstitial implants in the rif-1 murine flank tumor: an animal model for brachytherapy. *Radiat Res* 1982; 91:624-637

157. Krishnaswamy V: Dose distribution around an ^{125}I seed source in tissue. *Radiology* 1978; 128:489-491

APPENDIX

I. GENERAL ANESTHESIA

1. Atropine sulfate (0.05 mg kg^{-1}) and acepromazine (0.25 mg kg^{-1}) were administered subcutaneously 10-20 minutes before induction of general anesthesia.

2. After clipping the hair overlying the left or right cephalic vein, the region was swabbed with alcohol and an 18-20 g intravenous catheter was inserted into the vein and taped in position.

3. The catheter was flushed with 1-2 ml of normal saline.

4. Three to four ml of 4% sodium thiamylal was slowly infused into the intravenous catheter. This was supplemented with 1 ml boluses of thiamylal in order to induce a surgical plane of anesthesia (i.e. reduced palpebral and pedal reflexes and minimal jaw muscle tone).

5. An endotracheal tube was inserted, the cuff of the tube inflated, and the tube tied in place using a gauze sponge placed around the tube and either the mandible or maxilla.

6. A surgical plane of anesthesia was maintained with either supplemental 1 ml boluses of thiamylal or a combination of O_2 (1 l·min^{-1}) and methoxyflurane gas.

II. MEASUREMENT OF EDEMA VOLUME USING CT

The CT number of a region, CT_{ROI}, comprised of two materials of known atomic composition is closely approximated by a linear combination of the CT numbers of each material, CT_1 and CT_2, within the region such that

$$CT_{ROI} \approx f_1 CT_1 + (1-f_1)CT_2 \tag{II.1}$$

and

$$f_1 \approx (CT_{ROI} - CT_2)/(CT_1 - CT_2) \tag{II.2}$$

where f_1 is the fraction of the region comprised of material 1 and $(1-f_1)$ is the fraction comprised of material 2.[97] If cerebral edema is defined as excess water within otherwise normal brain, then it is evident from Equation II.2 that the fraction of the region occupied by excess water can be determined from the CT number of the edematous region, the CT number of water, CT_{H2O}, and the CT number of normal brain. In the case of a focal radiation lesion confined to one hemisphere, the CT number of the contralateral hemisphere, CT_{CH}, can be used to approximate the CT number of normal brain. Therefore, the fraction of the irradiated hemisphere comprised of excess water, f_{ED} can be derived from the equation

$$f_{ED} \approx (CT_{IH} - CT_{CH})/(CT_{H2O} - CT_{CH}) \tag{II.3}$$

where CT_{IH} is the CT number of the irradiated hemisphere. The volume of excess water is then

$$V_{IH}f_{ED} \approx V_{IH}(CT_{IH} - CT_{CH})/(CT_{H2O} - CT_{CH}) \tag{II.4}$$

where V_{IH} is the volume of the irradiated hemisphere.

III.   THEORY OF TRANSFER CONSTANT DETERMINATION

The blood-to-brain influx constant for a given molecule, K_i $(ml \cdot g^{-1} \cdot min^{-1})$, is defined as the proportionality constant relating the plasma concentration, C_P, of an indicator at a given time, t, to its rate of accumulation in interstitial brain tissue under the condition of no backflux from brain to blood.   Under the more general condition, allowing for a brain-to-blood backflux constant, K_b (min^{-1}), the change in concentration of compound in brain, $C_B(t)$ $(g \cdot g^{-1})$, can be described by the equation

$$dC_B(t)/dt = K_i C_P(t) - K_b C_B(t) \qquad (III.1)$$

The significance of K_i can be better appreciated by recognizing that it is a function of three parameters: 1) the permeability of the agent, P, in $cm \cdot s^{-1}$, which is the average velocity at which molecules pass from blood into brain, 2) the surface area per unit weight of tissue, S, in $cm^2 \cdot g^{-1}$, which is the area directly accessible to the agent and through which the agent can cross from blood to brain, and 3) the blood flow through the region, F, in $cm^3 \cdot g^{-1} \cdot s^{-1}$ (or equivalently $ml \cdot g^{-1} \cdot s^{-1}$), which gives the rate at which the agent is delivered by the blood to the region.   The exact equation relating these three parameters to K_i is

$$K_i = F \ (\ 1 - e^{-PS/F}) \qquad (III.2)$$

At low blood flows relative to PS, i.e. F<<PS, the term $e^{-PS/F}$ becomes effectively zero, so that K_i is closely approximated by F alone, i.e $K_i \approx F$.   In this situation, movement of the agent from blood to brain is said to be flow limited.   In the case

that F>>PS, the term e$^{-PS/F}$ can be shown via a Taylor series expansion to be closely approximated by 1 - PS/F, so that

$$K_i \approx F[1 - (1 - PS/F)] \quad (F>>PS) \tag{III.3}$$

$$K_i \approx PS \tag{III.4}$$

This equation indicates that when the PS product is low relative to flow, the PS product alone determines the magnitude of K_i. This follows because the agent is being delivered to the region at a much more rapid rate than the rate at which the agent can move across the BBB.

The term blood-to-brain transfer constant, K_i, and "permeability" are sometimes used interchangeably. Therefore, the above equations are important not only because they indicate the parameters which determine K_i but also because they make a distinction between the quantity which is measured in the present study, K_i, and permeability, P. The present work uses the term permeability in the more general sense to signify leakiness. The letter "P" is used for any references to the quantifiable parameter.

The CT-based determination of K_i is derived from Equation (III.1). The solution to this equation is

$$C_B(T) = K_i \int_0^T C_P(t)e^{Kb(t-T)} dt \tag{III.5}$$

The concentration of a compound within a ROI in brain at time T, $C_{ROI}(T)$, is determined by the concentration of that compound within both the blood and the

parenchyma. If the compound is excluded from red blood cells as is Conray 400,[143] the iodinated contrast agent used in the present studies, then

$$C_{ROI}(T) = C_B(T)V_B + C_P(T)V_P \qquad (III.6)$$

where V_B and V_P are the fractional volumes of brain parenchyma and plasma within the ROI. V_P is related to the fractional volume of blood, V_{BI}, by the equation, $V_P=(1-Hct_C)V_{BI}$ where Hct_C is the cerebral tissue hematocrit. The cerebral hematocrit is reduced by a constant amount relative to the peripheral hematocrit, Hct, so that in dog brain $Hct_C=0.5Hct$.[144] Recognizing that V_B is simply $1-V_{BI}$, Equation III.6 can be restated as

$$C_{ROI}(T) = C_B(T)(1-V_{BI}) + C_P(T)V_P = C_B(T) \cdot [1-V_P/(1-0.5Hct)] + C_P(T)V_P \qquad (III.7)$$

Substituting Equation III.5 into III.7 and dividing both sides of the equation by $C_P(T)$,

$$C_{ROI}(T)/C_P(T)=K_i[1-V_P/(1-0.5Hct)] \cdot [\int_0^T C_P(t)e^{Kb(t-T)} dt/C_P(T)]+V_P \qquad (III.8)$$

This equation is a modification of one used in PET to determine transfer constants.[61]

In CT, alterations in x-ray attenuation or CT number are represented by ΔCT, and following administration of a contrast agent, ΔCT_{ROI} is directly proportional to the concentration of that agent in the ROI.[79] Therefore, the left side of Equation III.8 and the integrand of the right side of the same equation can be determined from CT data by using a proportionality constant of c and the equations

$$C_{ROI}(T)/C_P(T)=c\Delta CT_{ROI}(T)/c\Delta CT_P(T)=\Delta CT_{ROI}(T)/[\Delta CT_{ART}(T)/(1-Hct)] \quad (III.9)$$

and

$$C_P(t)/C_P(T)=[c\Delta CT_{ART}(t)/(1-Hct)]/[c\Delta CT_{ART}(T)/(1-Hct)]$$
$$=\Delta CT_{ART}(t)/\Delta CT_{ART}(T) \quad (III.10)$$

where $\Delta CT_P(T)$ and $\Delta CT_{ART}(T)$ are the change in CT number for the plasma or artery, respectively.

Equations III.9 and III.10 can be substituted directly into Equation III.8 for determination of K_i, K_b, and V_P via the equation

$$\Delta CT_{ROI}(T)(1-Hct)/\Delta CT_{ART}(T)$$
$$= K_i(1-V_P/(1-0.5Hct) \left(\int_0^T \Delta CT_{ART}(t)e^{K_b(t-T)}dt/\Delta CT_{ART}(T)\right) + V_P \quad (III.11)$$

which is equivalent to Equation 2.

IV.   ITERATIVE ALGORITHM FOR K_i AND K_b DETERMINATION

A computer program was written to iteratively determine K_b. Because values of K_b of less than zero would be physically impossible, K_b was constrained to a value of greater than or equal to zero. The algorithm made the assumption that the value of the correlation of the data points with a straight line would vary parabolically with alterations in K_b. The goal was then to find the K_b which maximized the correlation. This could be accomplished by either increasing or decreasing K_b to determine which change made the correlation

increase and then changing K_b in that direction until the correlation was maximal. The specifics of the algorithm were:

1.   Set $K_b = 0$, $y(T)=\Delta CT_{ROI}(T)/[\Delta CT_{ART}(T)/(1\text{-Hct})]$ and $x(T)=$

$$(\int_0^T \Delta CT_{ART}(t)e^{K_b(t-T)}\, dt/\Delta CT_{ART}(T))$$ (cf. Equation III.11), and determine the correlation between the points $x(T)$ and $y(T)$.

2.   Increment K_b by a small factor, which was initially set to $0.01\ ml\cdot ml^{-1}\cdot s^{-1}$.

3.   Recompute $x(T)$ and re-compute the correlation between points $x(T)$ and $y(T)$.

4.   If the correlation computed in step 3 is increased, repeat steps 2-4. If the correlation is reduced, negate the increment factor, divide it by 2, and repeat steps 2-4.

5.   If the absolute value of the increment factor is less than 0.0001, then stop.

V. THEORY OF BLOOD FLOW DETERMINATION

Indicator-dilution techniques have demonstrated that changes in the tissue or blood concentration of an indicator following intravenous administration are related to and can be used to quantitatively determine blood flow.[145-147] Use of these techniques for the non-invasive determination of rCBF therefore depends upon the accurate measurement of indicator concentration as a function of time after injection. In dynamic CT, the indicator is iodinated contrast medium, and previous work has shown that changes in CT number after the administration of contrast are linearly related to the actual concentration of contrast medium within ROIs.[79] Thus the CT number *versus* time data obtained from a dynamic CT study directly relate to concentration *versus* time data. Parameters relating to blood flow, including the center of

Figure 28   Schematic diagram illustrating the use of concentration versus time curves in deriving V_{BI} and $<t_f>$. The stippled region is the area under an idealized concentration versus time curve for a peripheral artery, AUC_{PA}, and the cross-hatched region corresponds to the area under an idealized concentration versus time curve for the region of interest, AUC_{ROI}. The fractional blood volume, V_{BI}, is then proportional to AUC_{ROI}/AUC_{PA}. Also shown are the centers of gravity for the arterial curve, $<t_{PA}>$, and for the region of interest, $<t_{ROI}>$. The mean transit time, $<t_f>$, is then proportional to $<t_{ROI}>$ - $<t_{PA}>$, and rCBF is proportional to $(AUC_{ROI}/AUC_{PA})/(<t_{ROI}> - <t_{PA}>)$.
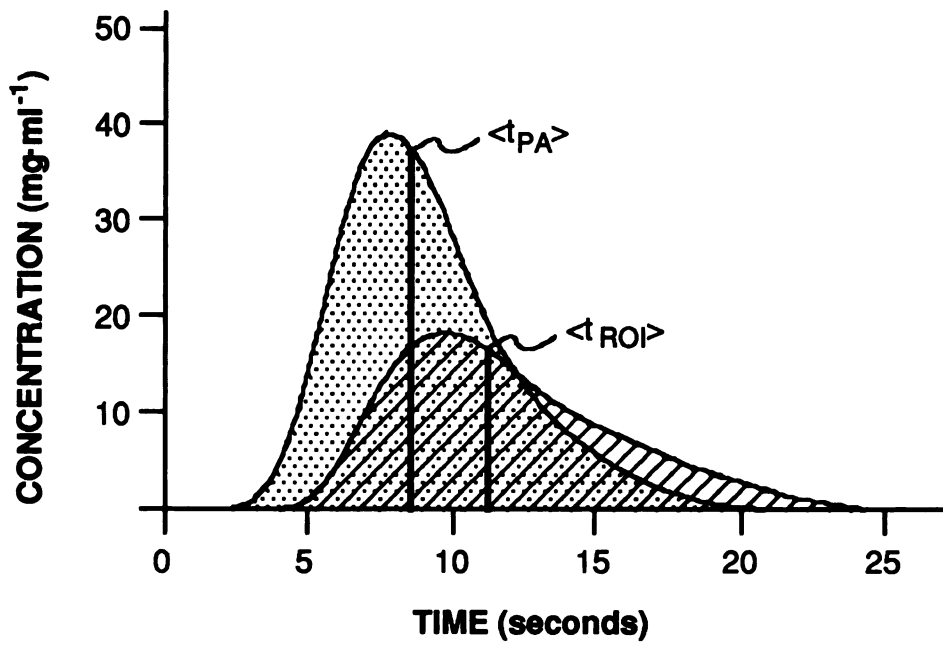
gravity and the area under curve, can be derived from the time-concentration data,[79, 81, 148] and these data can then be analyzed using indicator-dilution principles to determine rCBF as demonstrated below (Figure 28).

Regional CBF can be calculated using the formula

$$rCBF = V_{BI}/<t_f>, \tag{V.1}$$

where V_{BI} represents the fractional blood volume and $<t_f>$ represents the mean transit time.[84] Because V_{BI} and $<t_f>$ cannot be extracted directly from time-concentration curves, it is necessary to use parameters from those curves to calculate these values. Using the relationship between tissue ROI and plasma (P) concentrations (C(t)), $C_{ROI}(t) = V_P \cdot C_P(t)$, where V_P is the fractional volume of the ROI occupied by plasma, the total amount, q, of contrast delivered into a ROI by an arterial plasma concentration of $C_{aP}(t)$ and plasma flow of F_P is given by[84]

$$q = \int_0^\infty F_P \cdot C_{aP}(t) \, dt = 1/V_P \cdot \int_0^\infty F_P \cdot C_{ROI}(t) \, dt. \tag{V.2}$$

Substituting the relationships, $V_P = V_{BI} \cdot (1-HCT_{ROI})$, $C_{aP}(t) = C_a(t)/(1-HCT_{PA})$, and $HCT_{ROI} = j \cdot HCT_{PA}$ into Equation V.2, V_{BI} can be derived and is equivalent to

$$V_{BI} = [(1-HCT_{PA})/(1-j \cdot HCT_{PA})] \cdot [\int_0^\infty C_{ROI}(t) \, dt / \int_0^\infty C_a(t) \, dt] \tag{V.3}$$

where $C_a(t)$ is the arterial blood iodine concentration, HCT is the hematocrit within a peripheral artery (PA), and j is a proportionality constant relating

peripheral hematocrit to ROI hematocrit (Hct_{ROI}).[144] Equation V.3 can also be expressed in terms of the area under the time-concentration (or, equivalently, time-CT number) curve (AUC):

$$V_B = [(1-HCT_{PA})/(1-j \cdot HCT_{PA})] \cdot [AUC_{ROI}/AUC_{PA}] \tag{V.4}$$

Because the AUC following a single contrast bolus is equal for all arteries in the body,[84] any artery visible on a CT scan can potentially be used for determination of the AUC_{PA}. .

The mean transit time, $<t_f>$, is derived from the center of gravity of the time-concentration curve of the ROI, $<t_{ROI}>$, in the following manner. The CT number *versus* time function can be represented by the summation of a number of functions, $f_i(t)$, each representing the change in CT number due to the entrance of the ith molecule of contrast into the ROI. If the bolus instantaneously enters at time 0, each of the r contrast molecules will produce an equivalent change in CT number between times 0 and t_i, the transit time through the ROI for the ith molecule. Thus, the indicator-dilution curve representing a single molecule has a square wave shape, and the overall function representing the indicator-dilution curve for the ROI is the summation of a number of these square wave functions, the number being equal to the number of contrast molecules within the bolus. If the indicator-dilution curve is represented by the function $C_{ROI}(t)$,

$$C_{ROI}(t) = f_1(t) + f_2(t) + \cdots + f_r(t) \tag{V.5}$$

where there are r molecules comprising the indicator bolus and $f_r(t)$ is the function representing the indicator-dilution curve for the rth molecule. The center of gravity of such a function, $<t_{ROI}>$, is given by

$$\int_0^\infty t C_{ROI}(t)\, dt / \int_0^\infty C_{ROI}(t)\, dt = [\int_0^\infty t(f_1+f_2+\cdots+f_r)\, dt]/[\int_0^\infty f_1+f_2+\cdots+f_r\, dt] \qquad (V.6)$$

If the change in CT number in response to a single indicator molecule is ∂, and if all the indicator molecules enter the ROI simultaneously so that there is instantaneous input of the bolus into the ROI at time 0, then f_r is equal to ∂ between 0 and t_r, the transit time through the ROI for the rth molecule, and is zero outside this interval. The center of gravity, $<t_{ROI_i}>$, of the indicator-dilution curve for the ROI resulting from an instantaneous bolus, $C_{ROI_i}(t)$, is equivalent to

$$<t_{ROI_i}> = (\int_0^{t_1} \partial \cdot t\, dt + \cdots + \int_0^{t_r} \partial \cdot t\, dt)/(\int_0^{t_1} \partial\, dt + \cdots + \int_0^{t_r} \partial\, dt) \qquad (V.7)$$

$$= 1/2 \cdot (t_1^2 + \ldots + t_r^2)/(t_1 + \ldots + t_r) \qquad (V.8)$$

Dividing both the numerator and denominator by r, the total number of molecules comprising the indicator bolus shows that

$$<t_{ROI_i}> = 1/2 \cdot [(t_1^2 + \ldots + t_r^2)/r]/[(t_1 + \ldots + t_r)/r] = 1/2 \cdot (<t_f^2>/<t_f>) \qquad (V.9)$$

in which $<t_f>$ and $<t_f^2>$ are the first and second moments, respectively, of a function representing the probability density function of transit times for the ROI.

Using the relation of the first and second moment, $<t_f^2> = <t_f>^2 + (SD_f)^2$,[149] where SD_f is the standard deviation of transit times, and by asserting that SD_f is

proportional to $<t_f>$ by the unknown proportionality constant k,[150, 151] $<t_f>$ can be determined from the relationship,

$$<t_f> = [2/(1+k^2)]\cdot<t_{ROI_i}> \tag{V.10}$$

For a non-instantaneous bolus, the time-concentration curve for the ROI is a convolution of the real input time-concentration curve, $C_{In}(t)$, and the hypothetical curve resulting from an instantaneous bolus, $C_{ROI_i}(t)$. The centers of gravity of these two convolved functions, $<t_{In}>$ and $<t_{ROI_i}>$, can be added to give the center of gravity of the convolution,[149] $<t_{ROI}>$, so that

$$<t_f>=[2/(1+k^2)]\cdot(<t_{ROI}>-<t_{In}>) \tag{V.11}$$

Using the assumption that the mixing of contrast with blood is similar for any two peripheral arteries visible on the same CT scan, the time-concentration curves of those two vessels should also be similar, any difference being due to a disparity in the arrival time of the bolus. Therefore

$$<t_{ROI}>-<t_{In}>=(1-m)\cdot(<t_{ROI}>-<t_{PA}>) \tag{V.12}$$

where $<t_{PA}>$ is the center of gravity of the time-concentration curve of a peripheral artery, m is the fraction of $<t_{ROI}>-<t_{PA}>$ that is due to the difference between the time the bolus arrives at the ROI and the time it arrives at the peripheral artery used for determining $<t_{PA}>$.

Regional CBF can therefore be determined by combining equations V.1, V.4, V.11, and V.12,

$$rCBF = n \cdot [(AUC_{ROI}/AUC_{PA})/(<t_{ROI}> - <t_{PA}>)] \qquad (V.13)$$

where n represents the factor $[(1-HCT_{PA}) \cdot (1+k^2)]/[2 \cdot (1-j \cdot HCT_{PA}) \cdot (1-m)]$. A value of 0.5 was assigned to the factor j,[144] and the magnitude of k was derived as described below.

The variance in the time-concentration curve at the output of a ROI is due to variations both in the times at which indicator molecules arrive at the ROI and the variance in the transit times within the ROI. Because the two processes (i.e. those accounting for the variance in arrival and transit times) are independent, the total variance of the time-concentration curve at the outflow of a ROI will equal the sum of the variances in the arrival and transit times.[149] Therefore, by knowing the variance in arrival times, which can be determined from the time-concentration curve of an artery supplying the ROI, and the variance in outflow times, which can be determined from the time-concentration curve of a vein draining the ROI, the variance and SD of transit times can be determined. In addition, the difference in centers of gravity of the arterial and venous time-concentration curves will give the mean transit time. Although it is difficult to find such a vein or artery for a specific ROI, it is generally possible to identify other representative arteries and veins. For example, on a transverse scan of the dog brain, the vein of the corpus callosum was often identifiable and representative of the draining veins for the level of the brain evident on a CT image, and the lingual artery, which was evident ventral to the trachea, was assumed to be representative of other arteries supplying that level of the brain. The gamma-variate function could be fitted to the time-concentration curves for such vessels and used to derive the variance of the curves, the mean transit time, the SD of transit times, and hence k[148] according to the equation

$$k=(\sigma_{Ve}^2 - \sigma_{PA}^2)^{1/2}/(<t_{Ve}> - <t_{PA}>)$$
(V.14)

where σ^2 is the variance of time-concentration curves for the vein (Ve) of the corpus callosum or the lingual artery (PA), and $<t_{Ve}>$ is the center of gravity of the venous curve.

A number of important factors and limitations had to be considered before this theoretical methodology of using CT to measure rCBF could be properly implemented. The factors included the determination of AUC and $<t>$ for tissue and arterial ROIs, and the factors HCT_{PA}, j, k, m.

Methods for determining the AUC and $<t>$ based on the fitting of a gamma-variate function to time-concentration data have been described in detail.[79-82, 152] The ultrafast CT scanner used for the present study supplied a routine which would automatically fit a gamma-variate function to the CT number *versus* time data for any specified ROI. The AUC and $<t>$ of the fitted curves were also automatically calculated. In general it was possible to obtain suitable data for ROIs of various sizes and shapes. However when a small ROI was required, such as that for a peripheral artery, there was concern that errors could be introduced that could have a major impact in the calculation of rCBF. For instance, the time-concentration data for small, poorly defined vessels might include a substantial portion of the surrounding parenchyma which would lead to volume averaging and an underestimation of AUC_{PA}. It was essential, therefore, that arterial ROI selection was done carefully and that the vessel selected was large enough to clearly support an ROI of 1 pixel or more. For these reasons, the lingual artery, which appeared to be the largest artery visible within the CT scan, was chosen for determining AUC and $<t>$ of the peripheral artery.

Another important consideration in acquiring time-concentration data for an ROI within brain tissue, was the effect of BBB breakdown on the measurement of rCBF. BBB breakdown following focal irradiation has been well documented, [47, 58] and the presence of such a breakdown could tend to increase AUC and <t> and thus alter the calculations of blood flow parameters (Equations V.4, V.11, V.12, and V.13). In fact, it had been reported that blood flow parameters acquired in the presence of BBB breakdown would be inaccurate.[153] Therefore, the effect of BBB breakdown on measured rCBF was estimated by a simulation of the alteration in the CT number *versus* time curve in the presence of BBB breakdown.

For the simulation, time-CT number data was generated using a gamma-variate function. The values of the parameters which characterize the gamma-variate function, A, B, and C (see Methodology, Validation, and Results - Method Overview: CT-Based Measurements for details), were set to 2.5, 1.5, and 300, respectively, for the arterial input curve, and 4, 1.5, and 0.8, respectively for the ROI flow curve. These values were comparable to those found in preliminary experiments. The parameter t_0, which is the arrival time of the contrast bolus at the ROI, would not be expected to be altered by BBB breakdown and was set equal to 0. In order to simplify the calculations, it was assumed that the inflow of the contrast into the ROI was completed prior to outflow, and that transfer across the BBB breakdown was unidirectional during the passage of the bolus. With this simplified simulation, beyond the peak of the time-concentration curve (when inflow was complete), the change in contrast concentration was reduced by a fraction equivalent to the fraction of total blood flow that crossed the BBB. As an example, if the degree of BBB breakdown was equivalent to 15% of rCBF, and if the CT number following the peak of contrast enhancement fell by 10 CT numbers in a given period of time, the presence of

BBB breakdown would result in there only being a drop of 8.5 CT numbers during this period. Following the simulation, a gamma-variate function could then be fitted to the CT number *versus* time data (see Methodology, Validation, and Results - Method Overview: CT-Based Measurements), and the effects of an altered BBB on the fit parameters and computed blood flow parameters assessed.

Because cerebral blood flow ranges from approximately 20-100 ml·100 ml^{-1}·min^{-1},[56], and because blood-to-brain transfer constants in the presence of radiation injury have been reported to be in the range of 1-3 ml·100 ml^{-1}·min^{-1},[47] the blood-to-brain transfer constants were set equal to either 5 or 15% of rCBF. In the case that BBB transfer was 5% of total flow, the changes in calculated vascularity, mean transit time, and rCBF were estimated to be only +1.0, +4.9, and -3.8% respectively. Even for breakdowns as large as 15% of total flow, the changes for the same respective parameters were +13.8, +8.5, and -4.6%. Based on these calculations, it appeared that the CT method of rCBF measurement would still be accurate ±10% even in the presence of BBB breakdown.

Because of the form of Equation V.1, it was clear that the accurate determination of mean transit time for rCBF calculation was most critical at short transit times, and underestimations of transit time would tend to result in larger errors than overestimation. For example, whereas a 0.2 second overestimation or underestimation of a mean transit time of 3.0 seconds would result in errors in rCBF of -6.2% and +7.1%, respectively, similar errors for a mean transit time of 1.0 second would result in errors in rCBF of -16.7% and +25%. Based on studies of focal hyperthermia damage in brain,[133] in which decreased mean transit time was never seen, it was hypothesized that irradiation would result in

increased mean transit time, so that this limitation was not expected to be a significant one for the present studies.

Another factor which had to be considered in the computation of rCBF by CT was the proportionality constant k. This factor relates the variation in transit times to the mean transit time. If brain blood flow was modeled as a plug of fluid flowing through a single tube, the variation in transit times was 0 and thus k was zero. In addition, because the washout of blood from a single well-mixed compartment is exponential in form,[152] the mean transit (or washout) time for such a model (i.e a single well-mixed compartment) is equivalent to the SD of transit times and thus k is one. Attempts to model blood flow with more sophisticated models such as multiple parallel compartments resulted in values which were clearly at odds with experimental results,[148] suggesting that the value of k had to be determined empirically. However, experimental determinations of k had found the value to be remarkably constant within a given organ system, with values in between 0 and 1 depending on the system,[150, 151] suggesting that true blood flow was best modeled as something in between plug flow and flow in a simple well-mixed compartment. Although the value of k had not been determined for brain, it was determined using ultrafast CT (see Equation V.14 and preceding discussion) in a series of twelve dogs. The average value of k was 0.757 ± 0.045 (mean $\pm$ SE).

The factor m was determined from the difference in the times of arrival of the contrast indicator at the peripheral artery used for determining $<t_{PA}>$ and at the ROI in brain tissue. Based on the same set of studies used for determination of k, the value of m was found to be 0.40 ± 0.07 (mean $\pm$ SE). It was assumed that when the peripheral artery and the ROI were within the same scan plane, the arrival times would be similar and m would be relatively small, so that it would have only a minor impact on the blood flow calculation using Equation

V.13. However, it was also noted that if the difference in arrival times became large relative to the mean transit time (i.e. m became larger), m would have a greater impact on the rCBF calculation. Thus, if the difference in arrival times was substantial, it would be necessary to carefully account for the effect of m on rCBF.

It was also important to accurately determine the blood (HCT_{PA}) and tissue (HCT_{ROI}) hematocrits in order to measure rCBF using CT (see Equation V.3 and preceding discussion and Equation V.13). Although it was clear that HCT_{PA} could be readily determined from a venous blood sample, it was also evident that the indicator bolus would reduce the hematocrit due to simple dilution. Some errors could be introduced into the rCBF measurement by not taking this dilutional effect into consideration. For instance, assuming a hematocrit of 40%, a factor of j of 0.50,[144] a bolus of contrast of 1 ml kg^{-1} and width of 5 seconds, and a cardiac output varying from 35-140 ml kg^{-1} min^{-1}, dilution could change the calculated rCBF by 2-9% from the actual rCBF.* However, it was possible to explicitly determine and correct for this dilution, because the volume diluted is equivalent to the product of total cardiac output and the bolus width. Both of these factors were determined from a time-concentration curve of a peripheral artery [84] Initial studies demonstrated the average dilution. of the hematocrit to be 0.90 ± 0.01 (mean ± SE). Based on this dilution, an average hematocrit of 34.9 ± 0.9 (mean ± SE), and the aforementioned values of j, k, and m, the value of n in Equation V.13 was determined to be 1.069.

---

* For example, for a cardiac output of 35 ml·kg^{-1}·min^{-1}, within the 5 second bolus, the cardiac output would be (5 seconds/ 60 seconds min^{-1})(35 ml·kg^{-1}·min^{-1}) or 2.92 ml·kg^{-1}. The 1 ml·kg^{-1} of contrast would dilute the hematocrit, so that the hematocrit would actually be [2.92/(2.92 + 1)]·40% or 29.8%. The factor multiplying AUC_{ROI}/AUC_{PA} in Equation V.4 would be changed from (1-0.40)/(1-0.5·0.40) or 0.75 to (1-0.298)/(1-0.5·0.298) or 0.82, which is equivalent to a change of (0.82-0.75)/0.82 or 9%.

VI. SIMULATED CHANGE IN CT NUMBER DUE TO BLOOD-BRAIN BARRIER BREAKDOWN

The concentration of the iodinated contrast agent used in the present studies declines bi-exponentially in the first four hours following administration,[154] so that the plasma concentration of iodine, $C_P(t)$, can be described by the equation

$$C_P(t) = A'e^{-\alpha t} + B'e^{-\beta t} \qquad\qquad (VI.1)$$

In addition, because of the proportionality between the change in CT number for an artery, $\Delta CT_{ART}(t)$, to $C_P(t)$

$$c\Delta CT_{ART}(t)/(1-Hct) = C_P(t) \qquad\qquad (VI.2)$$

which indicates that $c\Delta CT_{ART}/(1-Hct)$ also changes bi-exponentially following injection. Preliminary studies have suggested values of c and Hct of 0.059 and 0.35, respectively. The values of A', B', α, and β can be obtained from the $\Delta CT_{ART}(t)$ data following an iodinated contrast bolus combined with the multi-exponential curve-fitting technique referred to as curve-feathering.[155] Typical values of A', B', a, and b obtained with this method are 4 mg/ml, 4 mg/ml, 0.01 s⁻¹, and 0.0006 s⁻¹.

Combining these values of A', B', α, and β, with Equations VI.1 and VI.2, typical values of $\Delta CT_{ART}(t)$ can be obtained from the formula

$$\Delta CT_{ART}(t) = 44e^{-0.01t} + 44e^{-0.0006t} \qquad\qquad (VI.3)$$

Furthermore, combining Equations III.5 and VI.1

$$C_B(T) = K_i e^{-K_b T} \int_0^T (A' e^{-\alpha t} e^{K_b t} + B' e^{-\beta t} e^{K_b t})\, dt \tag{VI.4}$$

$$= A' K_i e^{-K_b T} \int_0^T e^{(K_b-\alpha)t}\, dt + B' K_i e^{-K_b T} \int_0^T e^{(K_b-\beta)t}\, dt \tag{VI.5}$$

$$= [A' K_i/(K_b-\alpha)][e^{-\alpha T}-e^{-K_b T}] + [B' K_i/(K_b-\beta)][e^{-\beta T}-e^{-K_b T}] \tag{VI.6}$$

In addition, by Equation III.6

$$C_{ROI}(T) = C_B(T)V_B + C_P(T)V_P = c\Delta CT_{ROI}(T) \tag{VI.7}$$

where c is the proportionality constant relating the change in iodine concentration within a ROI ($C_{ROI}(T)$) to the change in CT number for that ROI (ΔCT_{ROI}) (see also Equation III.9 and preceding discussion). V_B, the fraction of an ROI comprised of brain parenchyma (or non-vasculature), is equivalent to 1-[$V_P/(1-0.5Hct)$] (see Equation III.7 and preceding discussion). Substituting this relationship and Equations VI.2 and VI. 6 into VI.7 and solving for ΔCT_{ROI}

$$\Delta CT_{ROI}(T) = \{[1-V_P/(1-0.5Hct)]/c\}\{[A' K_i/(K_b-\alpha)][e^{-\alpha T}-e^{-K_b T}]+[B' K_i/(K_b-\beta)][e^{-\beta T}-e^{-K_b T}]\} + (V_P/c)(A' e^{-\alpha t}+B' e^{-\beta t}) \tag{VI.8}$$

By inserting the same values of c, Hct, A', B', α, and β as mentioned above, this equation shows the explicit formula used to calculate the expected values of $\Delta CT_{ROI}(T)$ for various input values of K_i, K_b, and V_P.

VII.   CHRONIC INTRAVENOUS CATHETER IMPLANT

1.   The medial left or right thigh was clipped from the femoral triangle to the stifle joint of overlying hair and aseptically prepared using a standard surgical scrub.

2.   A 3-5 cm longitudinal incision was made over the femoral artery and vein just distal to the femoral triangle.

3.   A 2-3 cm length of femoral vein was isolated using blunt dissection.

4.   After placing a ligature distally on the isolated vein segment, a small incision was made in the vein just proximal to this ligature. Approximately 50 cm of a 100 cm length of sterile, Tygon tubing (inner diameter 0.040 inches, outer diameter 0.070 inches) was inserted into the vein through this incision. The Tygon tubing had two plastic cuffs, which were 1 mm thick and 1 mm wide and separated by 2 mm, which had been cut from larger diameter tubing (inner diameter 1 mm, outer diameter 2 mm) and glued to the Tygon tubing at the point 50 cm from the end. Two additional cuffs had been glued 10 cm away from the first two. The tubing was advanced so that the two cuffs at 50 cm (the proximal cuffs) lied just inside the vein, 1-2 mm proximal to the vein incision. The distal cuffs remained outside the vein.

5.   The tubing was secured by placing a ligature around the vein and tubing at a point between the two cuffs inserted into the vein. A second ligature was placed just distal to these two cuffs. The catheter was looped such that the two distal cuffs overlaid the two proximal cuffs which had been sutured within the vein. The ends of the two previously placed sutures

were then used to place one ligature between the two distal cuffs and a second ligature just distal to these same cuffs.

6.   The patency of the inserted tubing was checked by flushing 5-10 ml of a heparinized saline solution (3.3 U/ml of heparin) through the line.

7.   The free end of the tubing was attached to a long metal trocar, 3 mm in diameter and 60 cm in length) and tunneled subcutaneously from the incision to the withers. The trocar was pushed through the skin along with the attached catheter along the midline between the scapulae.

8.   The muscle, subcutaneous tissue, and skin of the medial thigh were closed in three separate layers. The tubing extending from between the scapulae was attached to an infusion pump placed within a vest worn by the animal (Figure 2).

VIII. 125I IMPLANT AND REMOVAL

1.   After induction of anesthesia, the hair of the scalp was clipped from just caudal to the external occipital protuberance rostrally to the dorsal orbital rim. The clipping extended 4-6 cm lateral to the midline on both the left and right sides.

2.   After a routine sterile surgical preparation of this region, the point on the scalp 57 mm rostral to the external occipital protuberance and 20 mm lateral to the midline was carefully noted, and a 2 cm longitudinal incision was centered on this point.

3.   After using pressure for hemostasis following the skin incision, a 2 cm incision was made in the temporalis muscle, the incision extending down to the skull.

4. Using the blunt end of the scalpel handle, the muscle was scraped from the bone so that a region of bone approximately 2 cm in diameter was visible and clear of overlying tissue and blood.

5. A 1 mm diameter hole, centered at the same point as the original scalp incision and 45° off vertical, was drilled in the skull while taking care so as not to penetrate the brain.

6. The skin incision was temporarily closed with a continuous suture pattern in order to prevent contamination of underlying tissues during the following procedures.

7. Five contiguous 3 mm thick transverse CT scans were obtained in order to check placement of the twist drill hole in relation to underlying brain tissues. The hole placement was planned such that a transverse CT scan containing the hole should correspond to the level of the brain at the junction of the thalamus and basal ganglia, 3-6 mm caudal to the most rostral extent of the lateral ventricles. If the hole was misplaced, the hole was re-drilled at the proper position based on the CT scans.

8. After another sterile surgical preparation of the previous incision, a blunt-ended probe was inserted through the twist drill hole and into the brain in order to clear a path for insertion of the polyethylene catheter containing the radioactive seed. During insertion, the probe lied just to the left of the ventricle within the transverse plane at a 45° angle off vertical.

9. In order to close the incision rapidly following radioactive seed placement, sutures were pre-placed in such a fashion that both skin and muscle could be closed simultaneously.

10. The catheter containing the ^{125}I seed was 13.5 mm in length (inner diameter 0.034 inches and outer diameter 0.050 inches), and the seed was placed at the most distal end of the catheter. It was kept in alcohol

for 24 hrs prior to implant and then rapidly rinsed with sterile saline immediately prior to insertion. It was inserted into the brain so that the top of the catheter lied flush with the skull.

11. After rapidly closing the incision using the pre-placed sutures, the dog was allowed to recover from anesthesia. The seed was left in for the appropriate time for a dose of 20 Gy at a point 0.75 cm from the seed (see Appendix X. Dose Calculation). Typically, this was 36-54 hrs for seeds of strength 16-24 mCi.

12. For seed removal, the dog was rapidly anesthetized with a 3-5 ml bolus of intravenous 4% sodium thiamylal, the incision surgically scrubbed twice with betadine and alcohol, and the seed removed.

13. The incision was then re-scrubbed using a standard surgical scrub, and the muscle, subcutaneous tissue, and skin closed in three separate layers.

IX. DOSE CALCULATION

The dose rate, D_R, at some distance r from the type of ^{125}I source used in the present study can be calculated using the equation

$$D_R = \varepsilon Y/r^2 \qquad\qquad (IX.1)$$

where ε is the dose-rate constant, and Y is the activity of the source in millicuries.[156, 157] In our experiments, dose was calculated at a point 0.75 cm from the ^{125}I source, and the corresponding ε for this distance is 0.0133 $Gy\cdot cm^2\cdot hr^{-1}\cdot mCi^{-1}$,[156, 157] giving

$$D_R = 2.36Y \qquad\qquad\qquad (IX.2)$$

The total dose, D_T, delivered within a given period is calculated by integrating the dose rate over the entire period or

$$D_T = \int_0^t D_{Ri}e^{-\kappa\tau}d\tau \qquad\qquad\qquad (IX.3)$$

where t is the duration of of irradiation, τ is a dummy variable for integration, D_{Ri} is the initial dose rate, and κ is the decay rate constant for ^{125}I, equivalent to $4.8X10^{-4}$ hr^{-1}.[156] Solving Equation IX.3

$$D_T = (D_{Ri}/\kappa)(1-e^{-\kappa t}) \qquad\qquad\qquad (IX.4)$$

Thus, the time to deliver a given total dose is

$$t = -\{ln[1 - (\kappa D_T/D_{Ri})]/\kappa\} \qquad\qquad\qquad (IX.5)$$

Thus, in order to deliver a total dose of 20 Gy as used in the present experiments, the time, in hours, necessary was

$$t = -ln[1 - (9.6X10^{-3} \text{ Gy·hr}^{-1}/D_{Ri})]/4.8X10^{-4} \text{ hr}^{-1} \qquad (IX.6)$$

X.   ANALYSIS OF VARIANCE - DESCRIPTION AND RATIONALE

Analysis of variance (ANOVA) is a statistical method used to analyze which factors are related to the variation in some biologic or physical response of interest. An important advantage of using an ANOVA is that it can be used to examine the relations of multiple factors to a response in a single experiment. In a typical ANOVA, one designs a model describing the relationship of the response (or dependent) variable to the factors (or independent variables) which are hypothesized to relate to the response. The factors which are included in the model can be either continuous or discrete. For example, in an experiment examining the effect of a drug on some biological response, the weight of each animal would be considered a continuous variable, and the sex would be considered a discrete variable. In addition, factors can be either fixed or random. Fixed factors are those which are specified by the experimental design, such as the type or dose of drug in the above example. Random factors are those which are not experimentally controlled, such as animal weight. A model which contains both fixed and random factors is referred to as a mixed-model.

ANOVAs can also be useful in accounting for factors which interact in such a way that their relation to the response of interest is obscured. As an example, consider the study of the response to a drug at various times after administration.   If the response was measured without any consideration for time after drug administration, it could be difficult to establish the relation between the drug and the response. If the response was measured too early after drug administration, there might be no measurable response because there would have been too little time for drug absorption. Similarly, if the response was measured too late, the drug might already have been excreted so

that once again no response would be measured. However, if the response was measured multiple times after drug administration and plotted as a function of time, it would be clear that the response was dependent both on drug administration and the time after administration. The interaction between drug and time would be evident. ANOVAs are helpful in that if the response is hypothesized to be related to the interaction of factors, the interaction can be entered into the model design so that its significance can be determined.

Finally, data from an experiment measuring a response multiple times within a single subject can be correctly analyzed using an ANOVA. An example of such an experiment would be one looking at changes in the response of an individual to a drug at multiple times after administration. If one is analyzing how the response to the drug may change as a function of time, it is important to account for the fact that the responses at the various time points are not independent. A repeated-measures ANOVA accounts for this lack of independence and thus makes it possible to do a proper statistical analysis of variation of the response as a function of time.

FOR REFERENCE